

Fall 2022

## Supported Metal Bifunctional and Bimetallic Catalysts With Precisely Controlled Structures and Properties

Anhua Dong

Follow this and additional works at: <https://scholarcommons.sc.edu/etd>

 Part of the [Chemical Engineering Commons](#)

---

### Recommended Citation

Dong, A.(2022). *Supported Metal Bifunctional and Bimetallic Catalysts With Precisely Controlled Structures and Properties*. (Doctoral dissertation). Retrieved from <https://scholarcommons.sc.edu/etd/7105>

This Open Access Dissertation is brought to you by Scholar Commons. It has been accepted for inclusion in Theses and Dissertations by an authorized administrator of Scholar Commons. For more information, please contact [digres@mailbox.sc.edu](mailto:digres@mailbox.sc.edu).

SUPPORTED METAL BIFUNCTIONAL AND BIMETALLIC  
CATALYSTS WITH PRECISELY CONTROLLED STRUCTURES AND  
PROPERTIES

by

Anhua Dong

Bachelor of Engineering  
Shandong Normal University, 2013

Master of Engineering  
Tianjin University, 2016

---

Submitted in Partial Fulfillment of the Requirements

For the Degree of Doctor of Philosophy in

Chemical Engineering

College of Engineering and Computing

University of South Carolina

2022

Accepted by:

John R. Regalbuto, Major Professor

John R. Monnier, Committee Member

Christopher Williams, Committee Member

Aaron K. Vannucci, Committee Member

Mellisa Ann Moss, Committee Member

Cheryl L. Addy, Interim Vice Provost and Dean of the Graduate School

© Copyright by Anhua Dong, 2022  
All Rights Reserved.

## DEDICATION

I dedicate this work to my husband Bing for his constant support, patience, encouragement and company, to my son Ethan, he has brought so much joy and happiness since his birth.

I also dedicate this work to my parents for their unconditional love and lifetime support, to my parents-in-law for their strong help in taking care my son in these years. The dedication also goes to all my three siblings, my elder brother, Anwei Dong, my elder sister, Weiling Dong, and my younger sister, Hui Dong, I felt so much love and care from them through my life.

## ACKNOWLEDGEMENTS

First of all, I would like to thank my advisor Prof. John R. (JR) Regalbuto, without him, I wouldn't be where I am in my research career. He brought me to CReF, an excellent, vibrant and caring/friendly group. He gave me so many great ideas to start my projects, he enlightened me in many aspects of the experiments. My speaking English was poor, but he always encouraged me to practice it and speak slowly. I was shy to do public speaking before and lack experience on it, he always creates opportunities for me to go upfront and be brave to present. I'm so grateful to him. He questioned me, challenged me when he finds it's necessary, all these make me to think more rigorously and comprehensively.

I would like to thank my committee members Prof. John Monnier, Prof. Chris Williams and Prof. Arron Vannucci for their expertise and instruction during my graduation study. I really appreciate Prof. Monnier's amazing guidance on reaction, mass spectra analysis, etc. I am full of gratitude for Prof. Williams instruction on IR experiment design and data analysis as well as in the reaction kinetic simulation. I am also very grateful for Prof. Vannucci's warm help in the HDO reaction in metal-acid bifunctional project.

I would like to thank Prof. John Meynard Tengco, who helped me so much in catalysts synthesis especially when I started my work here, as well as in a lot of data analysis and equipment maintenance. Dr. Jeremiah Lipp has been very helpful in XRD analysis. Dr. Abolfazl Shkouri, Dr. Ritu Banerjee, Dr. Leandro (Andy) Tagum De Castro,

Md Masudur Rahman, et al are amazing colleagues who are very friendly careful and supportive.

I also would like to thank Dr. Doug Blom who helped to collect a lot of amazing STEM images for my catalysts, and Dr. Stavros for his help in recording the XPS spectra.

I would like to thank Shitou Dong and Chuanrong Dong, my dad and my mum, for their continuous love and support. No matter where I am, they are always there for me. Their character of being honest, kind-hearted and industrious, are always the best lessons I had in my life. I would like to thank my three siblings. We had so much joy and pleasure through our childhood, and they are always there caring for me. I miss them so much.

Most of all, I would like to thank my husband, I am very lucky to have him in my life, he brought so much happiness and joy to my life. He gave me so much help and support for my career. I'm very thankful for every minute of his company during the weekend and late night in the lab. I would like to thank my son, Ethan. He is such a treasure for me, his appearance brought so much joy to my life and taught me how to be responsible.

## ABSTRACT

In heterogenous catalysis, metallic nanomaterials play vital roles in numerous chemical processes. However, monofunctional catalysts are greatly impeded in their applications especially in the systems including tandem and/or sequential reaction steps. Besides, the catalytic performance can also be greatly influenced by the particle size, morphology, and geometry of the surface metal atoms.

The goal of this work is to synthesize bifunctional or bimetallic nanoparticles with high metal dispersion and homogenous alloys by rational synthetic strategies to facilitate the catalyst function. Strong electrostatic adsorption (SEA) is an effective and facile methodology to produce well dispersed and uniform nanoparticles. Metal-acid bifunctional catalysts with ultra-small Pd nanoparticles (< 2nm) and tunable amount of acid sites were synthesized by using SEA protocol over metal (Zr, Nb)-doped silicas with hierarchically large mesopores. These bifunctional catalyst with varied metal/acid ratios were evaluated by hydrodeoxygenated (HDO) reaction of methyl-guaiacol under mild conditions. The resultant catalytic performance showed Nb-containing bifunctional catalysts with ultra-small Pd nanoclusters benefited the reactivity (97% conversion, 100% hydrogenation and >20% selectivity to deoxygenated products) due to the optimal Pd/acid balance.

Addition of a secondary metal to prepare bimetallic catalysts is another promising strategy to overcome the limitations of mono-metallic/functional materials taking into consideration of the electronic and geometric effects in the alloying nanoparticles.

Simultaneous strong electrostatic adsorption (co-SEA) was used to prepared bimetallic PdAu alloys with three atomic ratio (Pd:Au=3:1, 1:1, 1:3) on high surface area silica and  $\gamma$ -Al<sub>2</sub>O<sub>3</sub>. The principle of preparing PdAu alloys with varied compositions was governed by controlling the concentration of Pd and Au complex precursors in co-SEA synthetic procedure. Highly dispersed and homogenously alloyed PdAu nanomaterials were successfully achieved (<1.6 nm). The presence of Pd oxide species co-SEA synthesized alloys with higher loadings of Pd is due to the ultra-small nanoparticles, the amount of which can be tuned by controlling the alloy composition. Further work was conducted to extend co-SEA synthetic procedure for yielding dilute limit of Pd into Au nanocluster (atomic Pd/Au=1:1, 0.23:1, 0.08:1, 0.04:1, ....., 0.01:1) on silica and estimated their catalytic function in the partial oxidation of 1-phenylethanol. Isolated Pd species in Au clusters were obtained over Pd/Au < 0.08. Significant improvement in the activity of 1-phenylethanol oxidation were acquired over PdAu homogenous alloys with Pd monomers due to the electronic and geometric effects.



## TABLE OF CONTENTS

DEDICATION .....	iii
ACKNOWLEDGEMENTS .....	iv
ABSTRACT .....	vi
TABLE OF CONTENTS .....	viii
LIST OF TABLES .....	x
LIST OF FIGURES .....	xii
CHAPTER 1 INTRODUCTION .....	1
1.1 Heterogenous Catalysts Preparation.....	2
1.2 Catalysts characterization.....	12
1.3 Bifunctional and Bimetallic Catalysts.....	14
1.4 Dilute Limit Alloy Catalysts .....	15
CHAPTER 2 SYNTHESIS OF METAL-ACID BIFUNCTIONAL CATALYSTS ON HIERARCHICALLY MESOPOROUS SILICA FOR METHYL-GUAIACOL HYDRODEOXYGENATION UNDER MILD CONDITION .....	16
2.1 Abstract .....	16
2.2 Introduction .....	17
2.3 Experimental .....	20
2.4 Results and Discussion.....	25
2.5 Conclusion.....	46

CHAPTER 3 A GENERALIZABLE AND FACILE SYNTHESIS OF GEOMETRICALLY CONTROLLED AND HIGHLY DISPERSED PDAU NANOPARTICLES ON $\text{SiO}_2$ AND $\text{Al}_2\text{O}_3$ .....	47
3.1 Abstract .....	47
3.2 Introduction .....	48
3.3 Characterization .....	53
3.4 EXPERIMENTAL RESULTS AND DISCUSSIONS .....	56
3.5 Conclusions .....	72
CHAPTER 4 THE PREPARATION OF SILICA SUPPORTED, DILUTE LIMIT PDAU ALLOYS VIA SIMULTANEOUS STRONG ELECTROSTATIC ADSORPTION .....	73
4.1 Abstract .....	73
4.2 Introduction .....	74
4.3 Experimental .....	76
4.3 Characterization and evaluation .....	79
4.4 Partial Oxidation of 1-Phenylethanol .....	82
4.5 Results and discussion.....	83
4.5 Conclusion.....	101
REFERENCES .....	102
APPENDIX A SUPPLEMENTARY MATERIALS TO CHAPTER 2 .....	117
APPENDIX B SUPPLEMENTARY MATERIALS TO CHAPTER 3 .....	119

## LIST OF TABLES

Table 1.1 The normal high and low PZC support materials, metal anions and cations. ....	11
Table 1.2 Catalyst synthesis summary. ....	13
Table 2.1 Textural and acidic properties of the as-prepared silicas. ....	27
Table 2.2 Maximum adsorption of PdTACl on metal doped KIT5 and KIT6. ....	31
Table 2.3 Summary of particle size pre- and post-HDO reaction and Pd leaching. ....	33
Table 2.4 Conversion, deoxygenated rate and products distribution in HDO reactions at 112 °C, 12.5 bar H <sub>2</sub> for 4 hrs. ....	41
Table 3.1 Support property and uptake of Pd-Au pair summary. ....	51
Table 3.2 Catalysts information. ....	53
Table 3.3 Detailed composition derived from XRD pattern fitting. ....	64
Table 3.4 Particle size comparison by XRD, STEM and CO-chemisorption analysis. ....	69
Table 4.1 Catalysts information and concentrations of metal precursors in the synthesis. ....	78
Table 4.2 XRD derived particle size, peak centers and Vegard's law derived peak centers. ....	86
Table 4.3 Pulse CO chemisorption over PdAu DLA catalyts. ....	87
Table 4.4 Binding energy of Au4f, Pd3d, Au4d, and surface composition derived by XPS spectra. ....	92
Table 4.5 Assignments of CO adsorption on Pd sites over monometallic and PdAu DLA catalysts. ....	96

Table A.1 Acidity of bifunctional catalysts and supports quantified by NH <sub>3</sub> -TPD.....	117
-----------------------------------------------------------------------------------------------------	-----

## LIST OF FIGURES

Figure 1.1 Precipitation synthetic procedure. ....	3
Figure 1.2 Schematic synthesis through sol-gel method, (a) film-based, and (b) powder nanoparticles.....	5
Figure 1.3 Schematic representation of catalysts by hydrothermal synthesis method. ....	6
Figure 1.4 (a) Scheme of SEA mechanism; (b) SEA synthetic procedure.....	7
Figure 1.5 Simulation on the pH shift of $\gamma$ -Al <sub>2</sub> O <sub>3</sub> with surface loadings (PZC=8.0, DpK=5.0, SA=180 m <sup>2</sup> /g).....	8
Figure 1.6 Adsorption survey of Pt ions and cations over various PZC materials vs pH. ....	9
Figure 2.1 Isotherm curves of KIT5 series silicas (a) and KIT6 series silicas (b); pore size distribution of KIT5 series (c) and KIT6 (d) series silicas. ....	26
Figure 2.2 Metal (W, Zr, Nb) leaching (a), surface area loss (b) and XRD patterns comparison (c) during the thermal stability test. ....	29
Figure 2.3 Adsorption survey of PdTACl on metal-doped KIT5 (a) and metal-doped KIT6 (b). ....	30
Figure 2.4 Normalized XRD patterns for silica supports and bifunctional catalysts: (a) KIT5 series, (b) KIT6 series.....	31
Figure 2.5 Deconvoluted XRD patterns for Pd5/S (a), PdZr5/S (b), PdNb5/S (c), Pd5/D (d), PdZr5/D (e), PdNb5/D (f). ....	32
Figure 2.6 Deconvoluted XRD patterns for Pd6/S (a), PdZr6/S (b), PdNb6/S (c), Pd6/D (d), PdZr6/D (e), PdNb6/D (f). ....	32

Figure 2.7 NH <sub>3</sub> -TPD spectra of bifunctional catalysts and the supports: (a) on metal-doped KIT5, (b) on metal-doped KIT6.....	35
Figure 2.8 Conversion and selectivity of main products in the HDO reaction of M-GUA on (a) Pd5/S, (b) PdZr5/S, (c) PdNb5/S, (d) Pd5/D, (e) PdZr5/D, (f) PdNb5/D, SEA and DI were run for 4 hours and 8 hours, respectively.....	37
Figure 2.9 Conversion and selectivity of main products in the HDO reaction of M-GUA on (a) Pd6/S, (b) PdZr6/S, (c) PdNb6/S, (d) Pd6/D, (e) PdZr6/D, (f) PdNb6/D, SEA and DI were run for 4 hours and 8 hours, respectively.....	38
Figure 2.10 Converted rate (a) and selectivity to dehydrogenated products vs conversion (b) of M-GUA over the as-prepared bifunctional catalysts. ....	40
Figure 2.11 Reaction mechanism of HDO of M-GUA.....	43
Figure 2.12 Normalized XRD patterns comparison before and after HDO reactions over bifunctional catalysts supported on metal-doped KIT5 (a) and metal-doped KIT6 (b). ....	45
Figure 2.13 Deconvoluted XRD patterns of bifunctional catalysts after HDO reactions: (a) Pd5/S-HDO-4h, (b) PdZr5/S-HDO-4h, (c) PdNb5/S-HDO-4h, (d) Pd5/D-HDO-10h, (e) PdZr5/D-HDO-10h, (f) PdNb5/D-HDO-8h.....	45
Figure 2.14 Deconvoluted XRD patterns over bifunctional catalysts after HDO reactions: (a) Pd6/S-HDO-4h, (b) PdZr6/S-HDO-4h, (c) PdNb6/S-HDO-4h, (d) Pd6/D-HDO-10h, (e) PdZr6/D-HDO-10h, (f) PdNb6/D-HDO-8h. ....	46
Figure 3.1 Equilibrium adsorption plots of single Pd, Au (dash lines) and Pd-Au pair (solid plots) on A300 (a) and $\gamma$ -Al <sub>2</sub> O <sub>3</sub> (b).....	57
Figure 3.2 TPR profiles for PdAu catalysts on A300 by co-SEA (a), by co-DI (b); on $\gamma$ -Al <sub>2</sub> O <sub>3</sub> by co-SEA (c), by co-DI (d).....	58
Figure 3.3 TPR-MS profiles over Pd <sub>3</sub> Au <sub>1</sub> /Al <sub>2</sub> O <sub>3</sub> _co-SEA. ....	59
Figure 3.4 XRD patterns of monometallic Pd and Au catalysts by SEA and DI (a, d); bimetallic PdAu catalysts by co-SEA (b, e), by co-DI (c, f), wherein plots of (a-c) and (d-f) plots were over A300 and $\gamma$ -Al <sub>2</sub> O <sub>3</sub> , respectively. ....	60

Figure 3.5 Deconvolution of monometallic Pd (a) and Au (b) nanoparticles over A300 synthesized by SEA and DI. ....	61
Figure 3.6 Deconvoluted XRD patterns over bimetallic PdAu nanoparticles over A300 by co-SEA (a), by co-DI (b). ....	63
Figure 3.7 Deconvoluted XRD patterns over bimetallic PdAu nanoparticles over $\gamma$ -Al <sub>2</sub> O <sub>3</sub> by co-SEA (a), by co-DI. ....	63
Figure 3.8 STEM images and particle size distributions for monometallic Pd and Au NPs. ....	66
Figure 3.9 STEM images over bimetallic PdAu nanoparticles supported on A300 with varied magnifications and histograms of particle size distribution. ....	67
Figure 3.10 STEM images over bimetallic PdAu nanoparticles supported on $\gamma$ -Al <sub>2</sub> O <sub>3</sub> with varied magnifications and particle size histograms. ....	68
Figure 3.11 XPS spectra of Au4f (a) and Pd3d and Au4d (d) over single Pd, Au and Pd1Au1 NPs synthesized by electrostatic adsorption method. ....	70
Figure 3.12 IR spectra over bimetallic PdAu nanoparticles supported on (a) A300 and (b) $\gamma$ -Al <sub>2</sub> O <sub>3</sub> . ....	71
Figure 3.13 Fraction of linear-bonded CO based on deconvoluted spectra areas over A300 (a) and $\gamma$ -Al <sub>2</sub> O <sub>3</sub> supported PdAu nanoparticles. ....	72
Figure 4.1 Electrostatic adsorption of Pd, Au precursor complexes on silica support (a); Palladium and/or Pd-Au alloy formed on gold clusters after H <sub>2</sub> reduction (b). ....	77
Figure 4.2 TPR profiles of PdAu DLA catalysts and the support. ....	83
Figure 4.3 XRD analysis of the PdAu DLA series, a) Normalized XRD profiles for (1) treated SiO <sub>2</sub> , (2) Pd <sub>1.54</sub> , (3) Pd <sub>1.27</sub> Au <sub>1</sub> , (4) Pd <sub>0.227</sub> Au <sub>1</sub> , (5) Pd <sub>0.08</sub> Au <sub>1</sub> , (6) Pd <sub>0.04</sub> Au <sub>1</sub> , (7) Pd <sub>0.02</sub> Au <sub>1</sub> , (8) Pd <sub>0.012</sub> Au <sub>1</sub> , (9) Pd <sub>0.01</sub> Au <sub>1</sub> , (10) Au <sub>2.2</sub> catalysts, b) background-subtracted and fitted patterns, c) comparison of results with Vegard's law. ....	85
Figure 4.4 (a) Normalized XRD patterns for silica support and Pd <sub>0.02</sub> Au <sub>1</sub> _co-DI; (b) Deconvolution of support background subtracted X-ray patterns of Pd <sub>0.02</sub> Au <sub>1</sub> _co-DI ....	86

Figure 4.5 STEM images of monometallic Pd <sub>1</sub> _SEA (A), Au <sub>1</sub> _SEA (B), Pd <sub>1</sub> Au <sub>1</sub> _co-SEA (C) and Pd <sub>0.04</sub> Au <sub>1</sub> _co-SEA (D) catalyst at low and high magnification as well as the particle size distribution histograms. ....	89
Figure 4.6 STEM images of monometallic Pd <sub>0.04</sub> Au <sub>1</sub> /A300_co-SEA and Pd <sub>1</sub> Au <sub>0.04</sub> catalyst on carbon synthesized by co-SEA. ....	90
Figure 4.7 XPS spectra comparison of Au4f (a), Pd3d and Au3d (b) over PdAu DLA catalysts. ....	91
Figure 4.8 Time-dependent FTIR spectra over Pd <sub>1.27</sub> Au <sub>1</sub> (a) in 1% CO/Ar and (b) in the subsequent N <sub>2</sub> flow; (c-d) subtracted IR spectra on Au <sub>2.2</sub> . ....	93
Figure 4.9 IR spectra over (a) monometallic and (b) PdAu DLA catalysts. ....	95
Figure 4.10 FTIR derived fraction of linearly adsorbed CO. ....	98
Figure 4.11 (a) Concentration of acetophenone per 0.64 mmol Pd vs reaction time; (b) turnover frequency based on Pd amount. ....	100
Figure A.1 Pore size distribution of metal doped KIT5 silicas before and after hydrothermal stability tests. ....	117
Figure A.2 XRD patterns of silica supports before and post HDO reaction for 1 hr: (a) KIT5 series silicas; (b) KIT6 series silicas. ....	118
Figure B.1 FFT images for Pd <sub>1</sub> Au <sub>1</sub> /A300_co-SEA (a) and Pd <sub>1</sub> Au <sub>1</sub> /Al <sub>2</sub> O <sub>3</sub> _co-SEA (b). ....	119
Figure B.2 FTIR spectra over pure support and single Pd, Au materials: (a) on 300; (b) $\gamma$ -Al <sub>2</sub> O <sub>3</sub> . ....	120



# CHAPTER 1

## INTRODUCTION

Catalysis plays a crucial role in numerous catalytic processes such as producing fine chemicals, petroleum refining, biomass conversion, energy conservation, and so forth. Over 80% of chemical production rely on the technology of catalysis with at least one catalytic step involved [1, 2]. Catalysts can be defined as a material containing functional sites that can influence the rates of chemical reactions without changing the thermodynamic equilibrium [3].

Since the very beginning of catalysis science, catalysts had been categorized into three groups: homogenous, heterogenous, and enzymatic. The thermal stability of protein structure in enzyme restricts its application in a lot of chemical processes wherein harsh reaction conditions are required [4]. Enzymatic catalysts are mostly employed in biochemical processes. Compared with enzyme, homogenous and heterogenous catalysts have been extensively utilized in industrial manufacturing. While both of them exhibits the virtues and deficiencies [5], homogenous complexes normally are more active, but difficulties still exist in products separation and catalysts reuse. In contrast, high catalytic performance can be achieved over heterogenous catalysts only if dexterously designing the materials to optimize the active sites. Thus, to develop ideal catalysts with high activity, selectivity, and stability as well as convenient recyclability and catalyst separation, promising synthetic strategies must be designed.

From the fundamental standpoint, notably, heterogenous catalysts are the most distinguished properties including high stability upon operating in robust conditions, conducive phase-separation, and achievable high reactivity through rational design modes. Therein, supported metallic nanoparticle accounts for the majority of heterogenous catalytic materials. More importantly, the catalytic performance is remarkably influenced by metal species with different sizes and shapes [6, 7]. In case of intermetallic materials, their functions in catalytic process are also intimately related to the composition, structure, ensemble and ligand effects between/among the metals [8, 9]. Furthermore, the underlying support is as well vital to determining the catalytic performance, due to their specific physicochemical properties which can serve active sites, induce varied metal-support interactions, modify the metallic NPs, etc. [10, 11]. A growing body of evidence shows delicate and rational synthesis of metallic nanoparticles have been attracting abundant attraction due to the enhanced functions in catalytic reactions.

### **1.1 Heterogenous Catalysts Preparation**

Impregnation and precipitation are two traditional heterogenous catalyst synthesis methods, which are extensively used in industrial processes. Novel synthetic routines includes deposition-reduction, sol-gel, hydrothermal, electroless deposition, strong electrostatic adsorption, ion-exchange, galvanic displacement, etc.

Impregnation has been considered as the simplest, least expensive, and most extensively used technique to produce heterogenous catalysts, which can be categorized into dry impregnation and wet impregnation depending on the volume of the metal precursor solution. Dry impregnation (DI) is also called incipient wet impregnation (IWI), wherein a small amount (normally the water accessible pore volume) of liquid was used to

fill the support pores based on the capillary action. In contrast, excess liquid, which is far more than the support pore volume, are used in wet impregnation procedure with enhanced mixing of metal precursor and support material. While filtration is required in wet impregnation with consequently waste of metal due to the incomplete adsorption. Poor metal dispersion a critical issue which can limit the effective utilization of metal atoms. Besides, other limitations also exist, including poor solubility of some solid metal precursors, inhomogeneity in the bi-/inter-metallic alloys.

Precipitation is another widely used method to synthesize supported metal nanoparticles due to the aggregation and precipitation of the nucleated metal crystals in an aqueous mixture due to changes in the physicochemical properties of the liquid. A general scheme of precipitation is shown in Fig. 1.1 from the literature [12] (with the permission

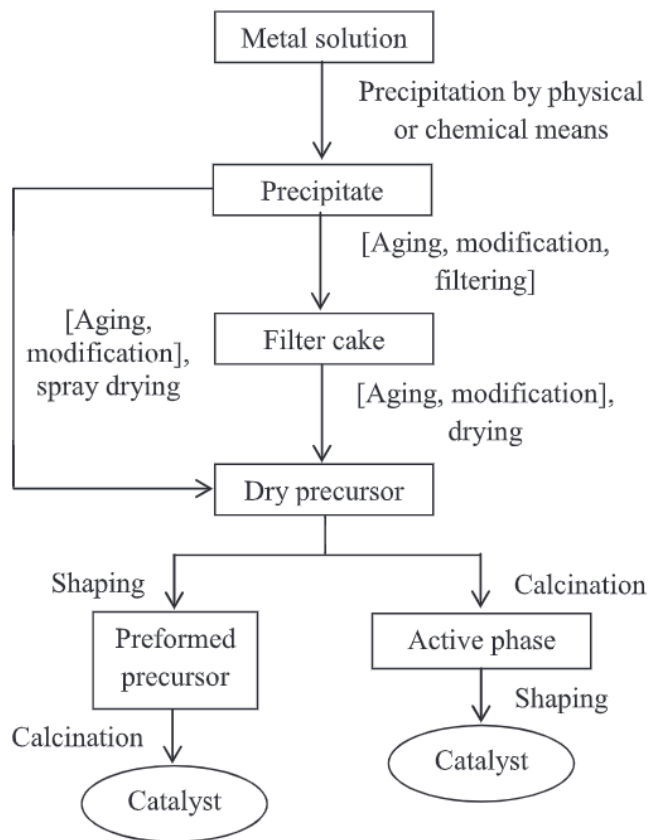


Figure 1.1 Precipitation synthetic procedure.

of copyright from Elsevier). Liquid solution with high metal concentration was controlled at a constant pH value. In terms of the low toxicity and facile decomposition, hydroxides and carbonates are usually utilized as precipitates to lead to the nucleation of the metal(s) of interest. A lot of parameters can be governed during the precipitation process to tune the metal dispersion, such as solution temperature, pH value, metal concentration, aging time, thermal treatment temperature and so forth. Bimetallic nanoparticles can be obtained by co-precipitation of two different metal complexes.

Sol-gel method is a wet chemical protocol to obtain metal nanoparticles with well-controlled structures, textures and alloying homogeneity. In this method, metal precursor was dissolved into a solvent, converted to gel by hydrolysis and the desired nanoparticles were formed after various hydrothermal treatments. The synthetic scheme of sol-gel method was given in Fig.1.2 from the literature [13]. The physicochemical property of the nanoparticles can be tailored by the concentration and type of metal precursor, solution pH, solvent, aging time, additives (chelate, template, surfactants, structure directing agents), substrate, etc. [14].

In the deposition-reduction synthetic approach, direct deposition of metal nanoparticles onto the support can be obtained through the addition of a soluble reducing agent into a suspension containing support and the metal of interest. The selection of solvent, reduction agent, metal complex precursor, modification for the support is crucial to achieve a satisfactory catalyst [15]. The drawbacks from this recipe arise when the active metal is incapable of completely and uniformly encapsulated into the porous framework of support materials.

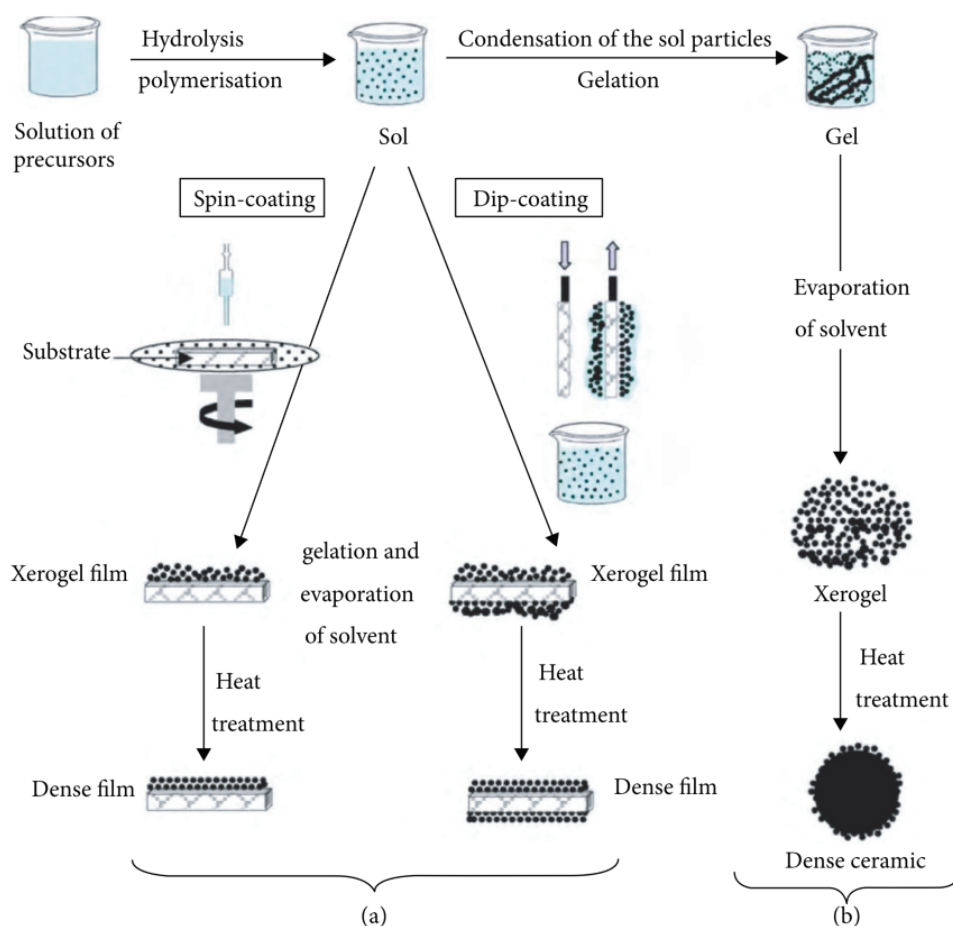


Figure 1.2 Schematic synthesis through sol-gel method, (a) film-based, and (b) powder nanoparticles.

The core of hydrothermal synthesis recipe is sealing the aqueous solution with metal precursor and alkali at high pressure and temperature in an autoclave for a certain period of time. Crystals with metal atoms can be nucleated and grown and the subsequent dry and reduction process would yield metal nanoparticles. Scheme of catalysts preparation by thermal synthesis [16] is displayed in Fig.1.3. Small particle size with uniform distribution, high purity, controllable morphology can be obtained by carefully tuning the nucleation speed, temperature, pressure, surfactant, solution pH, etc.

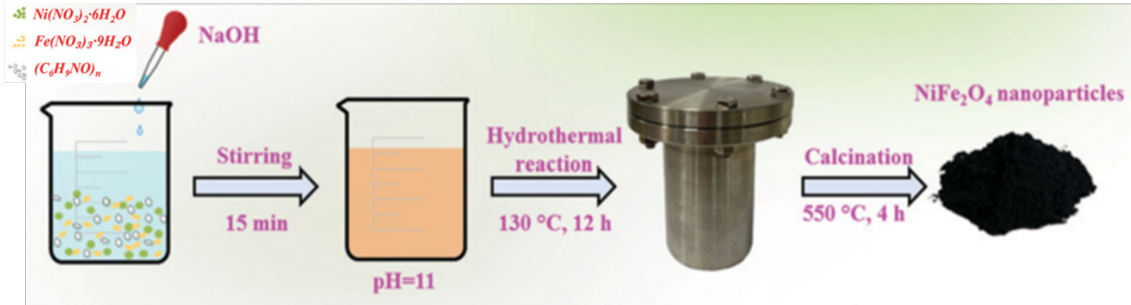


Figure 1.3 Schematic representation of catalysts by hydrothermal synthesis method.

Electroless deposition is another novel technique to prepare supported metal nanoparticles as well as for metal-plating, which can be categorized into three kinds: (a) Galvanic displacement reaction; (b) using a reducing agent to deposition a reducible metal salt onto the surface of the existing metal based on their reduction potential; (c) disproportionation reaction [17]. In the catalysts preparation by electroless deposition, identical metal can be deposited, which could effectively grow the particle size. While the deposition of a different metal with a higher reduction potential will lead to a core-shell structure with tuned thickness of the shell [18]. In this approach, reducing agent selection, solution control, deposition rate and other parameters are critical to the success of the catalysts synthesis.

Ion exchange is a reversible chemical reaction between the soluble ions and the charged surface of a porous solid, which can be used in catalyst synthesis. Commonly, ion-exchange approach involves contacting support material with solution containing complexed metal ions at a constant pH for a period of time, wherein, metal ions replace the ion counters on the surface of the support due to a strong electrostatic adsorption.

Strong electrostatic adsorption (SEA) is a novel routine to prepare ultra-small metal nanoparticles, which can also be considered as a modified wet impregnation approach, therein anionic or cationic metal precursors are strongly adsorbed onto oppositely charged support surface due to the coulombic attraction by controlling solution pH. Fig.1.4 illustrates how the SEA mechanism works. The presence of hydroxyl OH on the terminal of oxide and carbon surface is to compensate the charge deficiency [19], which can be protonated or deprotonated. Point of zero charge (PZC) of a support, also known as the isoelectric point, is the pH the surface hydroxyl groups are neutral. As shown in Fig. 1.4, if the solution pH is higher than the PZC of the support material, the surface OH groups would be deprotonated and can adsorb cationic metal precursors; below PZC, support surface will be protonated and positively charged, and can attract anionic metal complexes. At the optimal pH, hydroxyl groups can be fully charged and adsorb the maximum metal precursors, which can be derived from the adsorption survey of this metal precursor on the support.

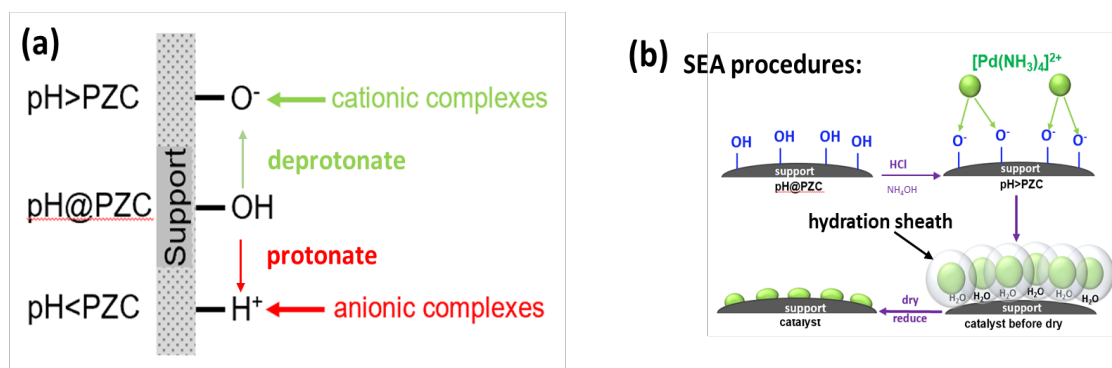


Figure 1.4 (a) Scheme of SEA mechanism; (b) SEA synthetic procedure.

Surface loading is defined as surface area of the support in the unit of solution volume. More support added into a fixed volume of aqueous solution, the higher the surface loading, which can be calculated according to Equation 1.1. Due to the numerous hydroxyl groups on the surface of support materials, a buffering effect has been observed especially at a high surface loading. When enough support contacts with small amount of water, like the thick slurry in the dry impregnation, final pH reaches the PZC of the material with the equilibrium of protonation-deprotonation. Whereby, support surface is neutrally charged and there is no electrostatic adsorption between support and metal precursors. The buffering effect of  $\gamma$ -Al<sub>2</sub>O<sub>3</sub> at varied surface loadings [20] were depicted in Fig.1.5.

$$SL (m^2/L) = \frac{SA \left( \frac{m^2}{g} \right) * m (g)}{V_{\text{solution}} (L)} \quad \text{Equation 1.1}$$

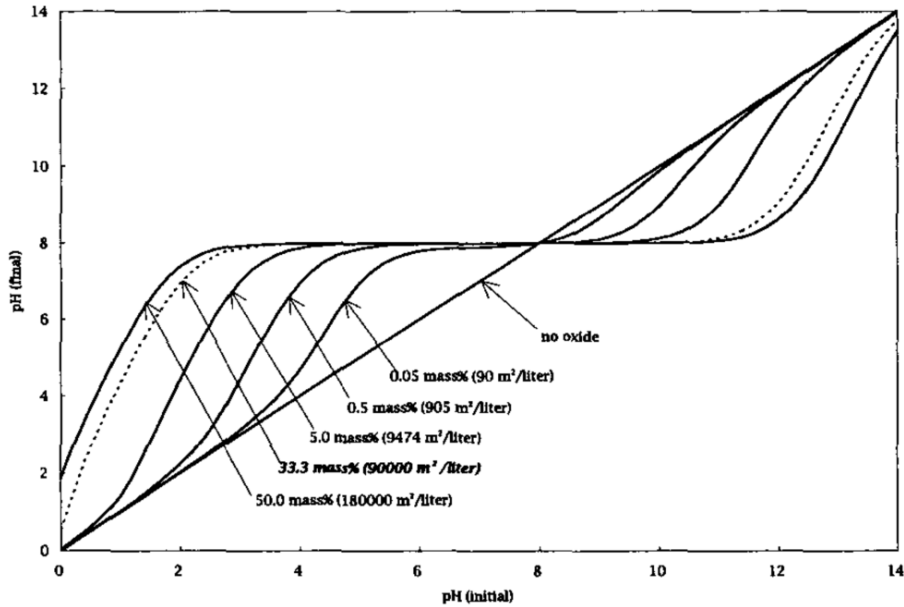


Figure 1.5 Simulation on the pH shift of  $\gamma$ -Al<sub>2</sub>O<sub>3</sub> with surface loadings (PZC=8.0, DpK=5.0, SA=180 m<sup>2</sup>/g).



In the simulation of the experimental adsorption of anionic and cationic metal complexes through revised physical adsorption (RPA) model, anion adsorbs onto the support with one hydration sheath while cation is believed to retain two [21]. Generally, the maximum adsorption density can be calculated by a steric monolayer of hydrated complexes, according to Equation 1.2 ( $r_{ion}$ : ion radius,  $r_w$ : water molecule radius,  $n$ : number of hydration sheath) [22]. In the case of Pt and Pd, calculated maximum adsorption of ions ( $\text{PdCl}_2^{2-}$  or  $\text{PtCl}_6^{2-}$ ) is around  $1.6 \mu\text{mol}/\text{m}^2$ , whereas it is about  $0.82 \mu\text{mol}/\text{m}^2$  for cations [ $\text{Pd}(\text{NH}_3)_4^{2+}$ ,  $\text{Pt}(\text{NH}_3)_4^{2+}$ ]. The uptake survey of over various PZC materials were shown in Fig.1.6 [23]. The fall-off in the metal adsorption past the optimal pH (above high PZC and below low pH) is resulted from the strong ionic strength due to the addition of excess basic or acidic solution, which screens the charged hydroxyl groups from the metal complexes [24]. Thus, it is crucial to figure out the optimal pH in the strong electrostatic adsorption method.

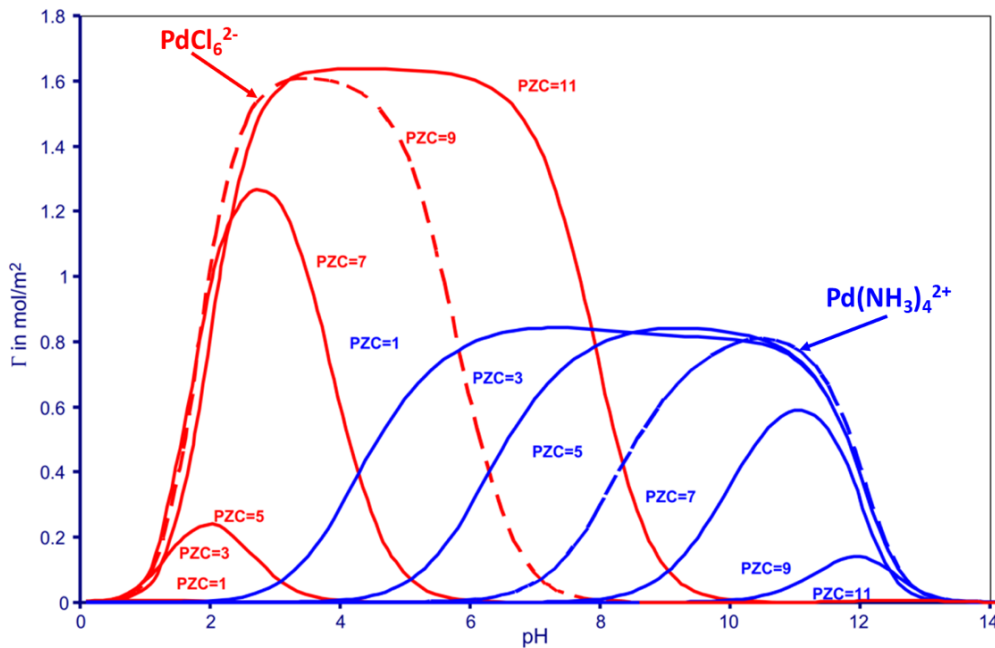


Figure 1.6 Adsorption survey of Pt ions and cations over various PZC materials vs pH.

$$\Gamma_{\max} = \frac{1}{N_0 * \pi * (r_{ion} + n * r_w)} \quad \text{Equation 1.2}$$

The elaborate procedures in SEA synthetic approach include: (1) PZC determination; (2) buffering effect of support material without metal precursors; (3) adsorption survey of active metal; (4) catalysts preparation. The PZC of a support can be measured by using a spear-tip semisolid electrode over the thick paste of the porous material with a very high solid/H<sub>2</sub>O ratio with the pH of water being adjusted at 3, 6.7, and 9, then take the average of the three measured final pH values. The corresponding (anionic or cationic) metal complex is selected based on the range of the support PZC. In the uptake survey of the active metal, initial pH values were determined on the basis of the above pH shift of the pure support, targeting to get evenly distributed points in adsorption plots in the investigated pH range. Besides, the adsorbed density ( $\mu\text{mol}/\text{m}^2$ ) is calculated by Equation 1.3. Then, the maximum metal adsorption and the corresponding optimal final pH can be acquired. In the catalyst preparation, the initial metal concentration is determined by Equation 1.4. In excess of 10% of the initial concentration was used in the calculation. The actual deposition of the active metals is determined by ICP using Equation 1.3.

$$\Gamma \left( \frac{\mu\text{mol}^2}{\text{m}} \right) = \frac{(C_{\text{initial}} - C_{\text{final}}) \left( \frac{\mu\text{mol}}{\text{L}} \right)}{SL (\text{m}^2/\text{L})} \quad \text{Equation 1.3}$$

$$C_{\text{initial}} \left( \frac{\text{mg}}{\text{L}} \right) = \frac{\frac{\text{m}_{\text{wt}}(\%)}{100} * m_{\text{support}}}{V_{\text{solution}}(\text{L})} = \frac{\frac{\text{m}_{\text{wt}}(\%)}{100} * SL(\text{m}^2/\text{L})}{SA (\text{m}^2/\text{g})} \quad \text{Equation 1.4}$$

A great deal of the work in our group has demonstrated that ultra-small metal (e.g. Pt, Pd, Ru, Cu, Ni, Co, Au, Rd, Ag, etc.) nanoparticles can be synthesized over numerous supports (e.g. SiO<sub>2</sub>, Al<sub>2</sub>O<sub>3</sub>, TiO<sub>2</sub>, CeO<sub>2</sub>, ZrO<sub>2</sub>, Nb<sub>2</sub>O<sub>5</sub>, Fe<sub>2</sub>O<sub>3</sub>, carbon, etc.). The generally used support materials as well as metal anions and cations were summarized in Table 1.1. Moreover, an anionic or cationic metal complex can selectively deposit onto the specific oxide in a support mixture by controlling the solution pH or using differently charged metal complexes. For instance, Pt was selectively adsorbed onto silica or alumina in their mixed oxides by [Pt(NH<sub>3</sub>)<sub>4</sub>]<sup>2+</sup> or using (PtCl<sub>6</sub>)<sup>2-</sup> in their appropriate pH range [25]. Moreover, strong electrostatic adsorption method has been successfully extended to produce well-dispersed bimetallic nanoparticles with homogenous alloys [26], core-shell structure [27], dilute limit alloys [28], etc.

Table 1.1 The normal high and low PZC support materials, metal anions and cations.

metal cations	metal anions	high PZC materials	low PZC materials
[Pd(NH <sub>3</sub> ) <sub>4</sub> ] <sup>2+</sup>	(PdCl <sub>4</sub> ) <sup>2-</sup>	Al <sub>2</sub> O <sub>3</sub>	SiO <sub>2</sub>
[Pt(NH <sub>3</sub> ) <sub>4</sub> ] <sup>2+</sup>	(PtCl <sub>6</sub> ) <sup>2-</sup>	ZrO <sub>2</sub>	TiO <sub>2</sub>
[Au(en) <sub>2</sub> ] <sup>3+</sup>	(AuCl <sub>4</sub> ) <sup>-</sup>	CeO <sub>3</sub>	BaTiO <sub>3</sub>
[Rh(NH <sub>3</sub> ) <sub>5</sub> Cl <sub>2</sub> ] <sup>3+</sup>	(RhCl <sub>6</sub> ) <sup>3-</sup>	Fe <sub>2</sub> O <sub>3</sub>	Nb <sub>2</sub> O <sub>3</sub>
[Ag(NH <sub>3</sub> ) <sub>2</sub> ] <sup>2+</sup> , [Cu(NH <sub>3</sub> ) <sub>2</sub> ] <sup>2+</sup>	---	Cr <sub>2</sub> O <sub>3</sub>	WO <sub>3</sub>
[Co(NH <sub>3</sub> ) <sub>2</sub> ] <sup>2+</sup> , [Ni(NH <sub>3</sub> ) <sub>2</sub> ] <sup>2+</sup>	---	Sb <sub>2</sub> O <sub>3</sub>	ZnO
etc.	---	oxidized carbon	carbon

The technique of the maximized metal-support interaction at the optimal pH in SEA preparation protocol can be used to modify the dry impregnation method, namely charge enhanced dry impregnation (CEDI). Therein, a high ratio of solid to liquid is applied according to the water accessible pore volume as described in DI synthetic procedure. Whereas the solution pH is adjusted to the optimal pH obtained from the uptake survey in SEA method by using the same support and metal precursor while a lower surface loading. In this case, metal-support can be enhanced, and a great deal of metal complex is adsorbed onto the support surface, which can normally produce small particles. Our work on deposition of Pt, Pd, Ni, Cu, Co onto silica by using DI, CEDI and SEA showed that small nanoparticles of mono-/bi-metallic NPs can be obtained by CEDI method which is much more effective without washing than DI. Generally, the particle size obtained follows the order: SEA < CEDI < DI.

Catalyst synthesis methods along with their advantages/disadvantages and the controllable parameters in the preparation procedures were listed in Table 1.2.

## **1.2 Catalysts characterization**

Catalysts physicochemical properties, including the composition, structure, metal state, and so forth, can be verified by various characterization techniques, which could inversely help us to explore the strategies in the catalyst synthesis.

Temperature programmed reduction (TPR) is a useful tool to verify the reduction temperature of metal precursor salts and the ligands removal. The overall composition of the metallic nanoparticles can be identified by inductively coupled plasma (ICP) or atomic adsorption spectroscopy (AA). X-ray fluorescence (XRF) can also be used to check the bulk content of catalytic material, while it is merely precise if the concentration of active

metal is high. Particle size analysis can be conducted by XRD, TEM, and chemisorption characterization. Peak fitting over background subtracted XRD profiles is able to certify metal phase and the corresponding particle size by Scherrer equation. EDXS can analyze the regional element distribution. Electronic structure of the metallic nanoparticles can be acquired by XPS and IR analysis. Temperature programmed desorption (TPD) with the adsorbate molecules can effectively quantify the amount of surface active sites (CO<sub>2</sub> for basicity, NH<sub>3</sub> for acidity, etc.). Combination of IR analysis and chemisorption can give the information of surface composition.

Table 1.2 Catalyst synthesis summary.

<b>synthetic approach</b>	<b>liquid/solid volume ratio</b>	<b>advantage</b>	<b>disadvantage</b>	<b>parameter</b>
dry impregnation	small	simple, fixed metal loading	poor dispersion, solubility of metal precursor	---
charge enhanced dry impregnation	small	small particle	solubility of metal precursor	solution pH
wet impregnation	large	simple, improved mixing	metal waste	liquid/solid ratio
precipitation	large	large metal loading	poor dispersion	pH, metal concentration, aging time, etc.
sol-gel	large	high dispersion	time consumed, complex	metal precursor, pH, solvent, aging time, additives, etc
deposition-reduction	large	high dispersion	metal waste	reducing agent, solvent, modification of support, metal precursor
hydrothermal	large	small particles, high purity	high pressure and temperature, time consuming	temperature, pressure, surfactant, pH, nucleation speed
electroless deposition	large	controllable particle size	metal selection	reducing agent, pH, metal concentration
ion-exchange	large	small particle	pH, limitation in metal precursor and support	pH, metal precursor, additives
strong electrostatic adsorption	large	ultra-small particles, simple, time effective	metal loading, stability of metal precursor	pH, liquid/solid

### 1.3 Bifunctional and Bimetallic Catalysts

In the complex reaction systems or reactions carried in harsh conditions, such as biomass conversion, fossil fuel refining, and so forth, numerous cascade and parallel reaction steps are involved, and distinctive active sites are required to get the desired product [29, 30]. Due to the limitations of monofunctional catalytic materials with single active site (low activity and selectivity, more purifications steps, time-consuming, etc.), the development of bi-/multi-functional catalysts have attracted great attentions in both academic and industrial fields in the green energy evolution.

Evidently, the concept of bifunctional catalysts is the materials contain two variety of active sites which can catalyze two tandem reaction steps. Compared to monofunctional catalysts, the unique advantage of this type of materials is its high efficiency in converting the active intermediate into the product in mind with high selectivity and less purification steps. Generally, bifunctional catalysts can be mainly divided into two categories: metal-acid/basic and bimetallic [31].

Metal-acid/basic bifunctional catalysts can be prepared by directly depositing metal sites onto metal oxide supports with acidic or basic property. While the neutral material like silica can also be used as the support by doping metals (W, Zr, Ce, Nb, Ti, etc.) to introduce acidity or basicity. The tunable properties of metal-acid/basic materials which can influence the reactivity exclusively conclude metal-support interaction, the amount and of metal and acidic or basic sites, metal dispersion. However, reduction in metal particle size can certainly increase the utilization of metal atoms and enhance the catalytic activity to some extent. In the case of bimetallic catalysts, the addition of a secondary metal could modify the geometric and electronic structure of the primary metal with the significant

enhancement in the catalytic performance. Besides, the composition, structure, morphology can be readily tuned by employing a promising synthetic approach.

#### **1.4 Dilute Limit Alloy Catalysts**

The geometry of the active sites is crucial in catalytic activity as the reduction in metal particle size can certainly increase the utilization of metal atoms with exceptional performance. The extreme of shrinking the monometallic metal particle size is single atom catalysts. However, due to the lack of metal-metal bond in single atom catalysts, it is reported that the dissociation of  $H_2$  would go through a distinct pathway which might have a higher barrier and the competitive adsorption and the subsequent dissociation of  $H_2$  and the reactant would be another issue in the reaction [32].

However, dilute limit alloy catalysts have been proposed due to its advantages of single atom catalysts and traditional alloyed materials. Dilute limit alloy catalysts can be defined as diluting the active metal into atomic level in another bulk method nanoparticles with the formation of isolated active sites, unique electronic structure, tunned composition [33]. The formation of the active metal monomers also maximizes the noble metal utilization efficiency; the controllable composition and structure through a rational design can influence the electronic structure of the isolated species which could significantly influence the catalytic performance.

## CHAPTER 2

# SYNTHESIS OF METAL-ACID BIFUNCTIONAL CATALYSTS ON HIERARCHICALLY MESOPOROUS SILICA FOR METHYL- GUAIACOL HYDRODEOXYGENATION UNDER MILD CONDITION

### 2.1 Abstract

In this chapter, a series of bifunctional catalysts with tuned metal/acid ratios on hierarchically mesoporous silica was prepared, characterized, and examined for hydrodeoxygenation (HDO) of methyl-guaiacol (M-GUA) under mild reaction condition at 112 °C, 12.5 bar. Tuned amounts of acid sites and surface palladium sites were achieved by doping W, Zr, or Nb into silicas matrices and by using distinct synthetic techniques, respectively. Experimental results elucidate metal (W, Zr, Nb)-containing KIT5 and KIT6 supports exhibits ordered three-dimensional mesopores and high hydrothermal stability in reaction condition. The HDO performances were strongly governed by surface palladium sites and acid sites. Palladium is responsible for the hydrogenation reaction and acid sites are indispensable for the deoxygenation of the hydrogenated intermediates. Catalysts synthesized by strong electrostatic adsorption (SEA) displayed higher reactivity due to ultra-small palladium particles. Furthermore, the introduction of acid sites enhanced the activity with a higher deoxygenated rate. Highest reactivity (97% conversion, 100% hydrogenated and >20% selectivity to deoxygenated products) was observed over Nb-



containing catalysts prepared by SEA method after 4 h, which can be ascribed to the optimal ratio of acid/metal balance. XRD analysis on spent catalysts suggests trivial particle sintering over SEA prepared catalysts, while particle reconstruction with decreased particle size was detected on DI samples.

## 2.2 Introduction

The limited supply of fossil fuels strongly motivates the search for alternatives like bio-oil, heavy or extra-heavy oil, shale oils, and oil sand, which take up over 70% of the world's oil reserves [34, 35]. However, the direct utilization of bio-oil and (extra-) heavy oils is impeded because of the high viscosity caused by massive oxygen-compounds in bio-oil, deficiency in hydrogen of (extra-) heavy oil, low thermal stability, etc. [36-39]. Thus, considerable efforts have been made to develop the methods of bio/heavy-oil quality improvement, such as catalytic cracking, hydrodeoxygenation, esterification, emulsification, etc. [34, 36, 40, 41]. Among these upgrading processes, hydrodeoxygenation reaction has been considered as the most conducive form for future industrial applications due to its high efficiency in facilitating the calorific value of bio-oil through increasing H/O ratio in the organic compounds [42-44].

In general, HDO reactions in the upgrading process of bio-oil are normally carried out under harsh conditions (e.g., high temperature and pressure). The high-severity hydrotreating process involving complete hydrodeoxygenation with minimal hydrogenation is normally maintained at 350 - 400°C at greater than 200 bar of H<sub>2</sub>, and for the low-severity hydrotreating with partial hydrodeoxygenation and reasonable hydrogenation, the temperature is controlled at 175 - 250°C with the pressure higher than 100 bar [45]. M. Zhang et al [38] summarized that bio-oil HDO efficiency can be improved

in the temperature range of 300 – 350 °C and high H<sub>2</sub> pressure like 10 - 30 MPa. Y. Xiao and the colleagues [46] disclosed that in gas-phase HDO reaction of guaiacol over Pt-M (Nb, W, Zr)/KIT6 catalysts, guaiacol wasn't activated until reaction temperature reached 250 °C.

However, multistep reactions involved in HDO process especially in harsh conditions, and a wide distribution of various chemicals were produced from several parallel and cascade reactions based on reaction conditions and catalysts applied [47-49]. To get the desired products, different active sites are required for various reaction steps. While monofunctional catalytic materials with single active site are insufficient in catalyzing several different reactions and the application of multiple monofunctional catalysts with various active sites in one batch or sequential utilization faces several challenges, such as inefficiency, poor product selectivity, and more purification steps [29, 49, 50].

Hence, bi-/multi-functional materials with disparate active sites open a door for carrying out cascade- and parallel-reactions in one batch [29, 30]. Adjacent active sites with multifunctionality are capable to tandemly perform a surface-catalyzed reaction to fulfill complementary reaction steps, so the isolation or purification steps to remove the unwanted by-products can be lessened or eliminated [29, 42, 51]. It is reported that active metal sites are indispensable to the hydrogenation reaction while acid sites from the supports can catalyze the deoxygenation of oxygenates [52-54]. K.G.M. Figueredo et al [55] discovered that, over Pd, Rh catalysts on SiO<sub>2</sub>-Al<sub>2</sub>O<sub>3</sub>, the acid sites could catalyze the ring-opening of  $\gamma$ -Valerolactone to 4-hydroxy pentyl valerate then to pentyl 2-pentenoate, which was finally hydrogenated to the desired product of pentyl valerate on the adjacent

active palladium or rhodium site. Wherein, the whole process occurred in one batch and could efficiently avoid side reactions. H. Kim et al [56] found that both the reaction pathway and product distribution were substantially influenced by the metal/acid balance of the catalysts in the HDO reaction of vanillin.

It is well acknowledged that ordered mesoporous materials with tunable pore structure and high surface area are attracting considerable attention because of the promoted mass transport, active sites utilization and fabulous coke-resistance, especially in reactions involving bulky molecules. Y. Wang et al [57] discovered that mesoporous ZSM-5 supported Pd catalysts exhibits superior activity and anti-coking performance than the ones on conventional microporous ZSM-5 counterparts, attributed to the fast diffusion and easy accessibility for reactants and/or products. Besides, compared with materials owning one-dimensional array of pores, 3D mesoporous silicas such as KIT-5 with interconnected cage-type pores and KIT-6 owning ultra-large-pore network are preferred, because bulky reaction intermediates can be accommodated inside [58, 59]. X. Wang and the colleagues [60] argued that the admirable catalytic activity of Ni/H $\beta$ -zeolite in HDO of guaiacol was facilitated by its open pore with 3D structure. Furthermore, the acid sites introduced into nonacidic silica are reported as catalytically active species [58, 59, 61-63]. Hierarchically mesoporous KIT5 and KIT6 silicas with 3D - structures can be readily synthesized via hydrothermal method and the number of acid sites can be tuned by doping metals, such as W, Zr, or Nb with varied acidic properties, into their framework [61, 64, 65]. Afterwards, they can be employed as catalyst supports in view of the 3D pore structure and the acidic species.

Palladium is extensively used as active metal species for hydrogenation, oxidation, oxygen reduction, cross-coupling related reactions [66-69]. Synthesis of ultra-small Pd NPs is of great interest in terms of the tremendous improvement in metal utilization efficiency. Strong electrostatic adsorption (SEA) is an effective technique to synthesize highly dispersed palladium nanoparticles, wherein charged metal precursors are strongly adsorbed onto oppositely charged supports [26, 70]. At the optimal pH, the support is charged to the greatest extent and the metal-support interaction is the strongest, which generates ultra-small nanoparticles. In this study, Pd-based bifunctional catalysts supported on metal (W, Zr, Nb) – doped KIT5 or KIT6 silicas were synthesized by strong electrostatic adsorption (SEA) to attain ultra-small palladium nanoparticles. For the sake of comparison, bifunctional catalysts were also prepared by incipient wet impregnation (IWI), with larger nanoparticles due to the poor metal-support interaction [71]. Low temperature N<sub>2</sub> physisorption, powder X-ray diffraction, H<sub>2</sub>-chemisorption, NH<sub>3</sub>-TPD, ICP, hydrothermal stability test was utilized to characterize the as-prepared materials. Then, bifunctional catalysts were examined for HDO of 4-methyl guaiacol under mild condition at 112 °C, 12.5 bar H<sub>2</sub>.

## **2.3 Experimental**

### **2.3.1 Materials**

Tetraethyl orthosilicate (TEOS 98%, Aldrich), sodium tungstate (Acros Organics), Zirconium (IV) oxychloride octahydrate (99.5% Sigma–Aldric), Niobium(V) chloride (99%, Strem Chemicals) were used as silicon, W, Zr and Nb source, respectively. Tetraamminepalladium (II) chloride monohydrate (PdTACl) (Sigma-Aldrich >99.99%), 4-methyl-guaiacol (≥98%) and Ethyl Ether anhydrous (>99.5%) was purchased from Sigma

Aldrich. Hydrochloric acid (HCl) and ammonia hydroxide (NH<sub>4</sub>OH) was procured from Alfa Aesar. H<sub>2</sub> and N<sub>2</sub> in UHP level was obtained from Praxair. All the chemicals and gases were used directly from the vendors without any purification treatment.

### **2.3.2 Synthesis of Supports and Bifunctional Catalysts**

The used pure or metal (W, Zr, Nb)-containing mesoporous KIT5 or KIT6 silica were provided by Dr. Bala Subramaniam's group in the University of Kansas University. They were prepared through hydrothermal synthesis method according to the literature [58, 59, 61, 64, 65, 72] with the molar ratio of Si/M (M=W, Zr, Nb) as 20. Metal doped silicas were presented as W-KIT5 (6), Zr-KIT5 (6), Nb-KIT5 (6).

To explore the optimal pH at which strongest metal-support interaction occurs, palladium adsorption surveys were carried out on the prepared silicas. The amount of support in the solution was controlled by support surface area, surface loading (SL=1000 m<sup>2</sup>/L) and solution volume (V=25 mL). Palladium ammine solution (200 ppm) pH was adjusted by HCl and NH<sub>4</sub>OH. Support added solution was placed on an orbital shaker at 120 rpm for 1h. Solution of 5 mL was taken out before and after contacting support to determine the metal adsorption densities from the difference in palladium concentration. Meanwhile, the initial and final pH was recorded to evaluate the optimal pH for palladium adsorption.

Palladium was deposited onto the as-prepared mesoporous silicas through SEA technique at the optimal pH achieved from the adsorption survey. Concentration of PdTACl solution was determined according to the target loading (2.5 wt %). To get a comparison, catalysts with the same palladium loading were also synthesized via IWI by using water accessible pore volume. All the synthesized wet catalysts were dried at room

temperature for 48 h followed by reduction treatments in a horizontal reduction furnace in 200 sccm 20% H<sub>2</sub>/N<sub>2</sub> at 240 °C for 1h at a ramp of 5 °C/min. Catalysts were denoted as Pd5/S, PdZr5/S, PdNb5/S, Pd5/D, PdZr5/D, PdNb5/D, where 5 stands for the KIT5 silica, S or D is on behalf of SEA or DI preparation method. Similar abbreviation was applied for bifunctional catalysts over metal doped KIT6 silica.

### **2.3.3 Characterization Techniques**

The solution (DI water or containing metal complex salts) pH was adjusted over a normal pH meter (ORION STAR A211). During the pH shift and adsorption survey of active metal complex onto the support material of interest, even spaced initial pH values were obtained by adjusting the solution by concentrated acidic or basic solution.

The point of zero charge (PZC) of the support material was measured by using a specific spear-tip pH meter (ATI orion Expandable Ionanalyzer EA 940). Three points PZC measurement were carried out with the pH of DI water at 3.0, 6.7, 9.0. The volume of water mixed with the specific amount of support was determined by water accessible pore volume to get a paste slurry and then the spear-tip of the pH meter was assured to merge into it. Three final pH values were obtained at the initial pH at 3.0, 6.7, and 9.0. The PZC was taken the average of the three final pH.

Specific surface area (BET) and pore structure (BJH) of pure and metal (W, Zr, Nb) containing KIT5 or KIT6 silicas was obtained by N<sub>2</sub> physisorption measurements on Micromeritics ASAP 2020. Samples were degassed at 300 °C for 3 h and then analyzed under 77.35 K in N<sub>2</sub>.

An inductively coupled plasma equipped with an optical emission spectrometer (PerkinElmer Avio 200 ICP-OES) was used to check the initial and final palladium

concentrations in the adsorption survey and catalysts preparation via SEA recipe, as well as to investigate any possible leaching of W, Zr, Nb during thermal stability tests, as well as Pd leaching during the reaction.

To verify palladium particle size and the support crystallinity, powder X-ray diffraction (XRD) patterns were recorded using a Rigaku MiniFlex II benchtop diffractometer with a high sensitivity D/tex Ultra Si slit detector. Scans were performed from 10-90 ° 2 $\theta$  with step size of 0.02 ° operated at 30 mA and 15 kV with a Cu-K $\alpha$  radiation source ( $\lambda=1.5406$  Å). Fityk software was used to deconvolute background subtracted XRD patterns with Gaussian shapes and the size of Pd NPs was calculated by Scherrer equation with a shape factor of 0.94 [73].

Pulse H<sub>2</sub> chemisorption over O<sub>2</sub> pre-covered bifunctional catalysts was employed on Micromeritics 2920 equipped with a TCD. Samples were pretreated in the U-tube at 180 °C in 10% H<sub>2</sub>/Ar for 1h, cooled down to 40 °C, contacted with 10 % O<sub>2</sub>/Ar for 45 min to attach oxygen onto the accessible palladium atoms, switched to argon to remove gaseous and physisorbed O<sub>2</sub>, and then titrated with 10% H<sub>2</sub>/Ar. Spherical palladium particle size and the dispersion was achieved by using the stoichiometry H/Pd=0.667 [74].

To explore the acidity of catalysts and supports, ammonia temperature programmed desorption (NH<sub>3</sub>-TPD) was conducted on a Micromeritics Autochem 2910 instrument equipped with an Inficon Transceptor 2 mass spectrometer (MS). About 150 mg sample was loaded into a vertical flow quartz tube, pretreated in 10 % H<sub>2</sub>/Ar at 180°C for 1h, cooled down to room temperature, exposed to ammonia for 45min to facilitate the adsorption of ammonia, purged Ar at 100°C to remove gaseous and physisorbed ammonia

molecules until the baseline was stable, then heated to 650 °C in argon at a ramp of 10 °C/min and the desorbed NH<sub>3</sub> was monitored by MS.

### **2.3.4 Catalysts Evaluation and Thermal Stability Test**

The hydrodeoxygenation of 4-methyl guaiacol (M-GUA) was carried out at 112 °C, 12.5 bar H<sub>2</sub> with stirring at 900 rpm. In the HDO reaction, 100 mg of sample was added into a 100 mL stainless steel autoclave batch reactor, 50 mL DI water and 1 mL aqueous 4-methyl guaiacol was charged. After installing the vessel, the reactor was purged with N<sub>2</sub> five times to remove the air inside; purged with H<sub>2</sub> another five times to remove the N<sub>2</sub> inside; then the reactor was pressured with H<sub>2</sub> to 12.5 bar at room temperature and heated to 112 °C without stirring to minimize any reaction; when the temperature was stabilized at 112 °C, stirring speed was rapidly increased to 900 rpm which as denoted the start of the test or reaction.

During the reaction, samples were withdrawn from the vessel after the reaction was initiated at: 0 min, 10 min, 30 min, 45 min, 1 h, 2 h, 3 h, 4 h for SEA prepared catalysts and 0, 30 min, 1 h, 2 h, 4 h, 6 h, 8 h for DI samples. Ten times of ethyl ether was used to extract the products from the liquid phase samples. Subsequently, the organic chemicals in the ethyl ether layer were analyzed by Gas Chromatography-Mass Spectrometry (GC-MS). The GC-MS analysis was performed using a Shimadzu QP-2010S with a 30 m long Rxi-5 ms Restek separation column with a 0.25 mm inner diameter. The oven temperature program was started at 40 °C for 0.5 min, followed by a 10 °C/min increase in temperature up to 140 °C, at which the temperature was held constant for two minutes. The conversion of M-GUA, product selectivity and reaction rate were determined by using the equations below:



$$\text{Conversion (\%)} = \frac{C(\text{M-GUA})_{\text{initial}} - C(\text{M-GUA})_t}{C(\text{M-GUA})_{\text{initial}}} \times 100 \% \quad \text{Equation 2.1}$$

$$\text{Selectivity (\%)} = \frac{C(\text{product})_i}{\sum_i C(\text{product})} \times 100 \% \quad \text{Equation 2.2}$$

$$\begin{aligned} \text{Rate}_{\text{react}} (\text{mmol} \cdot \text{g}^{-1} \cdot \text{min}^{-1}) \\ = \frac{\text{Converted (M-GUA)}_t}{\text{Reacted time} \times \text{Mass of catalysts}} \times 100 \% \quad \text{Equation 2.3} \end{aligned}$$

Hydrothermal stability test over the supports was performed in the same condition to the HDO reaction of M-GUA except for reactant (none added). Hydrothermal stability tests were conducted in 12.5 bar H<sub>2</sub> or N<sub>2</sub> for 1h in the same procedure as HDO reaction. After completing the thermal stability test and HDO reactions, stirring was stopped, heating jacket was removed from the vessel with chilling water on to cool down the reaction system to room temperature. Then the pressure of the reactor was released, liquid phase samples and the solid catalysts were collected for ICP and XRD analysis, respectively.

## 2.4 Results and Discussion

### 2.4.1 Support Characterization

N<sub>2</sub> physisorption isotherm curves of KIT5 or KIT6 series silicas in Fig. 2.1a-b presented a typical irreversible type-IV isotherm, characteristic of mesoporous materials [75, 76]. H<sub>2</sub> hysteresis loop was observed on KIT5 series silicas with a sharp capillary condensation ranging in 0.5-0.7 of P/P<sub>0</sub>, which is the representative of high network effects

with a narrow range of pore necks. A. Ramanathan et al [64] reported a cubic three-dimensional mesoporous structure on W-doped KIT5 material. In addition, pore size distribution of metal doped KIT5 in Fig. 2.1c suggests bimodal pores with pore neck lower than 3 nm and bulky pores above 5 nm. While, metal-doped KIT6 silicas revealed H1 hysteresis loop in 0.7-0.8 P/P<sub>0</sub> with parallel adsorption and desorption curves, indicating highly ordered large and uniform mesopores [65]. Pore size distribution patterns in Fig.2.1d suggests KIT6 series silicas exhibited larger pores.

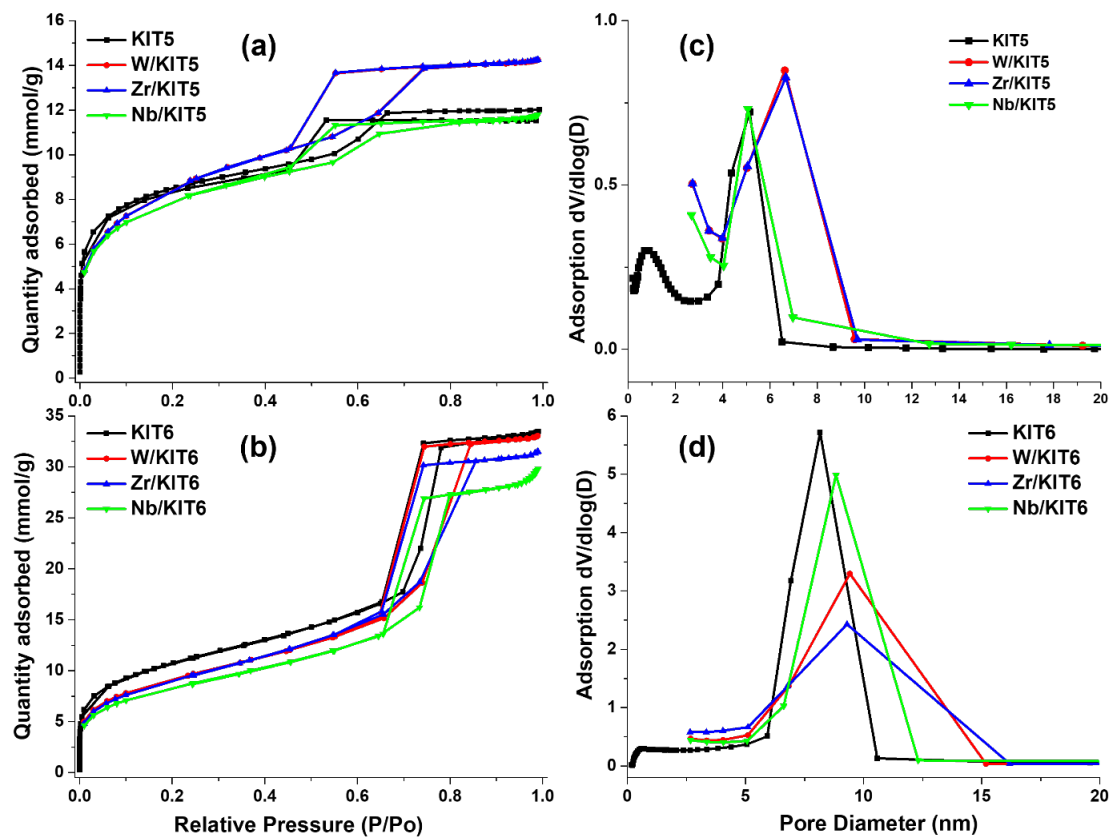


Figure 2.1 Isotherm curves of KIT5 series silicas (a) and KIT6 series silicas (b); pore size distribution of KIT5 series (c) and KIT6 series (d) silicas.

Textural and acidic properties of the pure and metal (W, Zr, Nb)-containing silicas were summarized in Table 2.1. Metal dopants led to a decreased surface area while an

increased average pore diameter, which can be ascribed to the blocking of the micropores.

B. Subramaniam group [61, 64, 65] reported that higher amount of metal-dopant into mesoporous silica led to a decrease in the surface area and increase in the pore diameter. No acidity was detected on the pure KIT5 and KIT6 silicas, and the amount of acid sites induced by the metal dopants follows the order of  $Zr > W > Nb$  due to their distinctive acidic properties, which will be discussed in detail later.

Table 2.1 Textural and acidic properties of the as-prepared silicas

Support	SA (m <sup>2</sup> /g)	V <sub>pore</sub> (cm <sup>3</sup> /g)	D <sub>ave.</sub> (nm)	acidity (mmol/gNH <sub>3</sub> )
<b>KIT5</b>	672	0.4	2.4	0.05
<b>W-KIT5</b>	662	0.5	3.0	0.31 <sup>[58]*</sup>
<b>Zr-KIT5</b>	661	0.5	3.0	0.63
<b>Nb-KIT5</b>	635	0.4	2.6	0.25
<b>KIT6</b>	858	1.2	5.4	0.04
<b>W-KIT6</b>	713	1.1	6.4	0.48 <sup>[64]*</sup>
<b>Zr-KIT6</b>	697	1.1	6.2	0.67
<b>Nb-KIT6</b>	649	1.0	6.3	0.21

\*: from literature

Thermal and chemical stability of heterogenous catalysts is a crucial issue especially in the upgrading of water-containing reaction system [77, 78]. To probe the stability of pure and W, Zr, Nb containing KIT5 or KIT6 silicas in HDO reaction condition, hydrothermal stability tests were executed in the condition as described in the Experimental Section. Metal (W, Zr, Nb) leaching results from the aqueous samples, alternation surface area and XRD patterns over the recovered powder was depicted in Fig. 2.2. What noteworthy is significant amount of tungsten loss (66.7wt%) was detected on W-doped KIT5 silica in H<sub>2</sub> atmosphere, while the leaching of Zr, Nb (Fig. 2a) as well as silicon (not

shown here) is negligible. It is reported that, with the molar ratio of Si/M=20, all of the Nb and most of Zr was incorporated as ions into the framework of silicas [59, 61, 65], but tungsten might exist as extra-framework species ( $\text{WO}_4$ ) in the mesoporous walls [58, 64]. Besides, B. Subramaniam's group deduced the interaction between niobium species and KIT6 is stronger from its much lower  $\text{H}_2$  consumption signal in  $\text{H}_2$ -TPR than W-doped KIT6 sample [58, 61]. In brief, in our study, the doped tungsten species might be shed via the cleavage of W-O-Si bonds by the dissolved  $\text{H}_2$  molecules in water.

Pure and metal (W, Zr, Nb)-doped silicas preserved their textural structure during the stability test in  $\text{H}_2$  atmosphere, as identical surface area (Fig. 2.2b) and pore size distribution (Fig. A1) was observed. Whereas, under 12.5 bar  $\text{N}_2$ , the slight abatement in the surface area of KIT5 series silicas and the increase in the bulky pore size over Zr-containing KIT5 might be ascribed to silica degradation caused by the hydrolysis of Si-O-Si and Si-O-M in the hydrothermal test condition. R. M. Ravenelle et al [79] proposed the hydrolysis of siloxane bonds (Si-O-Si) as the dominant degradation mechanism under steaming conditions. I. A. Bakare and the colleagues [80] ascribed the surface area reduction to the removal of Si and Al from zeolite framework in the hydrothermal stability test. Based on the aforementioned results, 12.5 bar of pure  $\text{H}_2$ , rather than  $\text{H}_2$ - $\text{N}_2$  mixture, was used in the HDO reaction.

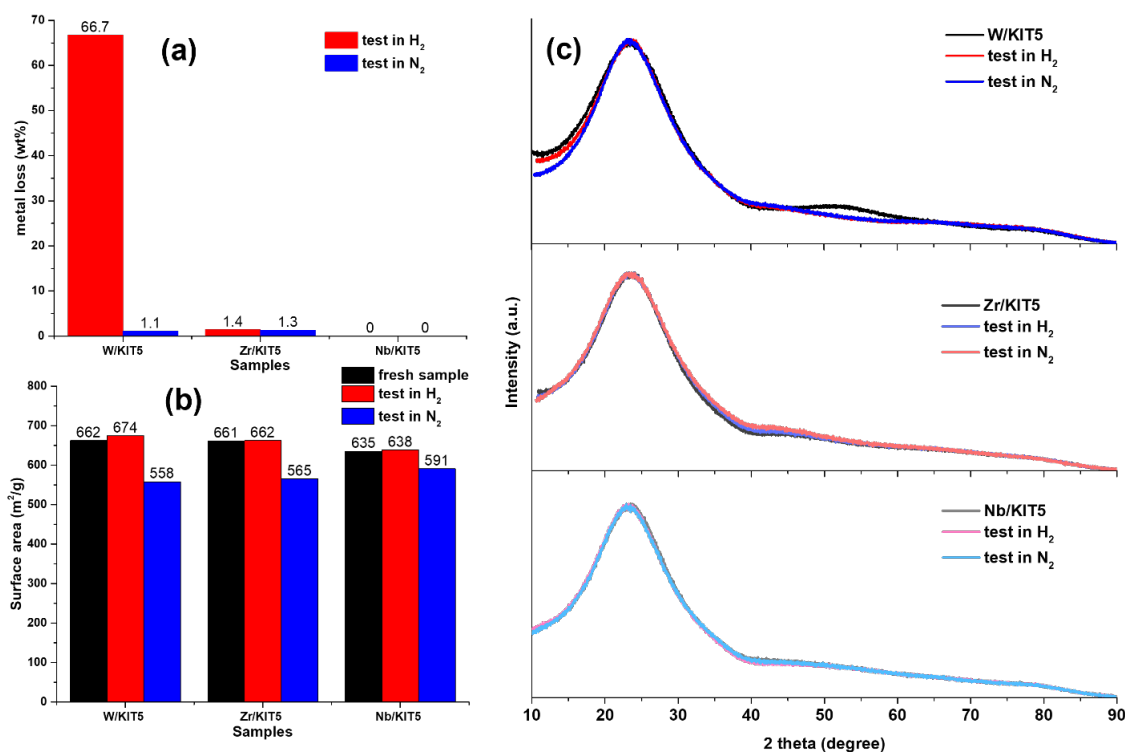


Figure 2.2 Metal (W, Zr, Nb) leaching (a), surface area loss (b) and XRD patterns comparison (c) during the thermal stability test.

Characteristic diffraction peaks of silica were observed in XRD patterns of pure and metal (W, Zr, Nb) doped silicas, and silica crystallinity was retained in the hot liquid water determined from the high similarity in the XRD plots before and after the test. Besides, neither metallic nor metal oxide phase of metal dopants was detected, which can be attributed to their high dispersion in silica framework. Disappearance of the broad peak on W containing KIT5 silica might result from tungsten leaching from silica framework. In conclusion, Zr, Nb-doped silicas can be utilized as the supports in the biomass conversion due to their remarkable stability during the reaction condition.

To figure out the optimal pH at which the maximum adsorption of Pd precursor occurs, uptake survey of PdTACl on the pure and metal-doped silicas were investigated as

illustrated in Fig. 2.3. Point of zero charge (PZC) of support, maximum palladium adsorption at the optimal pH was listed in Table 2.2. As expected, volcanic plots of cationic palladium uptake were observed on all the prepared silicas. Adsorption of palladium increased when the pH moved further away from the PZC due to increased amount of hydroxyl groups being deprotonated, while the high ionic strength at high pH lowered palladium uptake. Furthermore, a broader uptake survey plot with slightly increased maximum palladium adsorption appeared on metal containing silicas, which might be ascribed to the intensified hydroxyl groups originating from the metal dopants. It is more significant on Nb-doped silicas, due to the very high surface hydroxyl groups (12 OH/nm<sup>2</sup>) [81]. Even though our previous work showed ion-doped, PZC-altered silica and alumina cannot influence the adsorptive property of the metal precursor [82, 83], in this study, the metal dopants introduced a slight increase in the maximum palladium adsorption because the doped metals can be hardly removed from silica surface due to the strong interaction. Besides, the reduction in the PZC of metal-containing silicas might be assigned to the acidic properties of W, Zr and Nb dopants, which will be discussed in detail in the coming section.

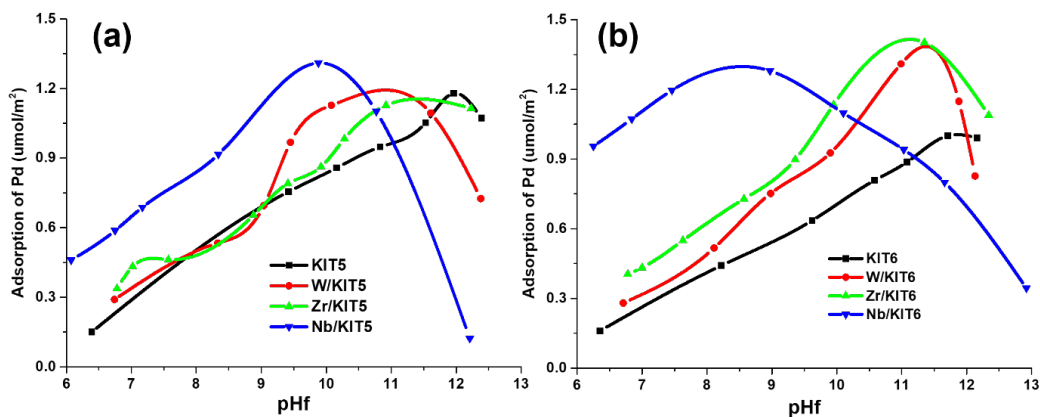


Figure 2.3 Adsorption survey of PdTACl on metal-doped KIT5 (a) and metal-doped KIT6 (b).

Table 2.2 Maximum adsorption of PdTACl on metal doped KIT5 and KIT6.

Property	KIT5	W/KIT5	Zr/KIT5	Nb/KIT5	KIT6	W/KIT6	Zr/KIT6	Nb/KIT6
PZC	3.4	1.2	2.4	2.1	3.6	1.3	2.4	2.2
pH <sub>opt.</sub>	12.0	10.1	10.9	9.9	11.7	11.0	11.4	9.0
$\Gamma_{\max.}(\mu\text{mol}/\text{m}^2)$	1.18	1.13	1.13	1.31	1.00	1.31	1.40	1.28

#### 2.4.2 Catalysts Characterization

Powder XRD patterns of the bifunctional catalysts as well as the supports were shown in Fig. 2.4. It is interesting to note that SEA prepared bifunctional catalysts displayed broad [111] peaks around  $33.8^\circ 2\theta$  of PdO and  $36.33^\circ 2\theta$  of Pd<sub>2</sub>O, while sharp peaks of metallic Pd with [111] peak centered at  $40.1^\circ 2\theta$  were observed on DI samples, suggesting SEA technique produced much smaller Pd particles [71]. The presence of palladium oxidation on SEA samples under ambient conditions is attributed to the higher metal dispersion [84]. Deconvolution of background subtracted XRD patterns on the bifunctional catalysts were displayed in Fig. 2.5-2.6. Particle size acquired from XRD analysis and H<sub>2</sub>-chemisorption as well as the metal dispersion were listed in Table 2.3.

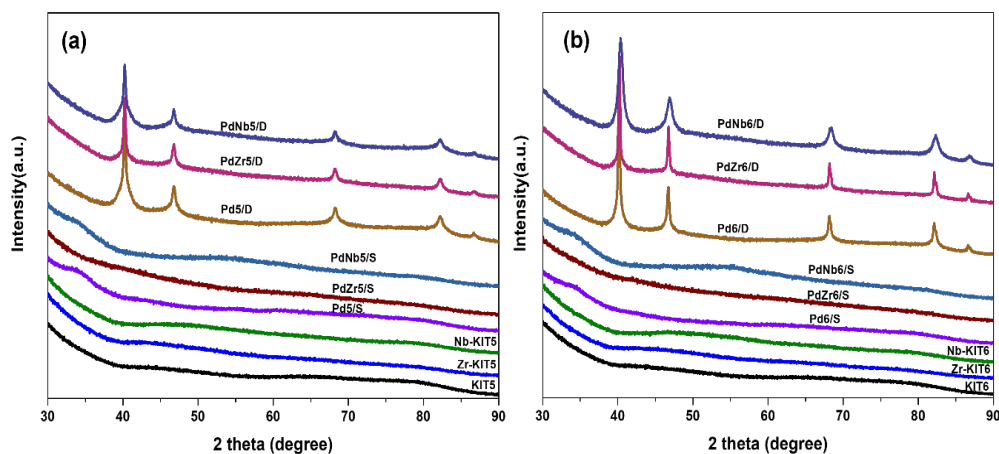


Figure 2.4 Normalized XRD patterns for silica supports and bifunctional catalysts: (a) KIT5 series, (b) KIT6 series.

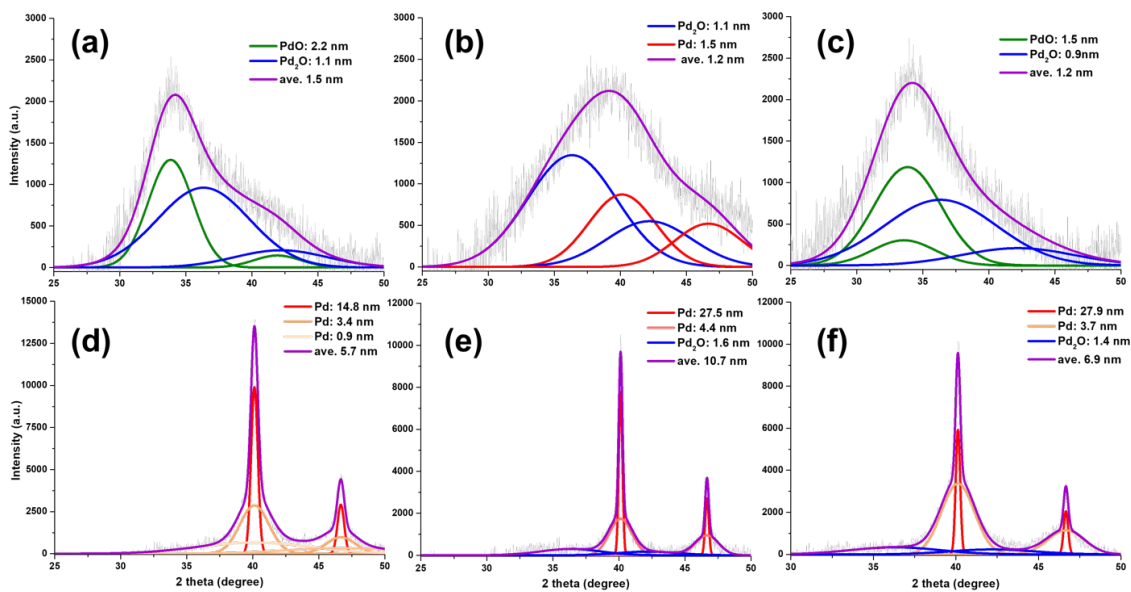


Figure 2.5 Deconvoluted XRD patterns for Pd5/S (a), PdZr5/S (b), PdNb5/S (c), Pd5/D (d), PdZr5/D (e), PdNb5/D (f).

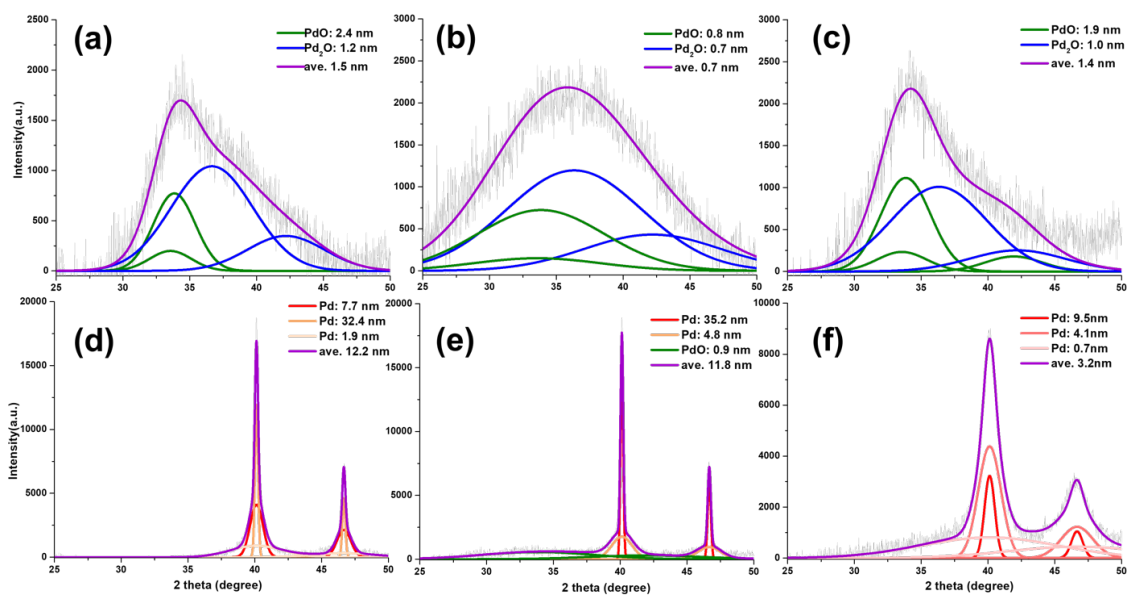


Figure 2.6 Deconvoluted XRD patterns for Pd6/S (a), PdZr6/S (b), PdNb6/S (c), Pd6/D (d), PdZr6/D (e), PdNb6/D (f).



Table 2.3 Summary of particle size pre- and post-HDO reaction and Pd leaching.

samples	Dispersion (%)	particle size (nm)		Particle size (nm)-post-HDO	leached Pd (%)
	by chemisorption	by XRD			by ICP
<b>Pd5/S</b>	91.4	1.9	PdO(2.2), Pd <sub>2</sub> O(1.1), ave.(1.5), sum(3.3)	Pd <sub>1</sub> (4.8), Pd <sub>2</sub> (2.2), ave. (2.9)	0.13
<b>PdZr5/S</b>	89.9	2.1	Pd <sub>2</sub> O (1.1), Pd (1.5), ave.(1.2), sum(2.7)	Pd <sub>1</sub> (2.2), Pd <sub>2</sub> (0.8), ave. (1.4)	0.13
<b>PdNb5/S</b>	74.2	2.2	PdO (1.5), Pd <sub>2</sub> O (0.8), ave. (1.1), (2.3)	Pd <sub>1</sub> (4.0), Pd <sub>2</sub> (1.4), ave. (2.4)	0.14
<b>Pd5/D</b>	30.2	3.7	Pd <sub>1</sub> (14.8), Pd <sub>2</sub> (3.4), Pd <sub>3</sub> (0.9), ave.(5.7)	Pd <sub>1</sub> (8.1), Pd <sub>2</sub> (2.1), ave. (4.3)	0.14
<b>PdZr5/D</b>	7.9	14.3	Pd <sub>1</sub> (27.5), Pd <sub>2</sub> (4.4), Pd <sub>2</sub> O (1.6), ave.(10.7)	Pd <sub>1</sub> (11.0), Pd <sub>2</sub> (2.6), ave. (4.5)	0.15
<b>PdNb5/D</b>	4.6	24.5	Pd <sub>1</sub> (27.9), Pd <sub>2</sub> (3.7), Pd <sub>2</sub> O (1.4), ave.(6.9)	Pd <sub>1</sub> (5.4), Pd <sub>2</sub> (1.8), ave. (3.2)	0.14
<b>Pd6/S</b>	55.7	3.8	PdO(2.4), Pd <sub>2</sub> O(1.2), ave.(1.5), sum (3.6)	Pd <sub>1</sub> (2.3), Pd <sub>2</sub> (0.9), ave. (1.3)	0.13
<b>PdZr6/S</b>	65.2	2.8	PdO(0.8), Pd <sub>2</sub> O(0.7), ave.(0.7), sum (1.5)	Pd <sub>1</sub> (2.0), Pd <sub>2</sub> (0.9), ave. (1.4)	0.13
<b>PdNb6/S</b>	60.7	2.9	PdO(1.9), Pd <sub>2</sub> O(1.0), ave.(1.4), sum(2.9)	Pd <sub>1</sub> (2.2), Pd <sub>2</sub> (0.7), ave. (1.2)	0.13
<b>Pd6/D</b>	8.2	13.7	Pd <sub>1</sub> (32.4), Pd <sub>2</sub> (7.7), Pd <sub>3</sub> (1.9), ave.(12.2)	Pd <sub>1</sub> (13.5), Pd <sub>2</sub> (2.8), ave. (7.6)	0.14
<b>PdZr6/D</b>	6.8	16.5	Pd <sub>1</sub> (35.2), Pd <sub>2</sub> (4.8), PdO (0.9), ave.(11.8)	Pd <sub>1</sub> (7.4), Pd <sub>2</sub> (1.5), ave. (3.2)	0.13
<b>PdNb6/D</b>	3.9	29.0	Pd <sub>1</sub> (9.5), Pd <sub>2</sub> (4.1), PdO (0.7), ave.(3.2)	Pd <sub>1</sub> (14.9), Pd <sub>2</sub> (4.0), Pd <sub>3</sub> (1.5), ave. (1.4)	0.14

XRD and H<sub>2</sub>-chemisorption revealed, to some extent, consistent Pd particle size over all the SEA designed catalysts. Chemisorption estimate particle size was situated in the range of average and sum of particle size from XRD analyzed several different metal (oxide) phases. This phenomenon can be explained by the partial coverage of the Pd oxide over the inner metallic Pd particles. However, a conspicuous discrepancy in the particle size over DI was conveyed by XRD and chemisorption, with larger particles being derived by chemisorption. Our previous investigation [85, 86] discovered the discrepancy in metal particle size estimated by chemisorption and XRD is due to decoration of carbon support onto metal surface. And strong Pd-C interaction can enhance this discrepancy because of the promoted formation of the carbon shell coated on palladium nanoparticle. Whereas, in this study, palladium-support interaction over SEA catalysts is stronger than DI prepared

ones [26], but this discrepancy is prevalent among DI samples. Besides, most Zr and all the Nb was homogeneously incorporated into the framework of silica as ions and the interaction between Zr or Nb and silica was very strong [61, 65], indicating the mobility of Zr and Nb is minimal. The above two factors suggest this discrepancy caused by decoration of metal-dopants or silica onto Pd particle surface can be excluded. However, it is prone to speculate it to the multigrain of several smaller Pd NPs over DI samples. A.N. Gavrilov et al [87] detected discrepancy in particle size characterized by XRD and chemisorption over PtRu catalysts with high metal contents (30-60 wt%) and interpreted it by the multi-grained structures, exhibiting distinguishingly in HRTEM images. Meanwhile, the size of single crystalline domains is in good agreement with the one derived by XRD and the physical dimension of the multi-grained particles is in accordance with the results of chemisorption. Therefore, this discrepancy in particle size of our DI catalysts might also result from the multi-grained palladium particles.

To gain insight into the acidity of the as-synthesized supports and catalysts, temperature programmed desorption of ammonia (NH<sub>3</sub>-TPD) was employed to analyze the strength and number of the acid sites, which can be identified by ammonia desorption temperature and resolved peak area, respectively (Fig. 2.7). Three ammonia desorption peaks were resolved for all Zr- or Nb-containing samples by Gaussian peak fitting. The low temperature desorption peak around 200 °C is ascribed to Lewis acid sites; the peak centered in 260 °C -310 °C is due to acid sites with medium strength; another desorption peak above 400 °C is assigned to strong acid sites arising from Bronsted acid sites [61, 65]. The quantified amounts and percentage of acid sites at specific desorption temperatures were summarized in Table A1.

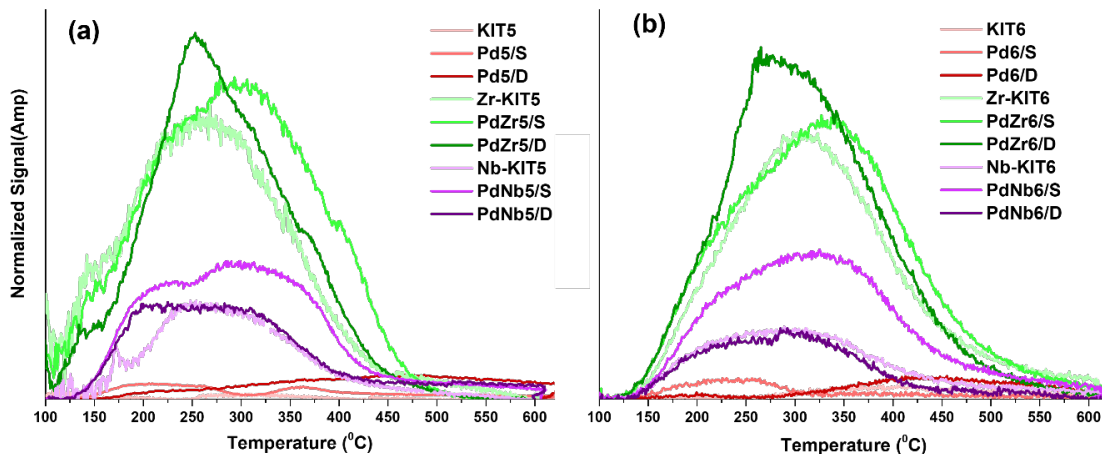


Figure 2.7 NH<sub>3</sub>-TPD spectra of bifunctional catalysts and the supports: (a) on metal-doped KIT5, (b) on metal-doped KIT6.

It is interesting to observe that most of the surface acid sites are detected in the medium acid strength region (> 60%). Acidity of palladium catalysts supported on pure KIT5 or KIT6 silicas is negligible (< 0.05 mmol NH<sub>3</sub>/g). But Zr or Nb-dopant substantially imparts acidity and Zr introduced higher amount of acid sites. Moreover, palladium deposition, especially with smaller Pd nanoparticles, led to a slightly higher amount of acid sites. This phenomenon might be interpreted by the cleavage of Zr, or Nb bond with -O-Si due to palladium loading, resulting into increased amount of surface hydroxyl groups. Furthermore, the enhanced acidity on catalysts synthesized by SEA recipe might be due to the stronger palladium-support interaction. A reduction in the fraction of Bronsted acid sites was also observed with palladium deposition, which might result from the generation of Pd(O<sub>x</sub>) cationic species. H. Hosseiniamoli et al [88] noticed that Lewis acid sites around 380°C was enhanced at the sacrifice of Bronsted acid sites due to the exchange of protons by Pd(O<sub>x</sub>) cations. Palladium deposition led to a prominent reduction in the fraction of strong acid sites on Zr-containing silicas.

### 2.4.3 Catalysts Evaluation

Aromatic compounds with hydroxyl and methoxy groups have been extensively utilized as a model feedstock for biomass conversion by an HDO mechanism [47]. In this study, tri-functional phenolics of 2-methyl guaiacol (M-GUA) with hydroxyl and methoxy groups on the aromatic ring was utilized as the model molecule under mild conditions (112 °C and 12.5 bar H<sub>2</sub>). It is reported that product distribution in the HDO reaction is very similar to guaiacol except for a 4-methyl substitution [89], so the activity and selectivity in our HDO reaction of M-GUA was discussed with the comparison to HDO of guaiacol from the literature.

Investigation of the as-prepared bifunctional catalysts in the HDO of M-GUA presented as a function of given time interval is displayed in Fig. 2.8 and Fig. 2.9. Remarkably, the HDO of M-GUA in this study consists of several sequential and parallel reactions including hydrogenation and deoxygenation. Six main products were detected by GC-MS, such as 2-methoxyl-4-methylcyclohexanol, 2-methoxyl-4-methyl-cyclohexanone, 4-methylcyclohexanone, 4-methylcyclohexanol, 3-methyl-cyclohexanone and 3-methyl-cyclohexanol, while toluene, methylcyclohexane, 3-methylanisole, 1-methoxy-3-methylbenzene and cyclohexanol are the minor products. The activity of acidic (Zr or Nb containing) and neutral KIT5 or KIT6 silicas is negligible, clarifying the as-prepared supports are not active in HDO reactions regardless of the acidity. Noticeably, majority of the products were completely hydrogenated over the aromatic ring. Y.-K. Hong et al [90] reported stepwise hydrogenation-deoxygenation mechanism in HDO of guaiacol and the complete deoxygenation was closely related to the reaction temperature. C. R. Lee and the colleagues proposed the deoxygenation over 2-methoxycyclohexanol occurred above

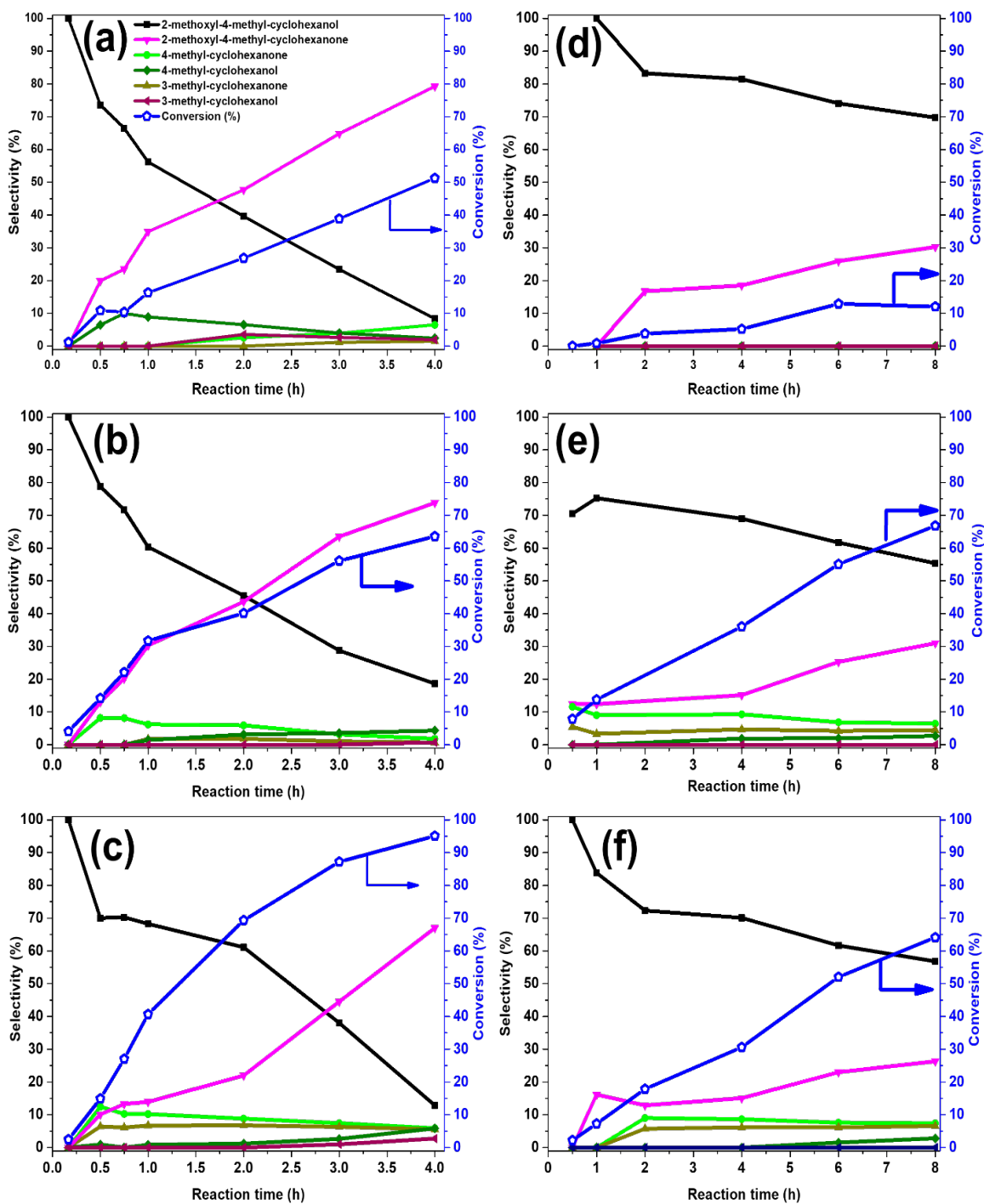


Figure 2.8 Conversion and selectivity of main products in the HDO reaction of M-GUA on (a) Pd5/S, (b) PdZr5/S, (c) PdNb5/S, (d) Pd5/D, (e) PdZr5/D, (f) PdNb5/D, SEA and DI were run for 4 hours and 8 hours, respectively.

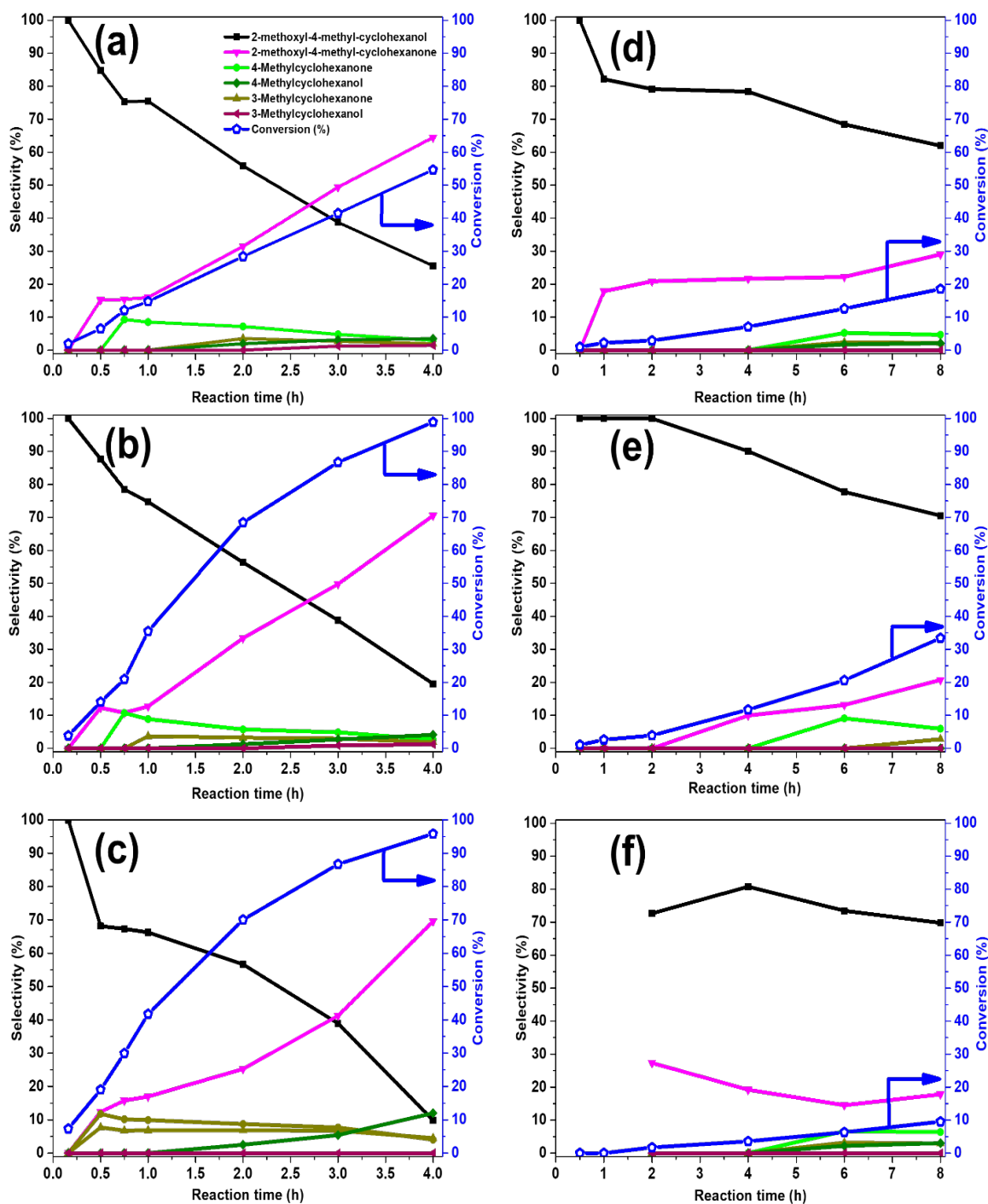


Figure 2.9 Conversion and selectivity of main products in the HDO reaction of M-GUA on (a) Pd6/S, (b) PdZr6/S, (c) PdNb6/S, (d) Pd6/D, (e) PdZr6/D, (f) PdNb6/D, SEA and DI were run for 4 hours and 8 hours, respectively.

250°C over acid-metal catalysts [53]. In addition, it is also reported that higher loading of Pd over zeolite significantly increased guaiacol conversion but the selectivity to aromatic products concurrently decreased and the lower amount of strong acid sites also enhanced non-aromatic selectivity [91]. Therefore, in our study, the complete hydrogenation of aromatic ring and the progressively partial deoxygenation would be on account of the relatively high Pd loading, low reaction temperature and weak acidity of the prepared metal-acid catalysts.

Catalysts synthesized by SEA method exhibited superior activity with a higher M-GUA converted rate (Fig. 2.10a). This activity can be attributed to the sufficient surface palladium sites because of the smaller particles [55, 92]. While the lower activity over DI prepared catalysts on KIT6 series supports was due to their larger palladium particles. Further increase in the activity was monitored over palladium catalysts with Zr or Nb dopants in view of the introduction of acid sites [47, 53, 93]. It is reported that the oxophilic cations devoted by Nb<sub>2</sub>O<sub>5</sub> or ZrO<sub>2</sub> at the Pd-support interface enhanced cleavage of C-O bond, promoting the deoxygenation reaction [93-95]. Higher activity was attained over KIT6 series catalysts, which might benefit from the larger mesopores [57, 60]. The highest M-GUA conversion and deoxygenated activity was achieved over SEA prepared Pd catalysts supported on Nb-containing KIT5 or KIT6 silicas. No correlation is observed between the selectivity of deoxygenated products and M-GUA conversion over SEA prepared catalysts (Fig. 2.10b), implying the deoxygenation is essentially independent of M-GUA concentration.

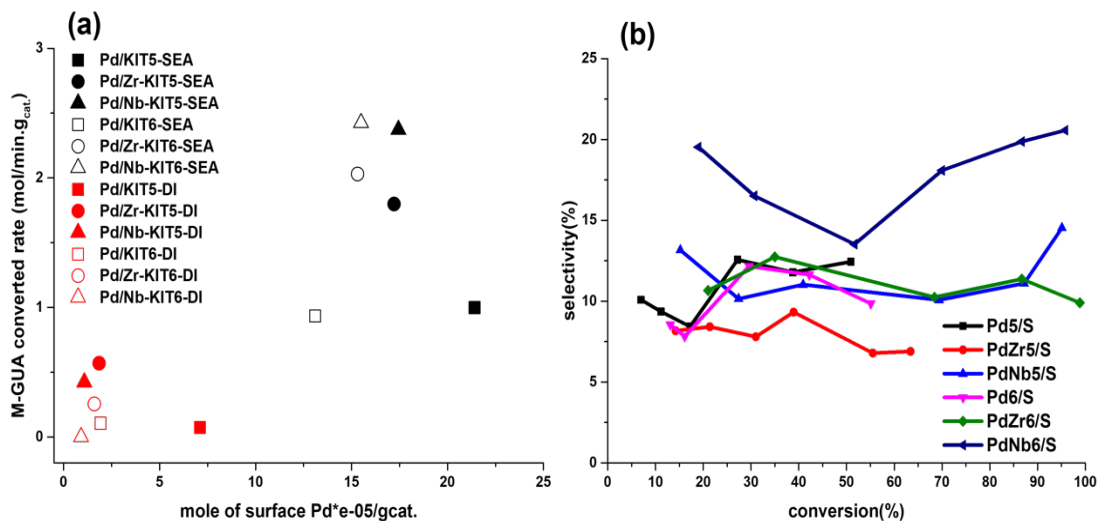


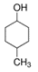
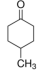
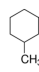
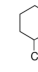
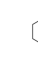

Figure 2.10 Converted rate (a) and selectivity to dehydrogenated products vs conversion (b) of M-GUA over the as-prepared bifunctional catalysts.

The preceding results on HDO activity imply that surface palladium sites and support acid are of great importance in the catalytic activity and product distribution. Aromatic ring in (methyl-) guaiacol was initially saturated via the hydrogenation process over palladium sites and the further deoxygenation reaction pathway occurred on the active (metal-) acid sites [90, 96]. The overall deoxygenated rate and product distribution is listed in Table 2.4. Remarkably, the deoxygenated activity raised with palladium dispersion due to the enhanced amounts of hydrogenated intermediates. In addition, it is exceedingly sensitive to catalysts acidity. The rate of deoxygenation from SEA-prepared catalysts follows the order: Pd/Nb-SiO<sub>2</sub> > Pd/Zr-SiO<sub>2</sub> > Pd-SiO<sub>2</sub>, while the amount of acid sites shows the trend of Pd/Zr-SiO<sub>2</sub> > Pd/Nb-SiO<sub>2</sub> > Pd-SiO<sub>2</sub>. This manifests SEA synthesized Pd catalysts with Nb dopants exhibits the optimal palladium-acid balance. W. Wang et al [97] reviewed that favorable metal-acid balance should be optimized in an appropriate range to ensure the hydro-isomerization occurs via the “ideal” consecutive mechanism and some conversion is not inhibited. X. Wu and the colleagues [98] argued that acid- metal



balance can govern HDO product distribution and a low acid/metal ratio facilitate anti-coking ability. In contrast, DI prepared bifunctional catalysts exhibits considerable low HDO activity regardless of metal/acid balance due to the insufficient surface palladium sites. Therefore, the highest or lowest metal/acid ratio might be unbeneficial to the catalytic activity, and the benign metal-acid balance should be optimized.

Table 2.4 Conversion, deoxygenated rate and products distribution in HDO reactions at 112 °C, 12.5 bar H<sub>2</sub> for 4 hrs.

catalysts	conversion	deoxygenated rate	molar fraction (%) of products in aqueous sample					
	%	mmol g <sup>-1</sup> min <sup>-1</sup>						
Pd5/S	51.2	0.124	3.3	1.2	0.8	1.0	4.3	40.6
PdZr5/S	63.6	0.136	1.1	2.8	0.44	0.5	11.8	46.9
PdNb5/S	95.1	0.506	5.6	5.6	5.3	2.6	12.3	63.7
Pd5/D	5.2	0.00	---	---	---	---	11.4	7.6
PdZr5/D	36.1	0.076	3.3	0.7	1.7	---	24.9	5.5
PdNb5/D	30.6	0.062	1.1	---	1.9	---	21.5	4.6
Pd6/S	54.6	0.093	1.6	1.9	1.1	0.8	14.0	32.3
PdZr6/S	98.8	0.198	2.6	4.1	1.9	1.2	19.3	69.7
PdNb6/S	95.8	0.494	3.9	11.5	4.3	0	9.5	66.6
Pd6/D	7.1	0.00	---	---	---	---	5.5	1.5
PdZr6/D	11.7	0.00	---	---	---	---	10.6	1.2
PdNb6/D	3.6	0.00	---	---	---	---	2.9	0.69

Proposed reaction pathways in the HDO of M-GUA in our study were depicted in Figure 2.11, involving four main reaction pathways: hydrogenation, demethoxylation, demethylation and dehydroxylation [44, 96]. Ring hydrogenation of methyl-guaiacol proceeds to yield 2-methoxyl- 4-methylcyclohexanol over surface palladium sites, which then reversibly converted to 2-methoxyl-4-methyl-cyclohexanone. Afterwards, two

competing reaction pathways took place via demethoxylation to obtain 4-methylcyclohexanol and by demethylation combined with dehydroxylation to produce 3-methyl-cyclohexanol over metal-acid sites. It is evident that the demethylation rate is higher than demethoxylation in our study. C.A. Teles and the colleagues [96] discovered that it is more facile to remove the hydroxyl group than the methoxy group on benzene ring due to a lower bond scission energy. Additionally, there is a small amount of methyl-guaiacol was converted to 3-methyl-cyclohexanol and/or 3-methyl-cyclohexanone through the initial dehydroxylation and then demethylation over the benzene ring with the subsequent hydrogenation of the benzene ring. The high extent of hydrogenation of methyl guaiacol was highly influenced by low reaction temperature, high Pd loading and low ratio of strong acid sites. While, another possible explanation is the methyl group on the benzene ring in M-GUA promotes its planar adsorption onto the catalysts. It is reported that the adsorption configuration of guaiacol is expected to govern the ring hydrogenation or C-O bond scission [91, 99, 100]. Adsorbed guaiacol in horizontal configuration bonds through the aromatic ring benefits the easy interaction of Pd with  $\pi$ -bonds and facilitates the ring hydrogenation. While the nonplanar fashion adsorption on the acid sites promotes the deoxygenated reaction with aromatic products.

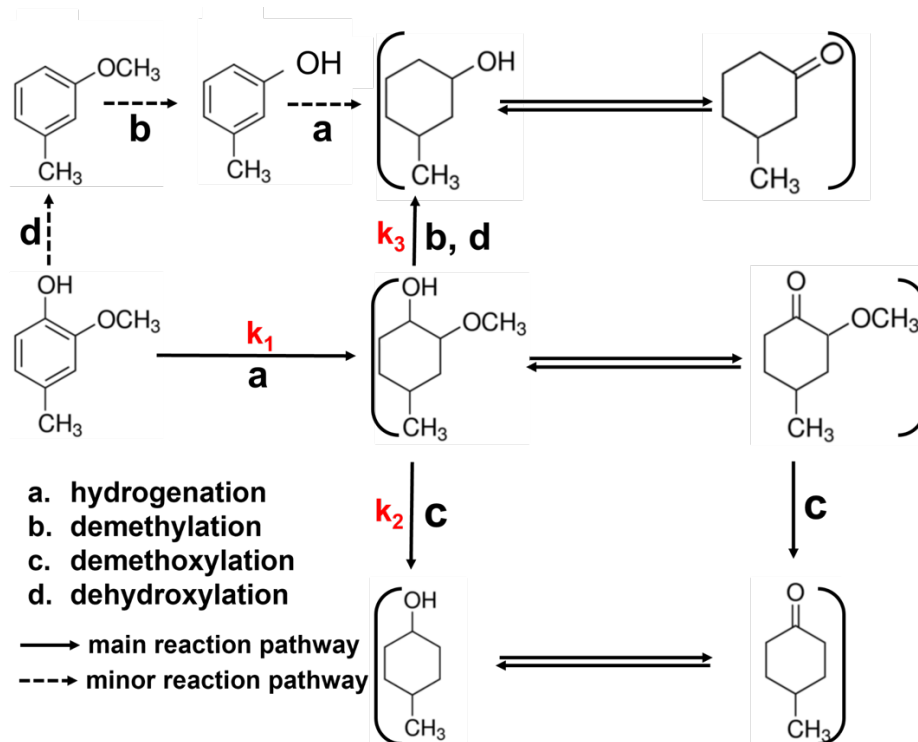


Figure 2.11 Reaction mechanism of HDO of M-GUA.

#### 2.4.4 Spent Catalysts Characterization

Structural and compositional changes of metal particles are generally considered as the main danger for the catalyst deactivation especially in aqueous media in aggressive reaction condition [47, 53]. To gain the insight into the possible alteration of palladium particle size and palladium leaching during the HDO of M-GUA, XRD characterization was conducted on recovered powder catalysts and ICP-OES analysis over the aqueous samples. Supports of pure and metal (Zr, Nb)-doped silicas preserved their crystallinity well in the HDO reaction, as shown in Fig. A2.

Fig. 2.12 plots the XRD patterns of the fresh and post reaction catalysts. divergent trends in palladium particle size were revealed between SEA and DI prepared catalysts. Peak fitting over background subtracted XRD patterns were shown in Fig. 2.13-2.14. Over SEA catalysts, the typical diffraction peaks of PdO at  $33.84^\circ$  and Pd<sub>2</sub>O at  $36.33^\circ$  of  $2\theta$

were transferred to metallic palladium due to the reduction in the H<sub>2</sub> atmosphere. Careful comparison of XRD-derived particle size of each deconvoluted species before and after the reaction (Table 2.3) demonstrated that average particle size of post-reaction catalysts is between the average and sum of particle size of different species over fresh SEA catalysts. This deduced that particle size change after reactions might be due to architecture of decoration of Pd oxide species onto the underlying Pd particle and no sintering occurred during the reaction over SEA catalysts. In addition, the appearance of broad metallic Pd peaks on the post reaction catalysts might be ascribed to palladium phase transition rather than sintering. While literature reported the grievous aggregation of metal NPs over their Au/C and Pd/C by increasing from 6nm to 28.5 nm and 3.9 nm to 13.6 nm in HDO reaction, respectively [92]. The high stability in the particle structure over our SEA catalysts might be due to the strong metal-support interaction and the mild reaction condition.

In contrast, bifunctional catalysts synthesized by DI method presented broader diffraction peaks of metallic palladium after the HDO reaction, suggesting the decreased particle size, which can be attributed to the particle reconstruction during the reaction. While the overall larger Pd particles were identified over DI samples than SEA samples during the reaction. Tiny amount (~0.14%) of palladium leaching was detected by ICP analysis from both SEA and DI synthesized catalysts. A. Wang et al [101] reported that mesoporous channel in the support can effectively prevent palladium leaching and particle sintering.

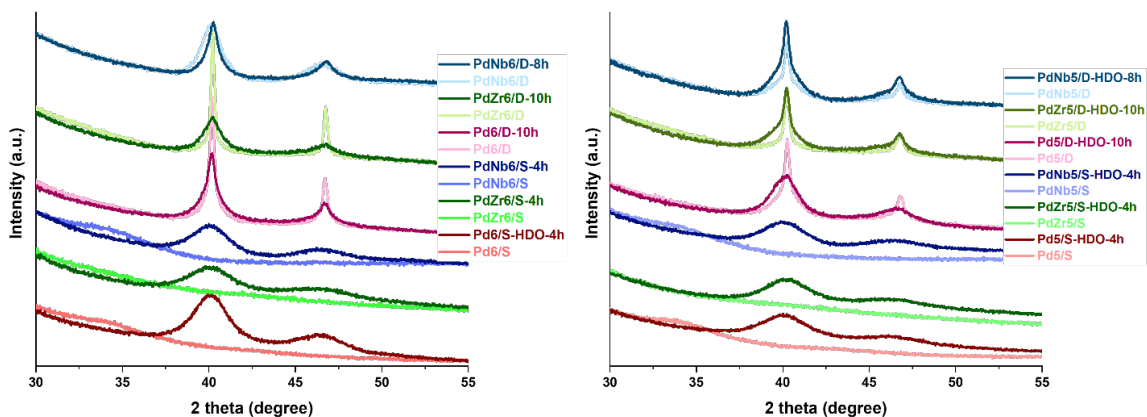


Figure 2.12 Normalized XRD patterns comparison before and after HDO reactions over bifunctional catalysts supported on metal-doped KIT5 (a) and metal-doped KIT6 (b).

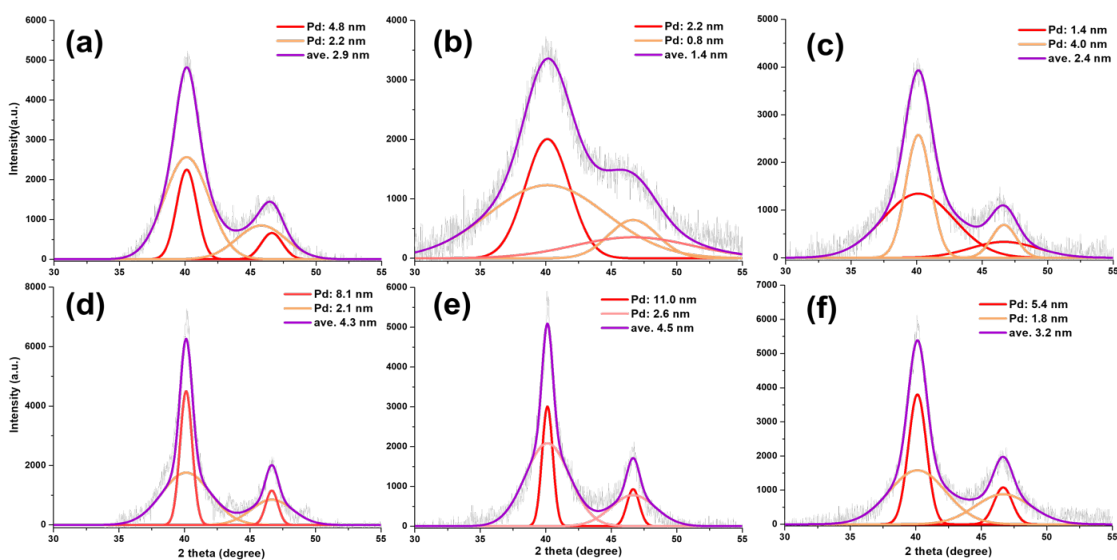


Figure 2.13 Deconvoluted XRD patterns of bifunctional catalysts after HDO reactions: (a) Pd5/S-HDO-4h, (b) PdZr5/S-HDO-4h, (c) PdNb5/S-HDO-4h, (d) Pd5/D-HDO-10h, (e) PdZr5/D-HDO-10h, (f) PdNb5/D-HDO-8h.

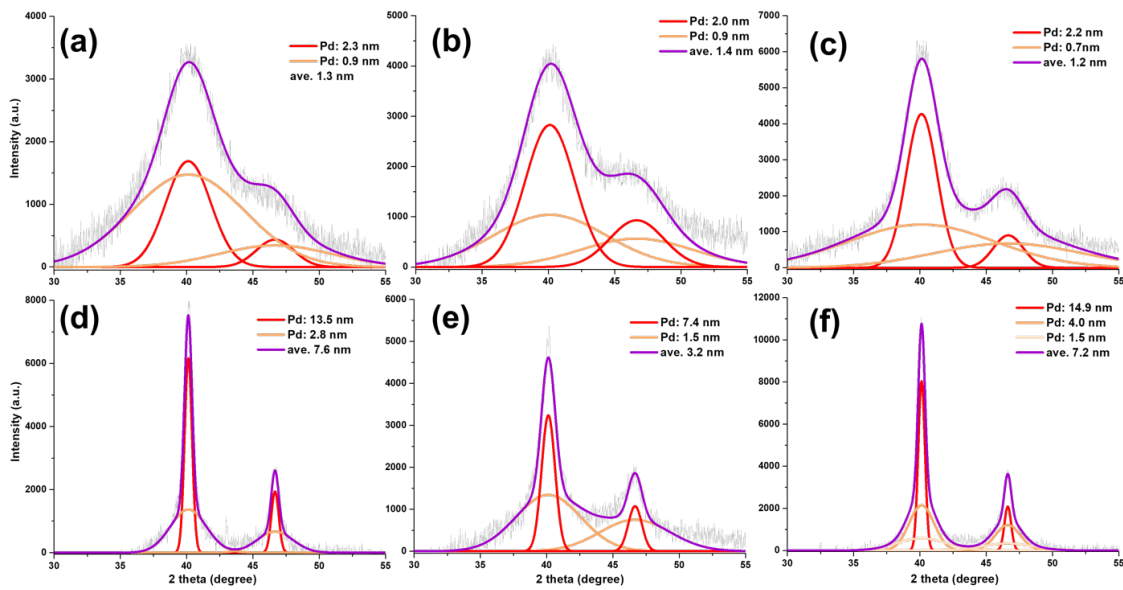


Figure 2.14 Deconvoluted XRD patterns over bifunctional catalysts after HDO reactions: (a) Pd6/S-HDO-4h, (b) PdZr6/S-HDO-4h, (c) PdNb6/S-HDO-4h, (d) Pd6/D-HDO-10h, (e) PdZr6/D-HDO-10h, (f) PdNb6/D-HDO-8h.

## 2.5 Conclusion

Hierarchically mesoporous silica with tuned amount of acid sites were favorably synthesized by using hydrothermal synthesis method. Bifunctional catalysts with varied metal-acid balances were obtained by using SEA and IWI techniques. Furthermore, SEA is a promising approach to produce ultra-small palladium particles. It was found that, under the mild reaction condition of 112 °C and 12.5 bar H<sub>2</sub>, the acid sites significantly improved the catalytic activity in the HDO reaction of M-GUA due to the role in C-O scission. Niobium containing Pd catalysts by SEA method exhibited the highest reactivity and HDO rate due to the optimal metal/acid sites ratio. No significant deactivation of the catalysts was detected in our HDO reaction condition with possible three explanations: 1) mild reaction condition at 112 °C, under 12.5 bar H<sub>2</sub>; 2) negligible palladium leaching and slight particle sintering; 3) hierarchical mesopores.

## CHAPTER 3

# A GENERALIZABLE AND FACILE SYNTHESIS OF GEOMETRICALLY CONTROLLED AND HIGHLY DISPERSED PDAU NANOPARTICLES ON $\text{SiO}_2$ AND $\text{Al}_2\text{O}_3$

### 3.1 Abstract

A series of bimetallic PdAu (Pd:Au=3:1, 1:1, 1:3) nanoparticle catalysts on oxide supports with high metal dispersion and homogenous alloys were successfully synthesized through simultaneous strong electrostatic adsorption on high surface area silica and alumina. Comparison of the adsorption behaviors of Pd and Au precursor complexes,  $[\text{Pd}(\text{NH}_3)_4]^{2+}$  and  $[\text{Au}(\text{en})_2]^{3+}$  respectively, over silica and alumina suggests fully deprotonated silica surface can adsorb more cationic Pd and Au metal complexes than alumina, which was partially charged at high pH. TPR experiments revealed a stronger metal-support interaction induced by co-SEA method than impregnation. Powder XRD and electron microscopy imaging characterization confirmed the formation of ultra-small particles with homogenous alloys. Pd oxide species were detected over PdAu nanoparticles and the content can be tuned by adjusting the composition. IR spectroscopy and pulse chemisorption with CO as the probe molecule verifies the higher number of Pd atoms exposed on the surface of the nanoparticles than impregnation prepared larger particles.

### 3.2 Introduction

Rational design of bimetallic materials has emerged as a hot spot in catalysis in the past several decades due to their unique functions beneficial to boost the catalytic performance, including improved activity, selectivity, and stability, which are not found over the monometallic variants [102-104]. Traditionally, monometallic catalysts were impeded in their application as the controllable properties were limited exclusively to metal dispersion and metal-support interaction. Introducing a second metal aroused a revolution in catalysis leading to the formation of specific structures, like homogenous alloys, single atom alloys, core-shell architecture, or the possibility of new active bifunctional sites, with governed electronic, ensemble, and ligand effects [105-109]. J-S.M. Lee et. al. [110] found that homogenous FeCu alloys showed excellent ORR activity, high stability, and well-defined poisoning resistance compared to the monometallic counterparts. J.E.S Hoeven and co-workers [111] pioneered the shell-thickness-dependent catalytic activity of  $\text{Au}_{\text{core}}/\text{Pd}_{\text{shell}}$  material in selective hydrogenation of butadiene, reporting a 50-fold better performance over individual components or their alloys. It is also reported that atomically diluted Pt on Cu nanoclusters offer efficient C-H activity and strong coke-resistance [112].

Pd is a marvelous catalyst in a variety of reaction systems, such as hydrogenation [113], dehydrogenation [114], oxidation [115], ORR [116], cross-coupling [66], etc. Research in the last few decades acknowledged that Au, which had been considered as an inactive catalytic material, has shown promising potentials in numerous reactions by subtly controlling the atom dispersion and interaction with the support [117-119]. Bimetallic PdAu alloys have been reported to exhibit specific catalytic performance in heterogenous molecular formations whereas single Pd or Au materials were ineffective, which can



account for the electronic and geometric effects due to Pd and Au adjacent on the alloy surface [120, 121]. Jiang et al [122] revealed that the activity of PdAu nanoparticles (NPs) is 2.26 times higher than that of Pd/SiO<sub>2</sub>, which is also greatly influenced by the composition and particle size. It is reported that H<sub>2</sub> desorption behavior and O<sub>2</sub> activation can be governed by controlling Pd ensembles through altering alloyed PdAu compositions [123]. Dimitratos et. al. [124] observed enhanced activity in alcohol oxidation over Pd-Au bimetallic NPs while Pt-Au NPs are less active compared to their single Pd or Pt variant, and they speculated that superior properties of Pd-Au were assigned to the positive geometric and electronic effects; while it is negative for Pt-Au.

Open questions also exist in the synthesis strategies in making bimetallic PdAu NPs. Ultra-small Au NPs on SiO<sub>2</sub> were hard to obtain via the most frequently used methods, such as impregnation, ion exchange, and deposition-precipitation, because of the high acidity of gold precursor and a lower melting point of Au [125, 126]. Whilst, gold bis-ethylenediamine ([Au(en)<sub>2</sub>]<sup>3+</sup> or AuBen) is an efficient metal precursor to synthesize small Au NPs on normal supports (carbon, SiO<sub>2</sub>, Al<sub>2</sub>O<sub>3</sub>, ZrO<sub>2</sub>, TiO<sub>2</sub>, Nb<sub>2</sub>O<sub>5</sub>, etc.) by inducing a strong interaction between cationic gold precursor and the oppositely charged support surface [127]. In earlier works [27, 28, 128, 129], ultra-small mono/bimetallic Pd, Pt, Ni, Co, Cu NPs over silica were successfully fabricated through strong electrostatic adsorption method.

In this study, three atomic ratios (3:1, 1:1 and 1:3) of bimetallic PdAu nanomaterials over high surface area of aerosol 300 and  $\gamma$ -alumina, were synthesized through simultaneous strong electrostatic adsorption (co-SEA) protocol. For the sake of comparison, larger PdAu NPs were also obtained via simultaneous incipient impregnation

(co-DI) by using the same supports, metal precursors and same compositions. High sensitivity powder X-ray diffraction and electron microscopy imaging were carried out to investigate the morphology, particle size, as well as the homogeneity of the alloys. Reducibility property and metal-support interaction was identified by H<sub>2</sub>-TPR. XPS was used to check the electronic structure in the alloys. Combination of IR spectroscopy and chemisorption was performed to verify the geometry and dispersion of Pd on the surface of alloyed NPs.

## 3.2 EXPERIMENTAL SECTION

### 3.2.1 Materials

High surface area (~280 m<sup>2</sup>/g) silica (Aerosil 300 or A300, Evonik) and gamma alumina ( $\gamma$ -Al<sub>2</sub>O<sub>3</sub>, UOP) were used as support materials for catalyst synthesis. A300 was used directly as received while  $\gamma$ -Al<sub>2</sub>O<sub>3</sub> was calcined in air at 500 °C for 4 hours. Physical properties of A300 and  $\gamma$ -Al<sub>2</sub>O<sub>3</sub>, including point of zero charge (PZC), BET surface area (SA), and water accessible pore volume, are listed in Table 3.1. The PZC of A300 (3.6) is much lower than  $\gamma$ -Al<sub>2</sub>O<sub>3</sub> (8.3). In the preparation of all the catalysts, gold bis-ethylenediamine (AuBen) and tetramminepalladium (II) nitrate ([Pd(NH<sub>3</sub>)<sub>4</sub>](NO<sub>3</sub>)<sub>2</sub>, or PdTA-NO<sub>3</sub>, Sigma-Aldrich, 99.99%) were used as cationic metal precursors. AuBen was prepared according to prior literature [127, 130] by using chloroauric acid (HAuCl<sub>4</sub>·xH<sub>2</sub>O, Alfa Aesar, >99.9%), ethyl ether (Sigma Aldrich, >98%), ethylenediamine (Sigma Aldrich, >99), and anhydrous ethanol (BeanTown Chemical, >96%). Sodium hydride and hydrochloric acid were used to adjust solution pH in the SEA synthesis process. Analytical gases, 1% CO/Ar (99.999%), UHP N<sub>2</sub> (99.999%) and UHP argon (99.999%), were acquired from Airgas company.

Table 3.1 Support property and uptake of Pd-Au pair summary.

Support	A300	$\gamma$ -Al <sub>2</sub> O <sub>3</sub>
SA (m <sup>2</sup> /g)	280	277
PZC	3.6	8.3
V <sub>pore</sub> (cm <sup>3</sup> /g)*	2.7	2.0
pH <sub>optimal</sub>	10.8	11.5
max. $\Gamma_{Au}$ (mmol/m <sup>2</sup> )	0.61	0.39
max. $\Gamma_{Pd}$ (mmol/m <sup>2</sup> )	1.03	0.37

\*water accessible pore volume

### 3.2.2 Uptake Survey

In the uptake survey experiments, freshly prepared precursor solutions with 200 ppm Au or Pd (as AuBen or PdTA-NO<sub>3</sub> respectively) in DI water were used for monometallic adsorption. Bimetallic adsorption used a solution of 100 ppm each of Au and Pd (total concentration of 200 ppm). Uptakes were investigated at high pH ranges, adjusted by NaOH or HCl. The surface loading (SL) was fixed at 1000 m<sup>2</sup>/L, such that the support amount is determined from the solution volume (set at 15mL), according to equation 3.1. Prior to adding the support material, an excess aliquot (5mL) of the solution was taken to measure the initial concentrations of Pd and Au, and the initial pH was also recorded. After addition of the support, the slurry was shaken at 120 rpm for 1 hour. Equilibrium (final) pH was measured and the filtered solutions were obtained to determine final Pd and Au amounts. Surface adsorbed-metal density ( $\Gamma$ ,  $\mu\text{mol}/\text{m}^2$ ) was calculated by equation 3.2.

$$m(g) = \frac{\left( \text{solution volume (L)} * SL \left( \frac{\text{m}^2}{\text{L}} \right) \right)}{S \left( \frac{\text{m}^2}{\text{g}} \right)} \quad \text{Equation 3.1}$$

$$G(\text{mmol}/\text{m}^2) = \frac{(\text{Conc.}_{\text{initial}} - \text{Conc.}_{\text{final}})}{SL \left( \frac{\text{m}^2}{\text{L}} \right)} \quad \text{Equation 3.2}$$

### 3.2.3 Nanoparticles Synthesis

A total surface metal density of 0.6  $\mu\text{mol}/\text{m}^2$  was desired for the synthesis of catalysts on A300 or  $\gamma\text{-Al}_2\text{O}_3$  with Pd/Au atomic ratios of 3:1, 1:1, 1:3. Monometallic Pd and Au nanomaterials were designed with the loadings around 1 wt%. The calculated amounts of precursors AuBen, PdTA-NO<sub>3</sub>, or both were dissolved into the specific volume of DI water determined by Equations 1 and 2 by using 0.8g support and intending complete uptake. Solution pH was adjusted to the value corresponded to the optimal final pH after contacting the support determined from the uptake survey. As in the adsorption experiment, 5ml solution was taken out to measure the amounts of deposited Pd and Au by ICP-OES. Then the support-contacted solution was shaken on an orbital shaker at 120 rpm for 1 hour and the powder was recovered by filtering the slurry.

To get a comparison, supported PdAu nanoparticles were also synthesized by co-DI approach by using the water accessible pore volume of the supports (2.4  $\text{cm}^3/\text{g}$  and 2.7  $\text{cm}^3/\text{g}$  for A300 and  $\gamma\text{-Al}_2\text{O}_3$ , respectively) with the precursor solution. The co-DI synthesis used the same metal precursors and amounts as well as the same support as that of the corresponding co-SEA prepared samples. The aqueous solution was gradually added into the support and the mixture slurry was shaken on a Vortex Mixer (VWR) to ensure all pores were saturated with precursor solution.

The recovered solids, or unreduced precursor form of the catalysts, were dried in air with opaque cover for over 48 hours, reduced in a horizontal reduction furnace in 20% H<sub>2</sub>, balance N<sub>2</sub>, at a total flow rate of 250 sccm at 400 °C for 1 hour with a ramp of 5°C/min,

and then stored in an amber glass vial under ambient temperature and pressure. The as-prepared samples are denoted as Pd<sub>x</sub>Au<sub>y</sub>/A300 (or Al<sub>2</sub>O<sub>3</sub>)\_co-SEA (or co-DI), therein x:y means the atomic Pd/Au ratio. Blank experiment was carried out on pure supports treated by SEA procedure without metal precursor, labeled as A300 (or Al<sub>2</sub>O<sub>3</sub>) support. Catalysts synthesis information was summarized in Table 3.2. Noticeably, controllable weight loadings of Pd and Au can be precisely achieved via co-SEA synthetic protocol.

Table 3.2 Catalysts information.

sample	atomic ratio Pd/Au		surface density (Pd+Au) mmol/m <sup>2</sup>	mass loading (%)		concn. (ppm) SEA (or DI)	
	nominal	actual		Pd	Au	PdTA-NO <sub>3</sub>	AuBen
Pd <sub>1</sub> /A300-SEA (or DI)	1:0	1:0	0.33	0.97	---	35.3 (3984)	---
Au <sub>1</sub> /A300-SEA (or DI)	0:1	0:1	0.15	---	0.84	---	38.0 (3989)
Pd <sub>3</sub> Au <sub>1</sub> /A300_co-SEA (or co-DI)	3:1	2.9:1	0.58	1.32	0.49	48.1 (5422)	29.9 (3373)
Pd <sub>1</sub> Au <sub>1</sub> /A300_co-SEA (or co-DI)	1:1	1.0:1	0.57	0.88	1.4	32.1 (3609)	59.2 (6649)
Pd <sub>1</sub> Au <sub>3</sub> /A300_co-SEA (or co-DI)	1:3	1:3.0	0.58	0.43	2.3	16.1 (1812)	88.3 (9945)
Pd <sub>1</sub> /Al <sub>2</sub> O <sub>3</sub> -SEA (or DI)	1:0	1:0	0.31	0.83	---	96.7 (1509)	---
Au <sub>1</sub> /Al <sub>2</sub> O <sub>3</sub> -SEA (or DI)	0:1	0:1	0.19	---	0.90	---	75.4 (1636)
Pd <sub>3</sub> Au <sub>1</sub> /Al <sub>2</sub> O <sub>3</sub> _co-SEA (or co-DI)	3:1	2.2:1	0.42	0.76	0.54	94.9 (1062)	33.2 (5187)
Pd <sub>1</sub> Au <sub>1</sub> /Al <sub>2</sub> O <sub>3</sub> _co-SEA (or co-DI)	1:1	1.0:1	0.60	0.82	1.40	88.0 (1871)	95.4 (3437)
Pd <sub>1</sub> Au <sub>3</sub> /Al <sub>2</sub> O <sub>3</sub> _co-SEA (or co-DI)	1:3	1:2.6	0.56	0.39	1.83	18.7 (1717)	141.2 (1447)

### 3.3 Characterization

To determine the metal content of the catalysts, inductively coupled plasma-optical emission spectrometry (ICP-OES, PerkinElmer Avio 200) was used to analyze the concentrations of Pd and Au in the precursor solutions before and after contacting with the support to determine the mass loadings.

Hydrogen temperature programmed reduction (H<sub>2</sub>-TPR) was performed on unreduced catalysts by using a Micromeritics Autochem II 2920 analyzer equipped with a

thermal conductivity detector (TCD). Samples (approximately 100 mg) were loaded and pretreated in 50 sccm Ar flow at 180 °C for 1h and then cooled down to 30 °C. The gas flow was then changed to 10% H<sub>2</sub> balance Ar and the sample was heated to 800 °C with a ramp of 5 °C/min. To verify the information on ligand removal during reduction, TPR characterization was also conducted using a custom vertical flow tubular furnace system with gas analyzer fitted with an Inficon Transpector 2 mass spectrometer (MS). Around 100 mg of fresh sample was loaded and pretreated in argon at 180 °C for 1 hour. The sample was then cooled down to room temperature with continued purging of argon until the MS baseline was stable before changing the gas flow to 20% H<sub>2</sub>, balance Ar. After reestablishing a stable MS baseline, the sample was then heated to 520 °C with a ramp of 5 °C/min.

Powder X-ray diffraction (XRD) patterns were collected on a Rigaku Miniflex-II equipped with a D/teX Ultra silicon strip detector, operated at 15 kV and 30 mA. Scans were acquired a 2 $\theta$  range of 10- 90 ° with a rate of 2 °/min by using Cu K $\alpha$  radiation ( $\lambda=1.5406$  Å) source. XRD patterns were deconvoluted using Gaussian shapes with Fityk software and average gold particle sizes were calculated with Scherrer equation by using the shape factor of 0.94 [73] based on the full-width at half maximum (FWHM) of the [111], [200], and [220] peaks.

Electron microscopy images with varied magnifications were taken on an aberration corrected JEOL 2100F scanning transmission electron microscopy (STEM) to analyze the average particle size and size distribution as well as the conceivable speckling effects. Samples were prepared by ultra-sonicating in ethanol and adding a drop of the suspension to a copper TEM grid with a thin holey carbon coating. Particle size

distributions were obtained with analysis class size of 1 Å based on over 700 particles by using Particule 2 software. Number, surface, and volume average particle diameters were calculated according to the following equations:  $D_N = \sum n_i D_i / \sum n_i$ ,  $D_S = \sum n_i D_i^3 / \sum n_i D_i^2$ ,  $D_V = \sum n_i D_i^4 / \sum n_i D_i^3$ , respectively, where  $n_i$  refers to the population of the particles for a specific particle class of size  $D_i$  [85]. Fast Fourier transform (FFT) analysis of high resolution microscopy images of Pd<sub>1</sub>Au<sub>1</sub>-co-SEA samples on silica and alumina were taken by using ImageJ software.

To probe the electronic properties of furnace-reduced mono/bimetallic PdAu samples, X-ray photo-emission spectroscopy (XPS) was performed on a Kratos AXIS Ultra DLD XPS system with a monochromatic Al K source, which was designed at 15 keV and 120 W. The acquired binding energy was corrected by using the binding energy of C1s (B.E.=284.8 eV) [131]. With a subtraction of Shirley background, XPS spectra were fitted with XPS Peak 4.1 software by using a mixed Gaussian/Lorentzian function and fixing spin-orbit splitting area ratio.

FTIR spectroscopy was carried out with a Thermo Electron model 4700 FTIR spectrometer with an MCT detector by using carbon monoxide (CO) as the probe molecule to detect the geometry of surface Pd sites. The self-supporting disk of 13 mm diameter was prepared from 15 mg finely ground sample powder on a press device with a force of 3 ton. The sample disk was then placed into the IR cell through a cylindrical sample holder and pretreated in 20% H<sub>2</sub>, balance N<sub>2</sub> at 180 °C for 1 hour. Afterwards, it was cooled down to room temperature, then 1% CO, balance Ar was flowed until the sample surface was saturated with CO, and then purged with pure N<sub>2</sub> to remove gas-phase and physically adsorbed CO molecules. The spectra were recorded by using the background taken before

CO exposure at room temperature. CO gas correction was obtained by subtracting the spectra on pure support by Fityk software.

In parallel, pulse CO-chemisorption was performed over the supported PdAu nanoparticles on the aforementioned Micromeritics Autochem II 2920 analyzer to quantify surface Pd sites. All the measured samples were *in-situ* reduced at 180 °C for 1 hour in 10% H<sub>2</sub>, balance Ar with a temperature ramp of 5 °C/min. Samples were then cooled down to room temperature under Ar flow. After establishing baseline TCD signal, 10% CO, balance He was pulsed until CO uptake was negligible. The difference between the amounts of injected CO and the measured residual amount in the gas effluent was applied to calculate the amount of adsorbed CO on surface Pd sites. The stoichiometry of CO/Pd derived from CO-FTIR analysis was applied to calculate Pd dispersion in CO-pulse chemisorption.

### **3.4 EXPERIMENTAL RESULTS AND DISCUSSIONS**

Equilibrium adsorption of Pd and Au versus solution pH was given in Fig.3.1. Adsorption patterns in volcanic shape were observed over both A300 and  $\gamma$ -Al<sub>2</sub>O<sub>3</sub> which is expected in an electrostatic adsorption mechanism [127, 132]. The maximum adsorption of Pd and/or Au appeared at 10.5-11.5 of the final pH with a subsequent sharp fall-off above this due to a very strong ionic strength, intrinsically retarding the metal adsorption [24, 133]. It is worth to mention that  $\gamma$ -Al<sub>2</sub>O<sub>3</sub> (PZC=8.3) displayed a much lower surface density (less than full monolayer) of Pd and/or Au with narrower adsorption profiles, which can be authorized to the partial deprotonation of the surface OH groups in high pH [134].



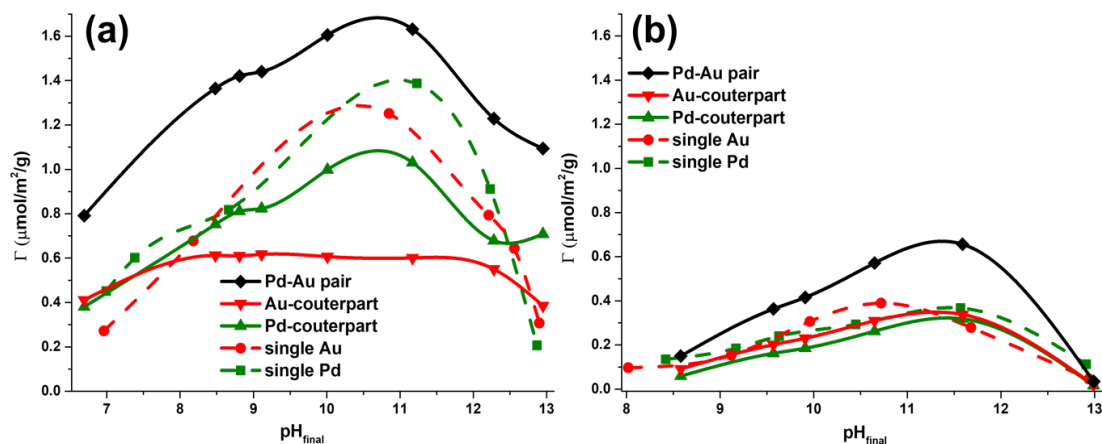


Figure 3.1 Equilibrium adsorption plots of single Pd, Au (dash lines) and Pd-Au pair (solid plots) on A300 (a) and  $\gamma\text{-Al}_2\text{O}_3$  (b).

The  $\text{H}_2$ -TPR patterns of Pd, Au, and PdAu nanoparticles on A300 and  $\gamma\text{-Al}_2\text{O}_3$  are shown in Fig.3.2. The compositions were varied to explore the reducibility of the supported PdAu materials and obtain information on the removal of precursor ligands. The negative signals at 168 °C and 152 °C (Fig. 3.2a) for monometallic Pd and Au samples prepared by SEA, respectively, can be attributed to reduction of complexes into metallic states. Also, the well-symmetric TCD signals in the temperature range of 153 - 158 °C measured over bimetallic PdAu NPs, explicitly between those of the single Pd and Au NPs, indicate the formation of homogenous alloys.  $\text{H}_2$  production peaks at 232 °C over monometallic Au/A300-SEA sample and between 190 °C to 204 °C were observed on bimetallic NPs. These might be ascribed to the disintegration of ethylenediamine ligands from AuBen precursor [127]. Furthermore, Pd addition decreased the temperature required to decompose the ethylenediamine ligands, which might be because the adjacent Pd complexes to Au impedes the migration of ethylenediamine from gold center to the support. Negative signals at 367 °C (Pd<sub>1</sub>/A300-SEA), 361 °C (Pd<sub>3</sub>Au<sub>1</sub>/A300\_co-SEA) and 513 °C

(Pd<sub>1</sub>Au<sub>1</sub>/A300\_co-SEA) can be due to the removal of ammine ligands from Pd precursor. Similar phenomena were observed on  $\gamma$ -Al<sub>2</sub>O<sub>3</sub> supported PdAu NPs synthesized by co-SEA (Figure 3.2b), except for the dip in signal for the peaks located around 230 °C to 274 °C, as well as the shoulders for Pd and Au reduction peaks over samples with Pd/Au=1:1 and 1:3, which may have resulted from the stronger acidity of alumina than silica.

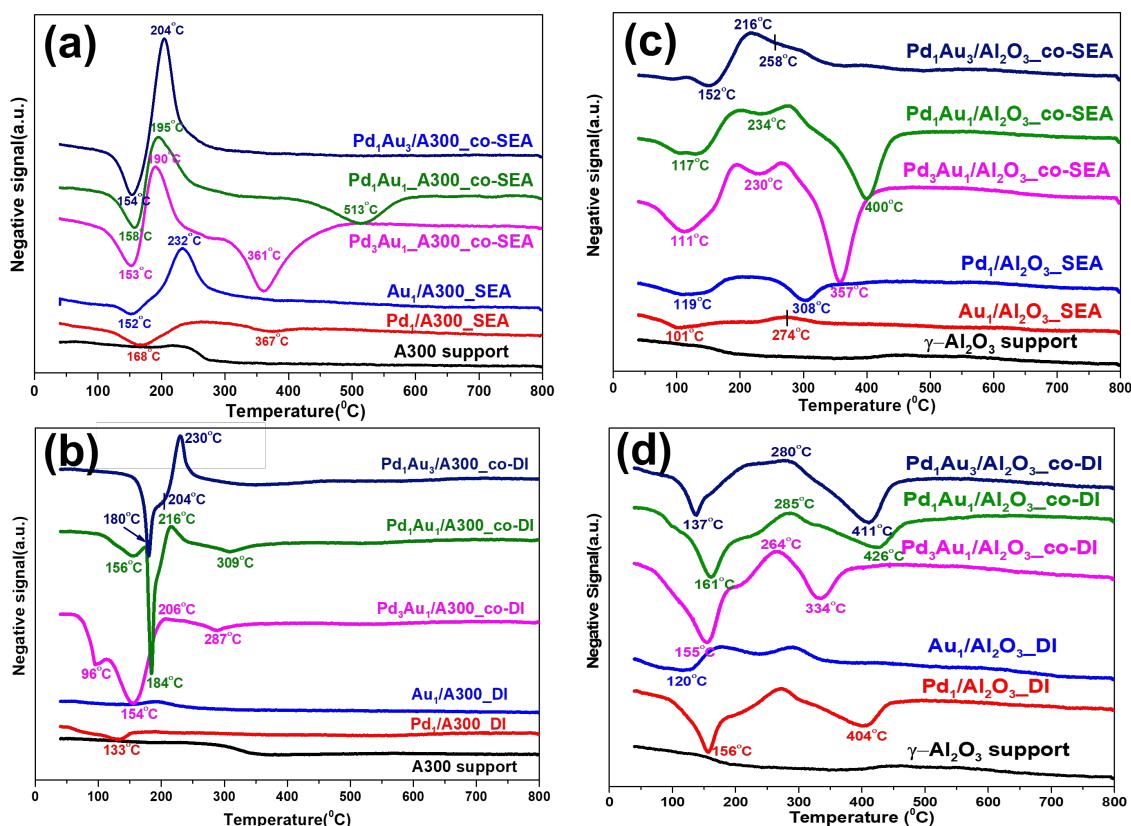


Figure 3.2 TPR profiles for PdAu catalysts on A300 by co-SEA (a), by co-DI (b); on  $\gamma$ -Al<sub>2</sub>O<sub>3</sub> by co-SEA (c), by co-DI (d).

Figure 3.3 exhibited the TPR profiles recorded by using mass spectra over Pd<sub>3</sub>Au<sub>1</sub>/Al<sub>2</sub>O<sub>3</sub>\_co-SEA, which once again confirmed the decomposition of ammine ligands at around 360 °C and the dissipation of major ethylenediamine at 160 °C and minority at 350 °C. However, co-DI prepared bimetallic PdAu NPs displayed parted reduction peaks of Pd and Au or with shoulders, an indicative of poor homogeneity. Meantime, the weaker

signals for ethylenediamine decomposition and ammine ligands removal certified the poor metal precursor-support interaction, which normally induces large particles.

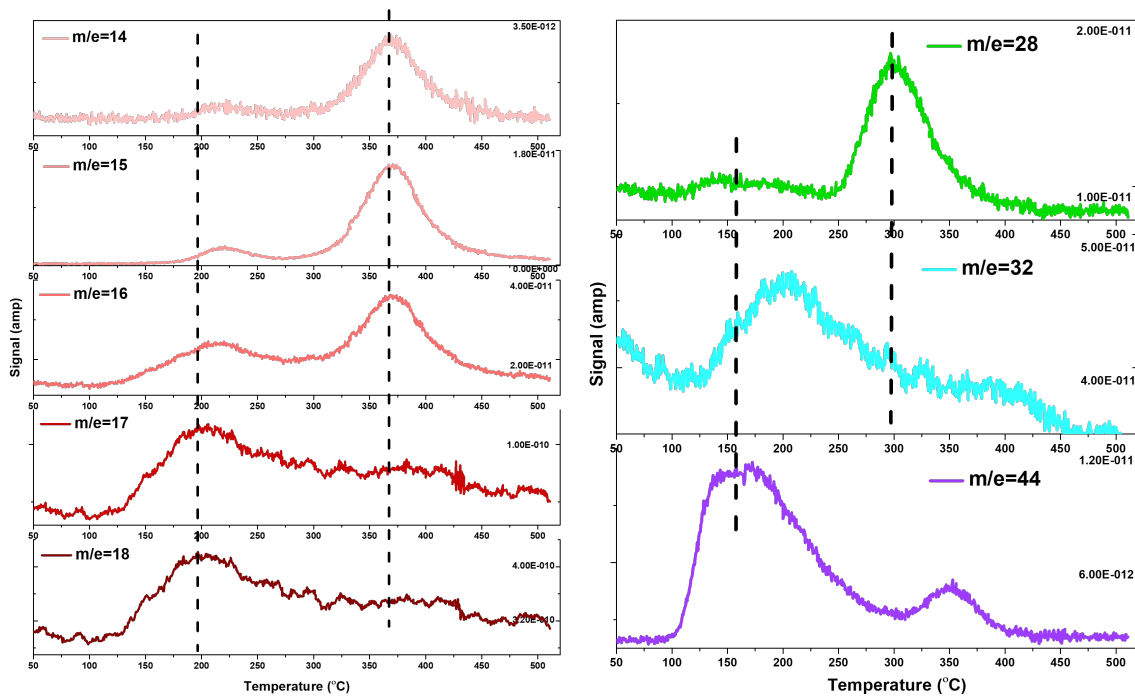


Figure 3.3 TPR-MS profiles over Pd<sub>3</sub>Au<sub>1</sub>/Al<sub>2</sub>O<sub>3</sub>\_co-SEA.

XRD profiles of monometallic and bimetallic PdAu NPs supported on A300 and  $\gamma$ -Al<sub>2</sub>O<sub>3</sub> as well as the supports are given in Fig. 3.4. Electrostatic adsorption protocol resulted in NPs that showed much broader peaks for their corresponding metals, suggesting smaller particles. For the monometallic Pd and Au NPs over A300 in Fig. 3.4a, with curve fitting over background subtracted XRD data shown in Fig. 3.5, the SEA synthesized Pd NPs can be resolved by assigning the reflections at  $2\theta = 33.63^\circ$  to Pd<sub>2</sub>O, formed due to the facile oxidation of ultra-small Pd NPs when exposed to the ambient air [128, 135]. XRD and STEM (Fig. 3.8a) analysis on Pd<sub>1</sub>/A300-SEA gave consistent particle size around

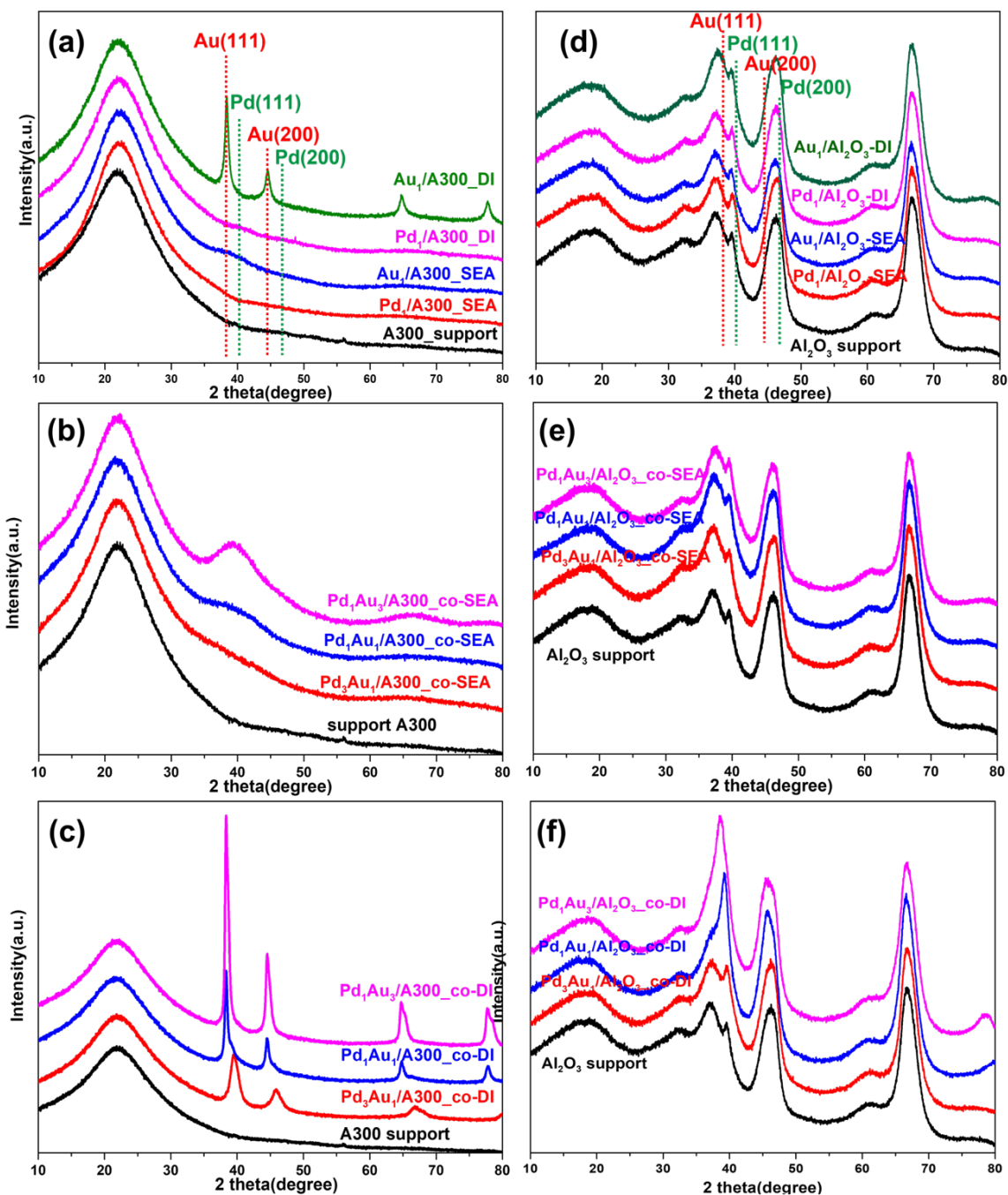


Figure 3.4 XRD patterns of monometallic Pd and Au catalysts by SEA and DI (a, d); bimetallic PdAu catalysts by co-SEA (b, e), by co-DI (c, f), wherein plots of (a-c) and (d-f) plots were over A300 and  $\gamma$ -Al<sub>2</sub>O<sub>3</sub>, respectively.

1 nm. While partial oxidation of Pd was identified over Pd<sub>1</sub>/A300-DI sample with 46.8 % of Pd<sup>0</sup> (2.0 nm) at 40.12 ° 2θ and 53.2% of Pd<sub>2</sub>O (1.2 nm) with the average particle size of 1.5 nm, larger than SEA-synthesized Pd NPs. In contrast, sharp and intense metal peaks were detected over Au<sub>1</sub>/A300-DI sample at 38.19° and 44.39° 2θ for Au [111] and Au [200], which can be fitted using bimodal particle sizes of 4.5 nm and 14.7 nm. Whereas Au<sub>1</sub>/A300-SEA yields unitary particles of 1.3 nm with considerably broad peak, in high agreement to that estimated by STEM analysis in Fig. 3.8b. Oxidation of ultra-small Au NPs was not expected over Au<sub>1</sub>/A300-SEA sample due to the high electronegativity of Au [136]. On account of the interference of the γ-Al<sub>2</sub>O<sub>3</sub> diffraction pattern, Pd and Au NPs associated diffraction peaks can be hardly observed on alumina support. While STEM study over SEA synthesized single Pd and Au NPs delivered small metal particles and the prominent signals in XRD plot around 38.19° 2θ over Au<sub>1</sub>/Al<sub>2</sub>O<sub>3</sub>-DI signified large particles.

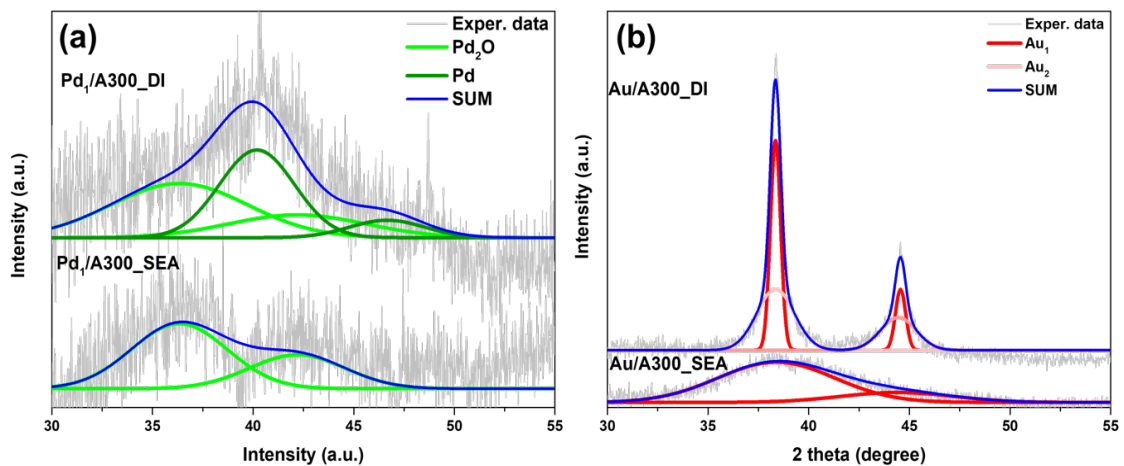


Figure 3.5 Deconvolution of monometallic Pd (a) and Au (b) nanoparticles over A300 synthesized by SEA and DI.

In the case of bimetallic PdAu nanomaterials, XRD profiles of co-SEA alloys supported on A300 (Fig.3.4b) revealed very broad peaks, which increased in intensity as the atomic ratio of Pd/Au decreased. Furthermore, no distinct diffraction features were measured over strongly adsorbed PdAu NPs onto  $\gamma$ -Al<sub>2</sub>O<sub>3</sub> (Fig.3.4e) in the most intense diffraction range of 38.19° to 40.12° 2 $\theta$  due to the formation ultra-small particle and the overlap with diffraction peaks from the support at similar positions. Careful fitting over deconvoluted XRD patterns in Fig.3.6-3.7 revealed the diffraction features of Pd<sub>2</sub>O species over co-SEA prepared NPs, which was correlated to Pd/Au ratio. The downwards shift in the Bragg region upon enhancing Pd/Au ratio can also be interpreted by the presence of Pd<sub>2</sub>O, which was expected over small Pd-rich NPs as the surface oxides formed with the alloyed PdAu underneath. It is interesting to mention that one PdAu alloy was exclusively detected over Pd<sub>1</sub>Au<sub>3</sub>/A300\_co-SEA and Pd<sub>1</sub>Au<sub>3</sub>/Al<sub>2</sub>O<sub>3</sub>\_co-SEA sample without any feature of Pd oxide species, implying the formation of homogenous alloys might prevent the oxidation of metallic Pd [137]. The detailed composition of the bimetallic PdAu alloys is summarized in Table 3.3. Here we concluded that oxidized Pd species took up a higher fraction over Pd<sub>3</sub>Au<sub>1</sub>-co-SEA sample than Pd<sub>1</sub>Au<sub>1</sub>-co-SEA, while it was absent from Pd<sub>1</sub>Au<sub>3</sub>-co-SEA, indicating the amount of oxidized Pd can be tuned by controlling the alloy composition. The detailed particle size analysis based on XRD data (Table 3.4) will be discussed later along with STEM characterization. An opposite trend in the diffraction peak which corresponded to the alteration of the composition as no Pd oxide species at lower Bragg angle occurred on larger nanoparticles. In addition, the sharp peaks with shoulder-encompassed non-Gaussian shape manifested inhomogeneous alloys with multi-phases. Similar conclusions in XRD investigation were also noted over PdAu NPs on  $\gamma$ -Al<sub>2</sub>O<sub>3</sub>.

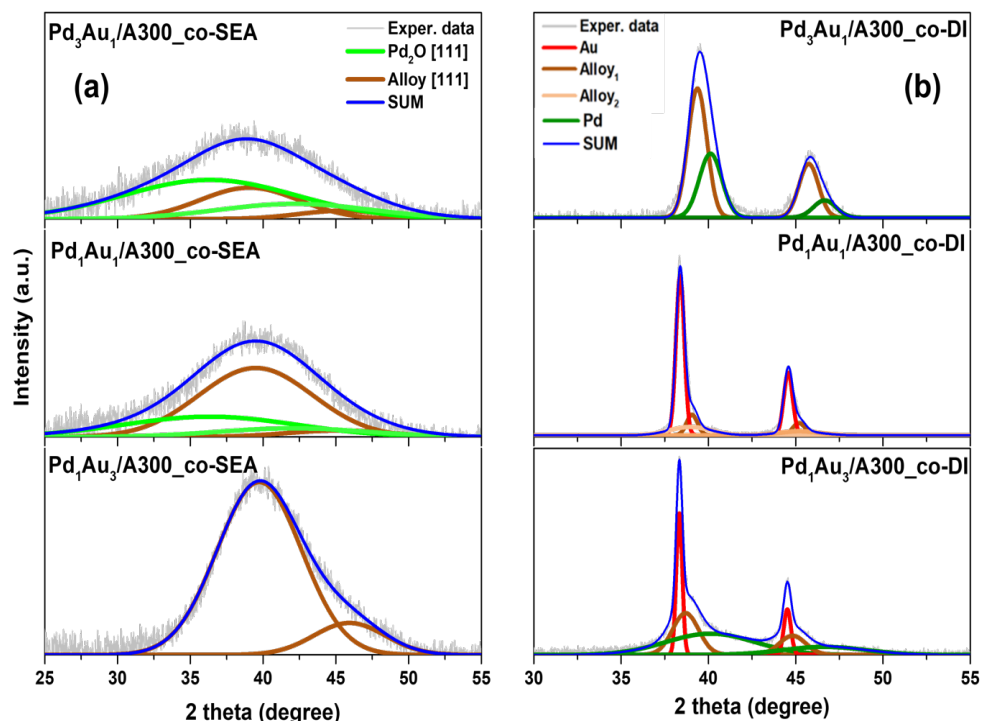


Figure 3.7 Deconvoluted XRD patterns over bimetallic PdAu nanoparticles over A300 by co-SEA (a), by co-DI (b).

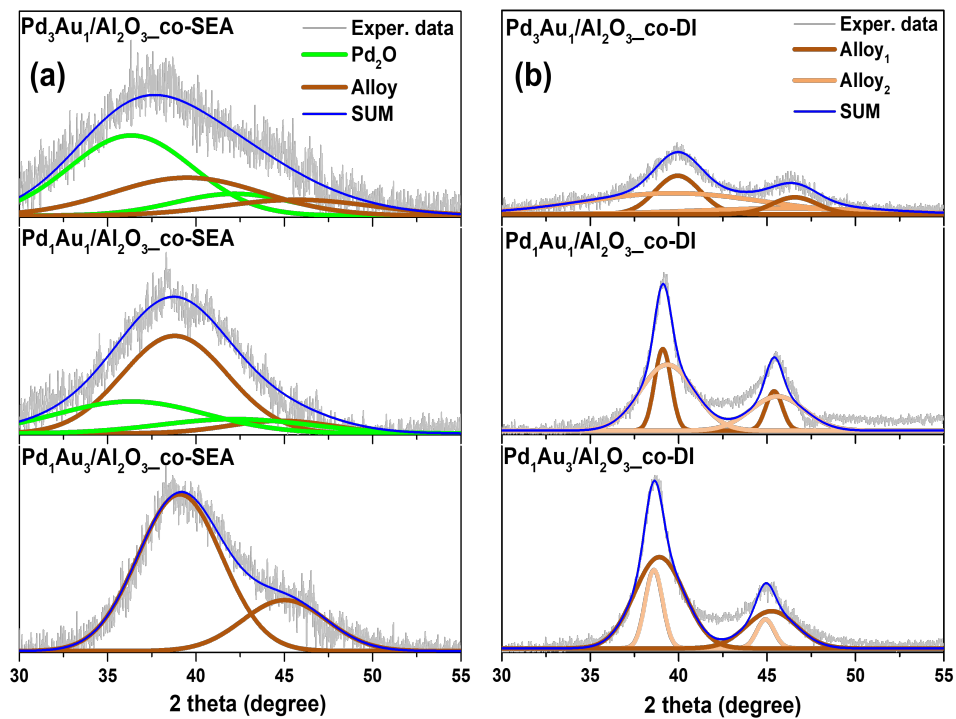


Figure 3.6 Deconvoluted XRD patterns over bimetallic PdAu nanoparticles over  $\gamma$ -Al<sub>2</sub>O<sub>3</sub> by co-SEA (a), by co-DI.

Table 3.3 Detailed composition derived from XRD pattern fitting.

sample	peak centers (area-based fraction)					
	Pd <sub>2</sub> O (70.5%)		alloy (29.5%)			
Pd <sub>3</sub> Au <sub>1</sub> /A300_co-SEA	36.33	42.19	39.06	45.41		
	0.65 nm		1.1 nm			
Pd <sub>1</sub> Au <sub>1</sub> /A300_co-SEA	Pd <sub>2</sub> O (36.0%)		alloy (64.0%)			
	36.33	42.06	39.50	45.25		
	0.66 nm		0.97 nm			
Pd <sub>1</sub> Au <sub>3</sub> /A300_co-SEA	---		alloy (100.0%)		---	
	---	---	39.74	45.94		
	---		1.3 nm			
Pd <sub>3</sub> Au <sub>1</sub> /A300_co-DI	alloy (65.6 %)		Pd (34.4 %)			
	39.37	45.75	40.12	46.66		
	6.9 nm		5.8 nm			
Pd <sub>1</sub> Au <sub>1</sub> /A300_co-DI	alloy <sub>1</sub> (43.2%)		alloy <sub>2</sub> (14.0%)		alloy <sub>3</sub> (42.8%)	
	38.33	44.53	39.06	45.41	39.17	45.55
	15.5 nm		8.1 nm		2.0 nm	
Pd <sub>1</sub> Au <sub>3</sub> /A300_co-DI	alloy <sub>1</sub> (67.8%)		alloy <sub>2</sub> (18.6%)		alloy <sub>3</sub> (13.6%)	
	38.38	44.57	38.96	45.21	39.06	45.19
	15.5 nm		3.2 nm		11.4 nm	
Pd <sub>3</sub> Au <sub>1</sub> /Al <sub>2</sub> O <sub>3</sub> _co-SEA	Pd <sub>2</sub> O (60.7%)		alloy (39.3%)			
	36.33	42.19	39.5	45.73		
	1.1 nm		0.9 nm			
Pd <sub>1</sub> Au <sub>1</sub> /Al <sub>2</sub> O <sub>3</sub> _co-SEA	Pd <sub>2</sub> O (37.5%)		alloy (62.5%)			
	36.33	42.06	39.5	45.25		
	1.3 nm		0.88 nm			
Pd <sub>1</sub> Au <sub>3</sub> /Al <sub>2</sub> O <sub>3</sub> _co-SEA	---		alloy (100.0 %)			
	---	---	39.09	45.02		
	---		1.6 nm			
Pd <sub>3</sub> Au <sub>1</sub> /Al <sub>2</sub> O <sub>3</sub> _co-DI	alloy <sub>1</sub> (62.3%)		Alloy <sub>2</sub> (37.7%)		---	
	39.71	46.57	39.95	46.03		
	1.1 nm		2.1 nm			
Pd <sub>1</sub> Au <sub>1</sub> /Al <sub>2</sub> O <sub>3</sub> _co-DI	alloy <sub>1</sub> (26.9%)		alloy <sub>2</sub> (73.1%)			
	39.11	45.4	39.36	45.6		
	8.1 nm		2.5 nm			
Pd <sub>1</sub> Au <sub>3</sub> /Al <sub>2</sub> O <sub>3</sub> _co-DI	alloy <sub>1</sub> (22.6 %)		alloy <sub>2</sub> (77.4%)			
	38.6	44.91	38.91	45.26		
	7.6 nm		2.7 nm			



To delve deeper into the morphology and microstructure of the as-obtained NPs, representative STEM images and particle size histograms were achieved for PdAu materials on A300 and  $\gamma$ -Al<sub>2</sub>O<sub>3</sub>, and shown in Fig. 3.8-3.10. Strategy of co-SEA yielded ultra-small particles ( $D_N < 2\text{nm}$ ) with uniform spherical shape and tight particle size distributions. Meticulous inspection over the magnified microscopy images of co-SEA synthesized NPs revealed evident speckling effects with brighter Au atoms in dimmer Pd clusters, evidence of random alloyed Pd and Au atoms [138]. Whereas co-DI synthesis protocol led to much larger particles with irregular shapes, and particle size histograms are unquestionably broader. STEM estimates over co-DI samples are in good accordance with the sharp peaks in XRD analysis. Interestingly, FFT analysis (Fig. B1) displayed disparate crystalline characteristics between silica and alumina supported Pd<sub>1</sub>Au<sub>1</sub> nanoparticles. Silica supported PdAu alloys showed random arrangement of Pd, Au atoms while pronounced nanocrystalline nature was present on PdAu/Al<sub>2</sub>O<sub>3</sub>\_co-SEA sample [124, 139]. Future studies are still necessary to rule out what leads to the varied crystallinity of the small PdAu NPs on amorphous silica and  $\gamma$ -alumina.

Comparison of bimetallic particle sizes derived from XRD and STEM characterization were summarized in Table 3.4. XRD analysis revealed high agreement to the number-based particle size obtained from STEM estimates. Ultra-small NPs (0.8-1.6 nm) were developed through co-SEA synthesis method. Noticeably, an observable decrease in the particle size of co-SEA materials was acquired by increasing the atomic ratio of Pd/Au, which might be interpreted by the promoted thermal stability of Au induced by the addition of Pd [140]. The co-DI prepared NPs showed a similar trend in particle size estimates. The finer co-DI yielded NPs that were present on alumina than silica can be

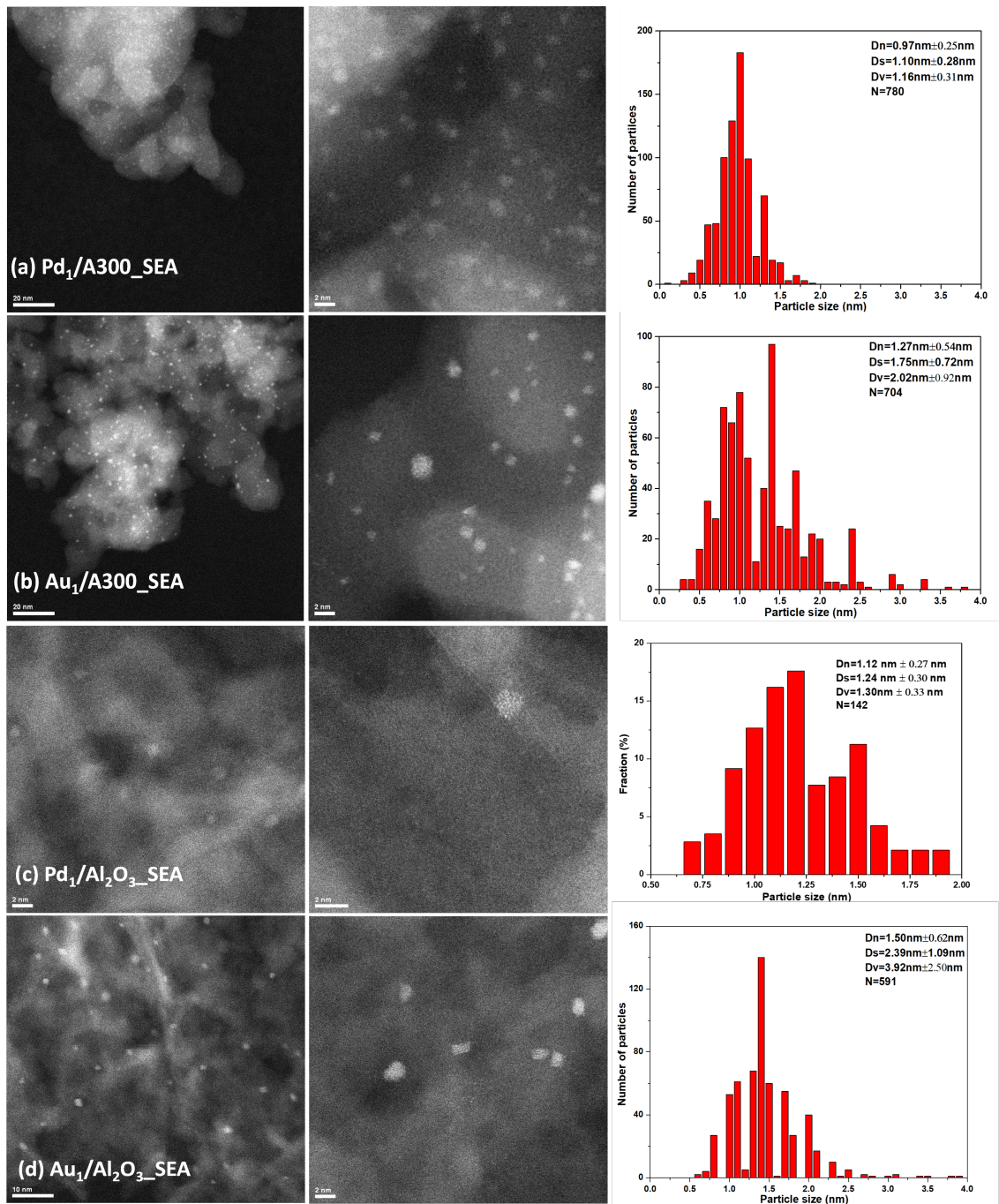


Figure 3.8 STEM images and particle size distributions for monometallic Pd and Au NPs.

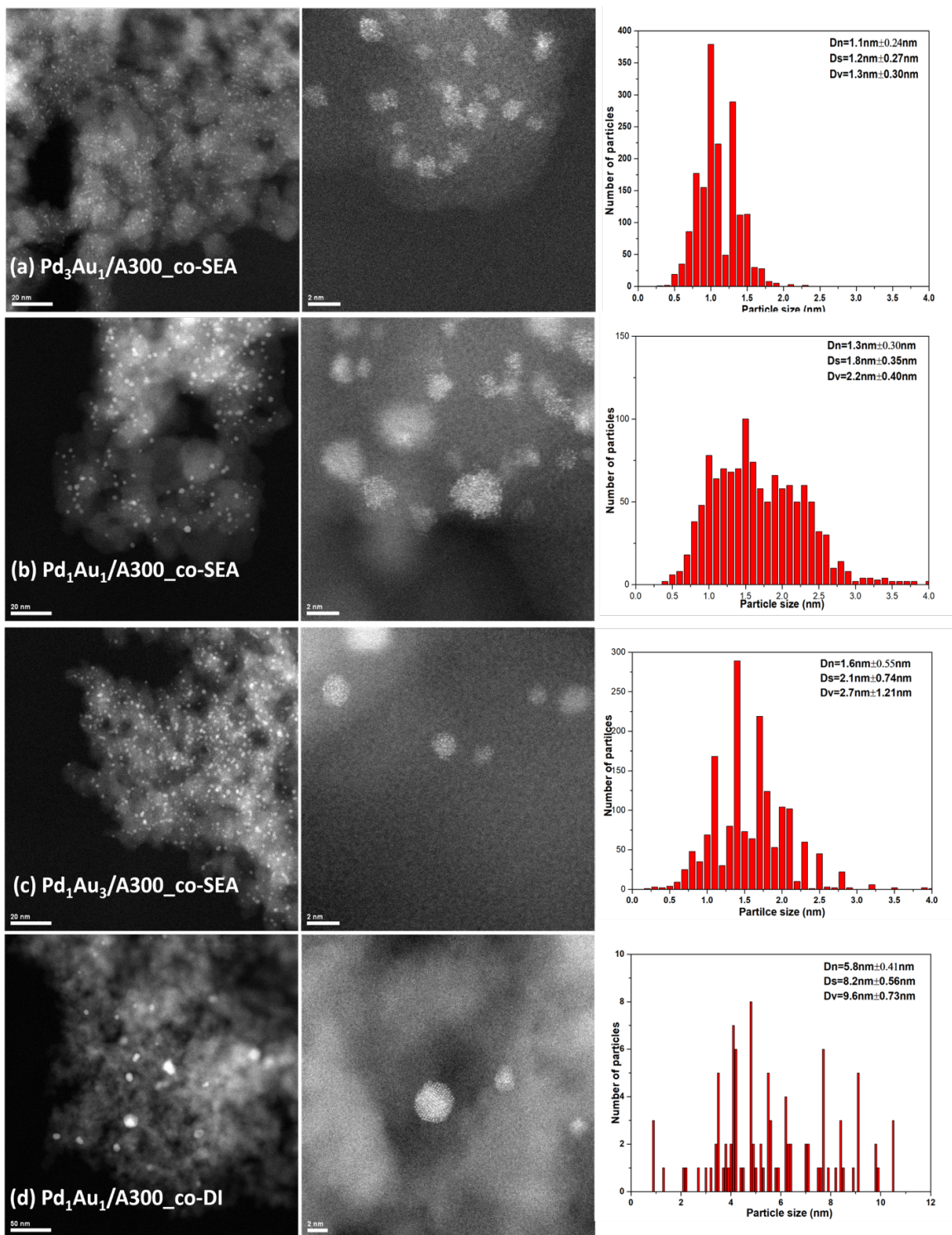


Figure 3.9 STEM images over bimetallic PdAu nanoparticles supported on A300 with varied magnifications and histograms of particle size distribution.

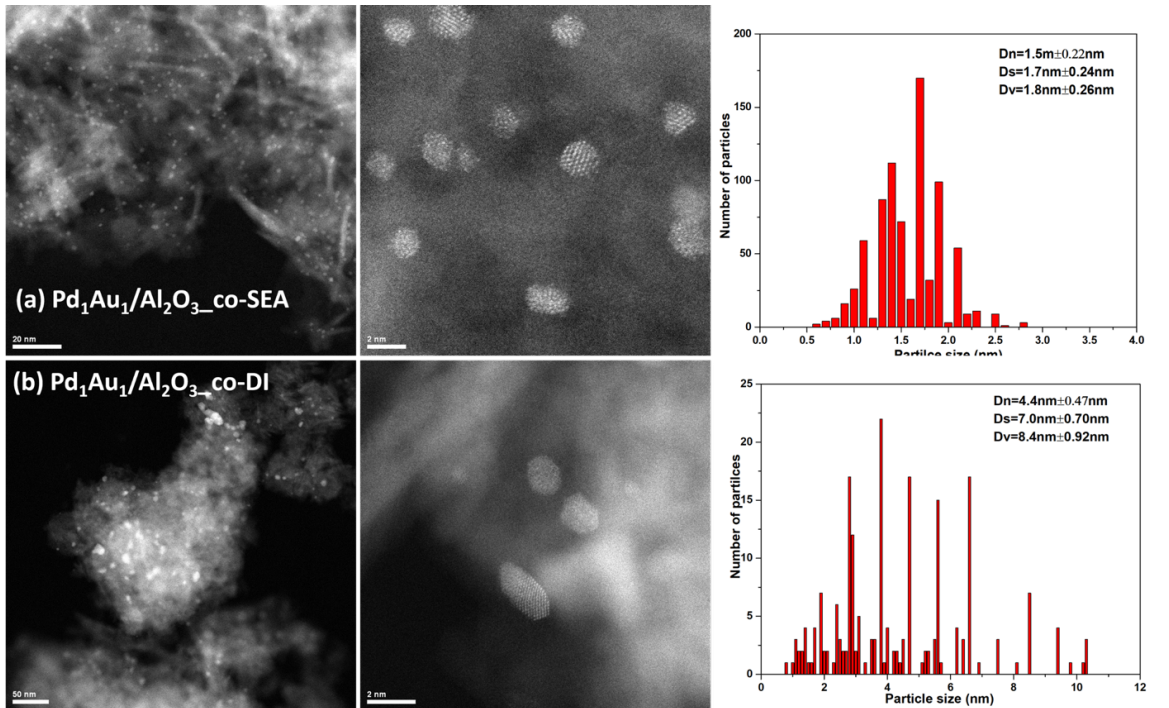


Figure 3.10 STEM images over bimetallic PdAu nanoparticles supported on  $\gamma$ -Al<sub>2</sub>O<sub>3</sub> with varied magnifications and particle size histograms.

PdTA-NO<sub>3</sub> and AuBen solution [128, 141]. Briefly summarizing the trend in the particle sizes of ascribed to buffering effects of the high PZC (8.3) alumina support in the acidic PdTA-NO<sub>3</sub> and AuBen solution [128, 141]. Briefly summarizing the trend in the particle sizes of PdAu alloys: 1) ultra-small particles are formed with uniform dispersion and homogeneous alloys over co-SEA prepared materials; 2) lower atomic Pd/Au ratio results in larger particles; 3) co-DI samples showed larger alloy particles with severe inhomogeneity. Bimetallic nanoparticles with same loading and equivalent moles of Pd and Au supported on A300 and  $\gamma$ -Al<sub>2</sub>O<sub>3</sub> presented consistent particle size derived from both XRD and STEM, suggesting the PZC of materials can hardly influence the aggregation behavior of metal atoms during the reduction treatment.

Table 3.4 Particle size comparison by XRD, STEM and CO-chemisorption analysis.

Samples	$d_{\text{XRD}}$	$d_{\text{STEM}}$ (nm)			CO-chemisorption		
	nm	$D_N$	$D_S$	$D_V$	Pd dispersion (%)	$Q_{\text{CO}}$ (cm <sup>3</sup> /g <sub>cat.</sub> )	$Q_{\text{Pd}}$ (mmol/g <sub>cat.</sub> )
Pd <sub>3</sub> Au <sub>1</sub> /A300_co-SEA	0.8	1.1	1.2	1.3	77.5	0.89	90.34
Pd <sub>1</sub> Au <sub>1</sub> /A300_co-SEA	0.9	1.3	1.8	2.2	58.0	0.63	47.99
Pd <sub>1</sub> Au <sub>3</sub> /A300_co-SEA	1.3	1.6	2.1	2.7	42.0	0.271	18.97
Pd <sub>3</sub> Au <sub>1</sub> /A300_co-DI	6.5	---	---	---	10.9	0.192	14.83
Pd <sub>1</sub> Au <sub>1</sub> /A300_co-DI	8.1	5.8	8.2	9.6	9.40	0.113	8.48
Pd <sub>1</sub> Au <sub>3</sub> /A300_co-DI	12.6	---	---	---	---	---	---
Pd <sub>3</sub> Au <sub>1</sub> /Al <sub>2</sub> O <sub>3</sub> _co-SEA	1.1	---	---	---	86.7	0.568	48.09
Pd <sub>1</sub> Au <sub>1</sub> /Al <sub>2</sub> O <sub>3</sub> _co-SEA	1.1	1.5	1.7	1.8	37.2	0.277	22.73
Pd <sub>1</sub> Au <sub>3</sub> /Al <sub>2</sub> O <sub>3</sub> _co-SEA	1.6	---	---	---	34.7	0.161	12.07
Pd <sub>3</sub> Au <sub>1</sub> /Al <sub>2</sub> O <sub>3</sub> _co-DI	1.5	---	---	---	27.7	0.177	27.66
Pd <sub>1</sub> Au <sub>1</sub> /Al <sub>2</sub> O <sub>3</sub> _co-DI	4.0	4.4	7.0	8.4	15.0	0.117	9.13
Pd <sub>1</sub> Au <sub>3</sub> /Al <sub>2</sub> O <sub>3</sub> _co-DI	3.8	---	---	---	17.9	0.078	6.21

To gain insight into the chemical structure of Pd and Au, XPS spectra of Au4f, Pd3d, Au4d were collected over SEA-prepared single Pd, Au and bimetallic NPs with Pd/Au=1, as shown in Fig. 3.11. One Pd species was exclusively detected over Pd<sub>1</sub>/A300-SEA sample with binding energy of 336.02 eV (Pd<sup>+</sup> 3d<sub>5/2</sub>) and 341.3 eV (Pd<sup>+</sup> 3d<sub>3/2</sub>) [122] which can be assigned to the Pd<sub>2</sub>O corroborated by XRD characterization. Careful peak fitting was performed on Pd<sub>1</sub>Au<sub>1</sub>/A300\_co-SEA sample to separate the spectra of Pd3d and Au4d with very close binding energies. Metallic Pd was expected over Pd<sub>1</sub>Au<sub>1</sub>/A300-co-SEA situated at the energy regime of 335.6 eV (Pd3d<sub>5/2</sub>) and 340.9 eV (Pd3d<sub>3/2</sub>) [142]. The higher binding energy of the detected Pd<sup>0</sup> might be accounted for through charge transfer in the alloyed PdAu NPs due to the lower electronegativity value of Pd compared to Au [143]. The occurrence of two typical peak sets Au4f<sub>7/2</sub>, Au4f<sub>5/2</sub> and Au4d<sub>5/2</sub>, Au4d<sub>3/2</sub> over Au<sub>1</sub>/A300-SEA and Pd<sub>1</sub>Au<sub>1</sub>/A300-co-SEA in Fig. 3.11 are associated with the metallic

state of Au. Despite the consistent binding energy of Au4f estimated from Au<sub>1</sub>/A300-SEA and Pd<sub>1</sub>Au<sub>1</sub>/A300-co-SEA, the later exhibited a slightly lower binding energy of Au4d, again attributed to the electronic interaction between Au and Pd in the alloys.

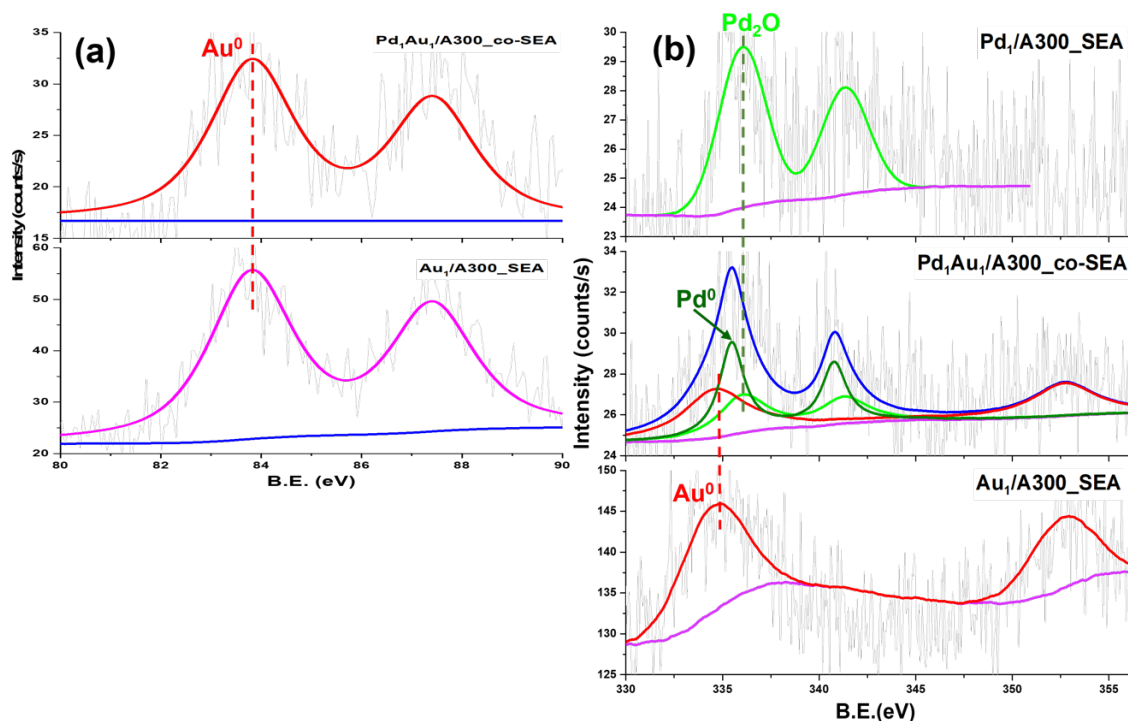


Figure 3.11 XPS spectra of Au4f (a) and Pd3d and Au4d (d) over single Pd, Au and Pd<sub>1</sub>Au<sub>1</sub> NPs synthesized by electrostatic adsorption method.

FTIR with CO as the probe molecule is a strong tool to identify the geometric structure of PdAu materials. Based on the IR spectra in Fig. B2, A300,  $\gamma$ -Al<sub>2</sub>O<sub>3</sub> and the supported single Au NPs can hardly adsorb CO molecules [144], demonstrating the detected carbonyl species on PdAu alloys are expected exclusively from exposed Pd atoms on the surface. In order to investigate the effect of composition and alloy homogeneity on the structural property of PdAu bimetallic materials, IR spectra were recorded over bimetallic PdAu NPs at 25 °C as shown in Fig. 3.12. CO stretching bands observed in the carbonyl region of 2100 cm<sup>-1</sup> - 2000 cm<sup>-1</sup> can be attributed to the linearly bonded CO on

low-coordinated Pd sites; bridge-adsorbed CO species existed in the range of 2000  $\text{cm}^{-1}$ -1900  $\text{cm}^{-1}$  on low index alloy planes; while three-fold type carbonyls on Pd species with high coordination numbers were detected in the even lower frequencies of below 1900  $\text{cm}^{-1}$  [18, 144, 145].

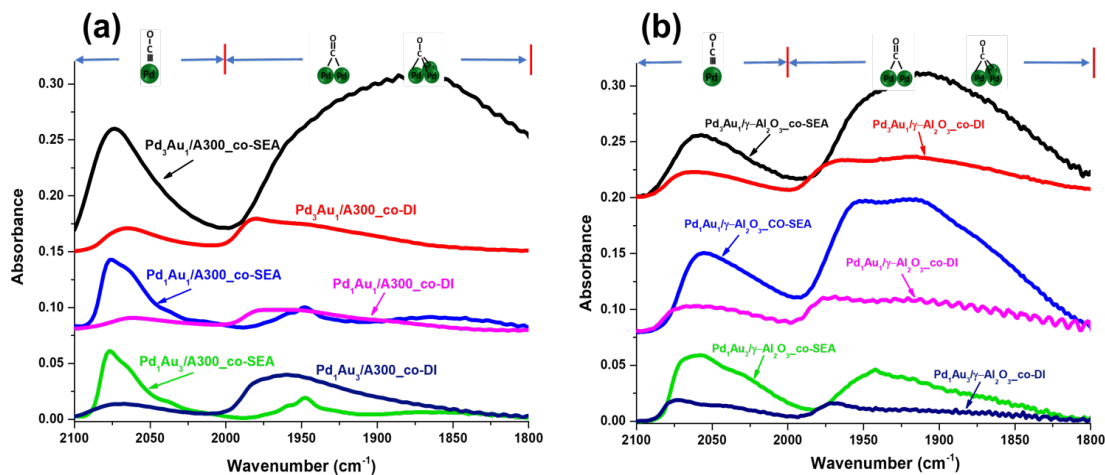


Figure 3.12 IR spectra over bimetallic PdAu nanoparticles supported on (a) A300 and (b)  $\gamma\text{-Al}_2\text{O}_3$ .

Remarkably, significant differences were observed over co-SEA and co-DI materials. Firstly, PdAu NPs prepared through co-SEA exhibited stronger signals, which can be assigned to the larger population of surface Pd atoms accessible to CO molecules due to the ultra-small particles. Secondly, considerable higher fraction of linearly adsorbed CO measured over the as-prepared PdAu alloy by co-SEA methodology was induced by the higher dispersion of Pd atoms surrounded by Au species, demonstrating enhanced homogeneity of alloys than co-DI alloys. In addition to the variations in CO absorbance between co-SEA and co-DI technique produced bimetallic NPs, a consistent trend in the fraction of linear CO on the bimetallic surface was measured on both kinds of as-prepared alloys, as more linearly bonded CO species were expected by lowering Pd/Au ratio due to

Pd surface dilution by increased amount of Au species, which was given in Fig. 3.13. In parallel, pulse CO chemisorption was employed to further explore Pd dispersion (Table 3.4). The resultant Pd distribution and quantity of adsorbed CO confirmed higher amount of Pd surface sites over co-SEA prepared co-SEA NPs, which can be explained by the ultra-small particles and homogenous alloys.

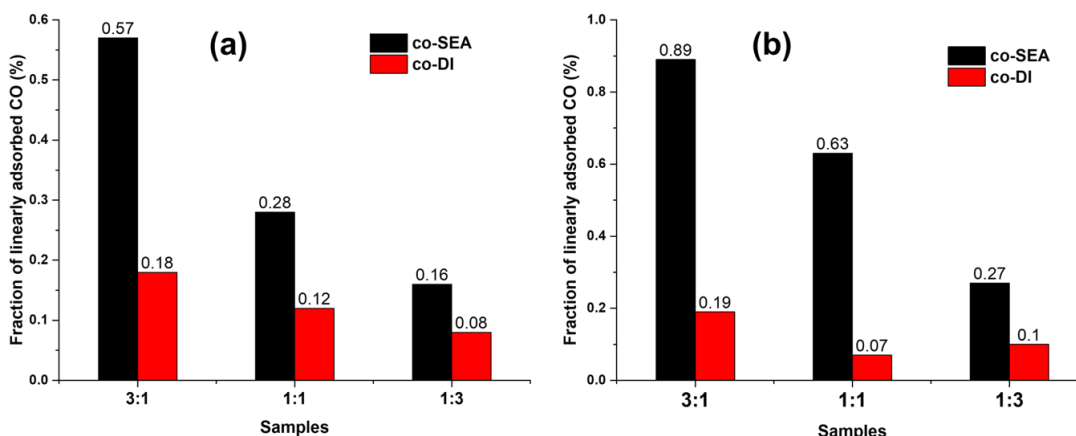


Figure 3.13 Fraction of linear-bonded CO based on deconvoluted spectra areas over A300 (a) and  $\gamma$ -Al<sub>2</sub>O<sub>3</sub> supported PdAu nanoparticles.

### 3.5 Conclusions

Strong electrostatic adsorption is an effective technique to synthesize well-defined bimetallic nanoparticles with homogenous alloys. Using co-SEA the alloy composition can be successfully controlled by tuning the concentration of Pd and Au complex precursors in the preparation procedure. The presence of Pd oxide species over co-SEA materials is due to the ultra-small particles, the amount of which is directly correlated to the alloy composition. Compared to PdAu alloys synthesized through co-DI method, increased amount of Pd sites with higher dispersion was revealed on co-SEA nanoparticles, suggesting the formation of homogenous alloys with smaller particles.



CHAPTER 4  
THE PREPARATION OF SILICA SUPPORTED, DILUTE LIMIT PDAU  
ALLOYS VIA SIMULTANEOUS STRONG ELECTROSTATIC  
ADSORPTION

**4.1 Abstract**

Supported, dilute Pd-in-Au alloyed nanoparticles might possess enhanced reactivity due to the altered structural and electronic properties of the Pd atoms isolated in an Au nanoparticle matrix. Simultaneous strong electrostatic adsorption (co-SEA) is a promising approach to synthesize such nanoparticles at high metal dispersion. In this study, diluted Pd sites in Au nanoclusters were achieved via co-SEA with dilute Pd/Au concentration ratios of the impregnating solution. XRD and STEM demonstrated ultrasmall nanoparticles (~1.7 nm) with homogenous alloying. Quantitative analysis of CO adsorption with Fourier-transform infrared spectroscopy was used to diagnose the disappearance of contiguous Pd ensembles with increasing dilution. Exclusively isolated Pd sites were achieved at or below the ratio of Pd:Au at 0.04:1. Catalysts comprising completely isolated Pd exhibited turnover frequencies four orders of magnitude higher than pure Pd catalysts.

## 4.2 Introduction

Interest has arisen for heterogeneous catalysts comprising single atom alloys (or dilute limit alloys, DLAs), in which one metal atom is diluted in the matrix of another supported metal nanoparticle, due to potentially enhanced catalytic activity, stability or other improved properties of the isolated atom [146-148]. For example, the isolation of noble metal atoms in a non-precious metal inert matrix enables the maximum noble metal utilization. Furthermore, DLA catalysts might combine the traditional advantages of alloys and single atom materials. Active metal coordination and the change in the electronic characteristics is intimately correlated to the interactions with the adsorbates, which in turn influence the catalytic performance. Numerous papers report tuned electronic properties of DLA catalysts by tailoring the atomic ratios, which are intimately related to the reactivity. It has been reported that CO could bind more weakly on isolated Pt sites in Cu nanoclusters than on Pt ensembles/monometallic nanoparticles, which could improve CO-tolerance stability or thermal stability [149, 150]. Zhang et al. [151] affirmed an altered hydrogenolysis reaction pathway from dehydrogenation to dehydration over isolated Pt-Cu catalysts. Chen and Zhang [152] reviewed the electronic structure of DLA catalysts and concluded that a combination of a lower density of state near the Fermi level, narrowing in the valence bands, and charge transfer, have a tremendous affect the adsorption behavior of reactants/intermediates in catalytic processes. Similarly, Pei et al. [153] reported that excess electrons on the surface Pd monomers from the alloyed Ag matrix boosted the catalytic performance in acetylene hydrogenation. Density functional theory (DFT) simulation has also shown charge transfer in the dilute limit alloys, which influences the adsorption strength of various species [154].

Catalysts with isolated Pd sites anchored on the surface of Au nanoparticles have shown initial promise for many reactions such as hydrogenation, dehydrogenation, oxidation, C-C coupling, etc. [140, 155-157]. For example, Liu and colleagues [158] reported that a small amount of Pd in Au nanoparticles improved the activity of Au in the hydrogenation of 1-hexyne by nearly 10-fold, while at the same time retaining its high selectivity. It was reported that the isolated Pd atoms on Au surface facilitated hydrogen dissociation and bonded CO and H atoms more weakly. Indeed, Lee et al. [159] recently reviewed the available literature, and noted that dilute alloy catalysts with isolated atom or small ensembles in Cu, Ag, or Au host metals generally showed highly selective and enhanced hydrogenation activity. These effects are not limited to hydrogenation, as Wrasman and the co-authors [160] have shown that dilute Pd/Au alloy nanoparticles can generate the active oxidant in selective alcohol oxidation. This effect occurs even on inert carbon support due to the intensified hydrogen dissociation ability of isolated Pd sites. Finally, it has been also reported that DLA catalysts with isolated metal sites showed enhanced anti-coking and/or CO poisoning activation [149, 157].

A facile and generalizable method to synthesize supported single atom or dilute limit alloys with high metal dispersion and controlled composition will benefit efforts to explore these materials. Current preparation techniques most frequently include vacuum physical deposition (VPD), galvanic displacement (GD), sequential reduction (SR), and co-precipitation or deposition-precipitation [107, 158]. Each of these methods has drawbacks; VPD is equipment-intensive, subject to impurities and not so scalable, while SR and precipitation methods involve incipient impregnation or colloidal synthesis, which

normally produce large particles. Galvanic displacement is possible for only a limited number of metal systems.

We have previously demonstrated that simultaneous electrostatic adsorption (co-SEA) is an effective method to synthesize highly-dispersed and well-alloyed bimetallic nanoparticles (~1nm) with 1:1 atomic ratios [161]. This simple method can be applied to a wide variety of metal precursors and oxide and carbon supports [162]. The synthesis of dilute limit alloys can be achieved simply by controlling the concentrations of metal precursors in the impregnating solution. We have recently demonstrated the co-SEA synthesis of dilute Pd-in-Cu alloys on silica, revealed by rigorous fitting and DFT interpretation of CO FTIR spectra [28].

In this chapter, we extend co-SEA to the synthesis of a series of silica supported DLA nanoparticles of Pd isolated in Au. With a comprehensive battery of characterization, we combine *in-situ* IR spectroscopy and chemisorption to probe the isolation of surface Pd sites in Au ensembles and the fraction of surface Pd. Powder XRD and STEM reveal particle size and the homogeneity of PdAu alloying. *In-situ* XPS reveals electronic interactions between the two metals. The DLA series was finally characterized by evaluating the reactivity for the partial oxidation of 1-phenylethanol, showing significant improvement in activity.

### 4.3 Experimental

Aerosil 300 (A300) from Evonik Corporation was used as amorphous silica support with the surface area of 283 m<sup>2</sup>/g. The point of zero charge (PZC) of A300 is 3.6 and water-accessible pore volume is 3.2 ml/g. Tetraamminepalladium (II) nitrate solution (99.99%, Sigma-Aldrich) (Pd(TANO<sub>3</sub>)) and gold ethylenediamine Au(en)<sub>2</sub>Cl<sub>3</sub> (AuBen) was used as

the cationic Pd and Au precursor, respectively. AuBen was made from tetrachloroauric (III) acid trihydrate (99.9%, Alfa Aesar) according to the reported literature [127, 163]. Other chemicals in AuBen preparation involve diethyl ether (99.9%, VWR), ethylenediamine (99%, Alfa Aesar) and anhydrous ethanol (>99.5, sigma-aldrich). NaOH and HCl were used to adjust the solution pH, which were supplied by VWR.

#### 4.2.1 Catalysts Preparation

The synthesized series, including the electrostatic adsorption of hydrated Pd and Au cationic complexes onto the deprotonated and negatively charged silica surface is depicted in Fig. 4.1. It is presumed that drying and reduction in hydrogen leads to nanoparticles of the same composition as the adsorbed layer of well-mixed precursors. Molar Pd/Au ratios of 1.27:1, 0.23:1, 0.080:1, 0.040:1, 0.020:1, 0.012:1 and 0.010:1 were obtained by controlling Pd concentrations listed in Table 4.1. The mass of Pd was diluted from 1.54 wt% to 0.01 wt%, while Au loading was targeted at 2.3 wt% Au. The initial pH of the 0.34L metal precursor solution was adjusted to around 11.5, then 1.2 g silica support was added. The slurry was placed on an orbital shaker for 1 hour and then

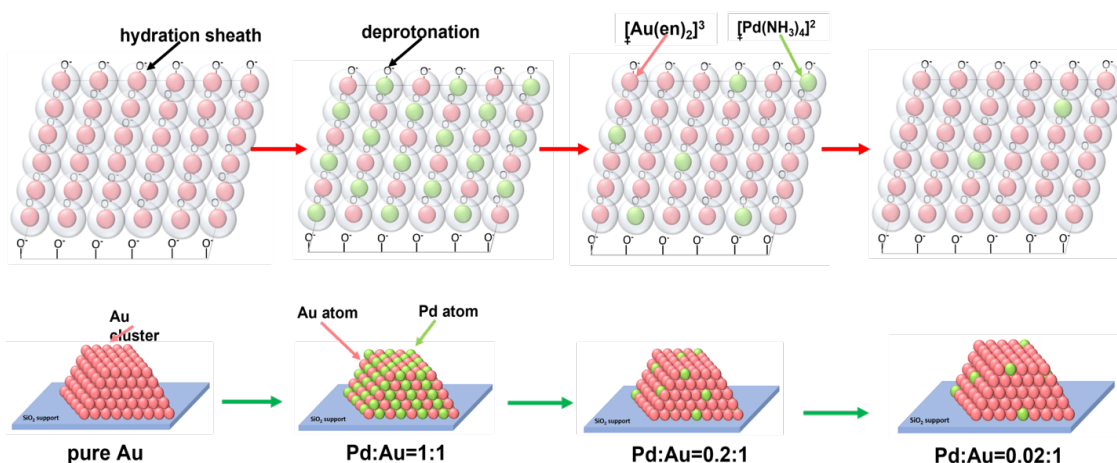


Figure 4.1 Electrostatic adsorption of Pd, Au precursor complexes on silica support (a); Palladium and/or Pd-Au alloy formed on gold clusters after H<sub>2</sub> reduction (b).

vacuum filtered to obtain the powder catalysts. Five ml aliquots of precursor solution were taken before and after contacting the support to determine the loadings of Pd and Au as measured by ICP-OES (PerkinElmer Optima 2000 DV).

For the sake of comparison, monometallic Pd, Au catalysts were produced by SEA and one bimetallic catalyst (Pd/Au=0.02:1) was made by simultaneous dry impregnation (co-DI). For the latter preparation, appropriate amounts of metal precursors were dissolved into 3.84 ml DI water, which was the water accessible pore volume of 1.2 g of the silica support. As a control, pure silica support was treated in a metal free ethylenediamine aqueous solution to simulate the SEA procedure in the absence of metals.

Table 4.1 Catalysts information and concentrations of metal precursors in the synthesis.

Catalysts	molar ratio		mass loading (wt%)		precursor conc. (ppm)	
	Pd <sub>x</sub> :Au <sub>1</sub>	Pd <sub>1</sub> :Au <sub>y</sub>	Pd	Au	PdTA	AuBen
<b>Pd<sub>1</sub>Au<sub>1</sub></b>	1:1	1:1	0.88	1.45	32	59
<b>Pd<sub>1.27</sub>Au<sub>1</sub></b>	1.27:1	1:0.79	1.54	2.2	45	84
<b>Pd<sub>0.227</sub>Au<sub>1</sub></b>	0.227:1	1:4.4	0.27	2.3	8.9	84
<b>Pd<sub>0.08</sub>Au<sub>1</sub></b>	0.080:1	1:13	0.10	2.3	3.0	84
<b>Pd<sub>0.04</sub>Au<sub>1</sub></b>	0.040:1	1:25	0.05	2.2	1.5	84
<b>Pd<sub>0.02</sub>Au<sub>1</sub></b>	0.020:1	1:50	0.024	2.3	0.74	84
<b>Pd<sub>0.012</sub>Au<sub>1</sub></b>	0.012:1	1:83	0.014	2.2	0.54	84
<b>Pd<sub>0.01</sub>Au<sub>1</sub></b>	0.010:1	1:100	0.010	2.3	0.37	84
<b>Au<sub>2.2</sub></b>	0:1	0:1	---	2.2	0	84
<b>Au<sub>1</sub></b>	0:1	0:1	---	0.84	0	40
<b>Pd<sub>0.97</sub></b>	1:0	1:0	0.97	---	36	---
<b>Pd<sub>0.10</sub></b>	1:0	1:0	0.10	---	3.6	---
<b>Pd<sub>0.02</sub>Au<sub>1</sub>_co-DI</b>	0.020:1	1:50	0.024	2.3	92	8670

The wet powders were dried at room temperature for 48 hours in darkness, and then reduced in a horizontal reduction furnace at 400 °C for 1 hour at the ramp rate of 5 °C in 250 sccm of 20 % H<sub>2</sub> in N<sub>2</sub>. The co-SEA prepared catalysts were denoted as Pd<sub>x</sub>Au<sub>1</sub>, where *x* is the molar ratio of Pd/Au. In the labels of the monometallic catalysts, the subscripts indicate the metal loadings. The samples labelled as Pd<sub>0.02</sub>Au<sub>1</sub>\_co-DI was produced by dry impregnation.

### 4.3 Characterization and evaluation

Temperature programmed reduction (TPR) was conducted in a Micromeritics 2920 equipped with a thermal conductivity detector. Fresh samples of around 200 mg were pretreated in Ar at 180 °C for 1 hour, cooled down to room temperature, switched to 10% H<sub>2</sub>/Ar at flowrate of 50 sccm, and then increased to 800 °C at a ramp of 5 °C/min.

Powder X-ray diffraction (XRD) was carried out with a Rigaku MiniFlex II with a high sensitivity D/teX Ultra Si slit detector. XRD patterns were recorded from 10-90° 2 $\theta$  with 0.02° step size using a Cu-K $\alpha$  radiation source ( $\lambda$  =1.5406 Å) at 30 mA and 15kV. Fityk version 1.1.3 software was employed for silica background subtraction and peak fitting. Average particle sizes were determined with the Scherrer equation with a shape factor of 0.94 [73].

Pulse CO-chemisorption was measured over PdAu DLA catalysts on a Micromeritics 2920 equipped with a TCD to quantify Pd sites on Au nanoparticles surface. All the measured samples were *in-situ* reduced in a U-tube installed into the equipment at 400 °C for 1 hour in 10% H<sub>2</sub>/Ar at a ramp of 5 °C/min, cooled down to room temperature and then pulsed with 10% CO/He until the discretely injected gas volumes was unchanged by TCD. The difference between the amounts of injected CO and the measured residual

amount in the gas effluent was used to calculate the amount of adsorbed CO on PdAu alloys. A small volume of CO was detected over the monometallic Au sample ( $0.05 \text{ cm}^3/\text{g}_{\text{cat}}$ ), which was then subtracted from the DLA catalysts to determine the population of adsorbed CO on Pd. The stoichiometry of CO/Pd derived from CO-FTIR analysis was applied to estimate Pd dispersion.

An aberration corrected JEOL 2100F scanning transmission electron microscopy (STEM) was employed to obtain average particle sizes and size distributions as well as to image the bimetallic nanoparticles at high magnification. Sample preparation involved ultra-sonicating the catalyst powder in ethanol and adding a drop to the copper TEM grid supporting a holey carbon film. Particle size distributions were achieved with analysis class size of  $1 \text{ \AA}$  based on at least 700 particles by using Particle 2 software. Number average particle sizes were calculated as  $D_n = \sum n_i D_i^2 / \sum n_i D_i$  and the volume average size, for comparison with XRD, as  $D_v = \sum n_i D_i^4 / \sum n_i D_i^3$  [85].

To probe the electronic structure and surface composition of the reduced PdAu DLA samples, X-ray photo-emission spectroscopy (XPS) was performed on a Kratos AXIS Ultra DLD XPS system with a monochromatic Al K source and a catalysis cell for *in-situ* pretreatment. Before procuring spectra, samples were *in-situ* reduced in the chamber at  $180^\circ\text{C}$  for 1h in 20 %H<sub>2</sub>. Binding energy was calibrated with the C1s peak at 284.8 eV [131]. With a subtraction of Shirley background, XPS spectra were fitted with XPS Peak 4.1 software by using a mixed Gaussian/Lorentzian function and fixing spin-orbit splitting area ratio.

Fourier-transform infrared spectroscopy (FTIR) with CO as probe molecule was employed to probe the atomic geometry of surface Pd sites. FTIR measurements were



performed on a Thermo Electron model 4700 spectrometer in transmission mode with a liquid-nitrogen-cooled MCT detector. A cylindrical stainless-steel cell was used in all FTIR experiments for *in-situ* pretreatment. After fine grinding, 15 mg sample was pressed into pellets in a diameter of 0.5 inch under the pressure of 3 bar for 20s. The spectra were recorded in a single beam mode with a total of 64 scans and a resolution of 4 cm<sup>-1</sup> in the 4000-4500 cm<sup>-1</sup> spectral region. Prior to collecting the spectra, each sample was firstly reduced in 20% H<sub>2</sub>/N<sub>2</sub> at 180 °C for 1 hour at the ramp of 5 °C/min, cooled down to room temperature in N<sub>2</sub>, with one spectrum collected and set as the background. The lower reduction temperature was employed for *the in-situ* IR characterization as it completely eliminated the adsorption of CO onto Au. Afterward, 1% CO/Ar was turned on and spectra were collected until the sample was saturated with CO. Subsequently, 1% CO/Ar was switched by pure N<sub>2</sub> to flush away the gas-phase and any physisorbed CO. Meanwhile, spectra were acquired until the signal of adsorbed CO signal stabilized.

Gaussian functions were used to resolve IR spectra subtracted that of the pure Au sample by using Fityk software. Curve fitting was firstly conducted on monometallic Pd catalysts to optimize the full width at half maximum (FWHM) in the Gaussian function and deconvoluted CO bands position. In the deconvolution of IR spectra over PdAu DLA catalysts, the obtained peak parameters, including FWHM, height and position, were initially used with the subsequent optimization by altering mainly the peak height, while subtly the peak position and FWHM until got a good fitting. The deconvoluted peak area corresponded to varied CO bands were used to calculate the fraction of linearly adsorbed CO molecules.

#### 4.4 Partial Oxidation of 1-Phenylethanol

Catalyst evaluation was collected and analyzed by Dr. Abolfazl Shakouri in University of South Carolina. Catalysts were evaluated for the partial oxidation (or dehydrogenation) of 1-phenylethanol (PE) to acetophenone in a 110 ml semi-batch reactor (Autoclave Engineers) at 50 psig of O<sub>2</sub> and 160 °C, with a stirring rate of 400 rpm. In all cases, 50 ml 1-phenylethanol was charged into the reactor together with 106 mg catalyst. The reactor was equipped with a rupture disk and a hollow shaft of impeller turbine with holes on top and bottom (Dispersamax<sup>TM</sup>, Autoclave Engineers). Besides, a needle valve attached to the reactor was used to control O<sub>2</sub> flow, which was opened merely to the reach and maintain the required O<sub>2</sub> pressure in the reaction. A heating jacket with a thermal couple was used outside of the vessel to get the required reaction temperature. After setting up the reactor, pure O<sub>2</sub> was purged into the reactor several times to remove the air inside and O<sub>2</sub> pressure was set as 50 psig. No stirring was started to limit the reaction rate. Upon the reaction temperature reached 160 °C, stirring started and the speed was set at 400 rpm, which was initiated as the start of the reaction. A little bit of liquid sample was taken out at interval of 10 min or 30 min and the composition was measured using a gas chromatograph (HP 5890) coupled to an autosampler with an HP-5 capillary column and a flame ionization detector. Turnover frequencies (TOFs) based on Pd was calculated according to the following equations:

$$\text{Conversion (\%)} = \frac{\text{converted } n_{PE} \text{ (mol)}}{\text{initial } n_{PE} \text{ (mol)}} * 100 \quad \text{equation (1)}$$

$$\text{TOF}_{Pd} = \frac{\text{converted } n_{PE} \text{ (mol)}}{n_{Pd} \text{ (mol)} * \text{reaction time (h)}} \quad \text{equation (2)}$$

## 4.5 Results and discussion

### 4.5.1 Catalysts Characterization

Temperature programmed reduction profiles for pure Au, Pd, and Pd/Au bimetallic nanoparticles (Fig. 4.2) showed reduction of pure Au at about 145 °C and pure Pd via SEA at about 170 °C. A DI-derived Pd sample at the same loading gave a lower reduction peak, presumably due to weaker interaction of the precursor with the silica surface. The reduction temperature of the 1:1 Pd:Au sample lowered toward that of Au, and low ratios of Pd:Au looked similar to pure Au. The Au-containing samples contained positive peaks from 200 - 250 °C presumed due to the decomposition of ethylenediamine ligand from gold precursor [164]. This peak shifted downward in temperature with the addition of even small amounts of Pd and in proportion to the amount of Pd added, which is an indication that the two metals are in intimate contact.

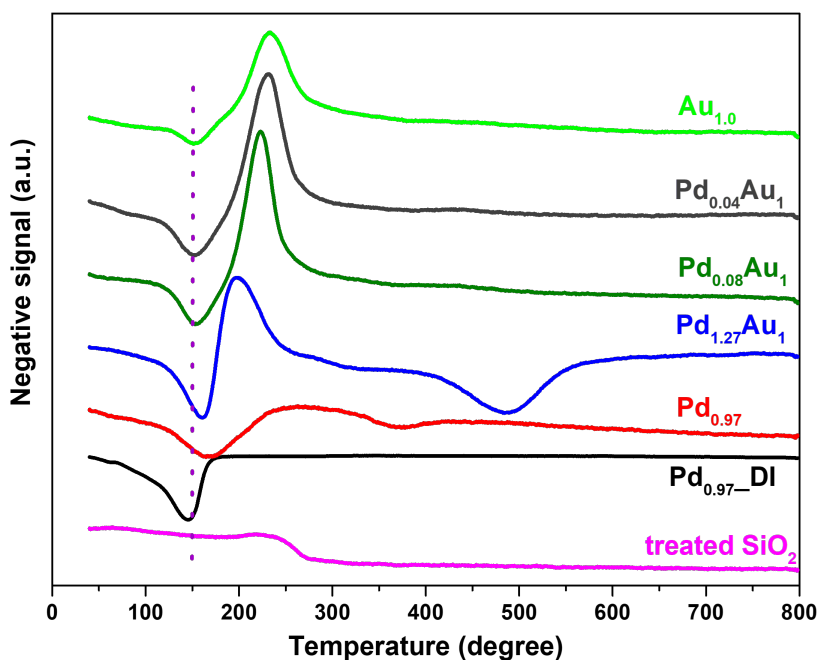


Figure 4.2 TPR profiles of PdAu DLA catalysts and the support.

Powder XRD characterization of the PdAu DLA catalysts is shown in Fig. 4.3. Raw diffractograms (Fig. 4.3a) are for the support-only (bottom), 0.97 wt% Pd-only (second from bottom), the DLA series, and then Au-only pattern (top). With the high intensity detector employed, careful background subtraction and peak fitting allows the identification of nanocrystalline features even smaller than 1 nm [165]. The Pd-only sample exhibits discernable broad peaks (Fig. 4.3b, bottom) which can be fit as 1 nm Pd<sub>2</sub>O particles. The Au-only sample (top pattern of Fig. 4.3a) can be fit with metallic fcc Au peaks with size 1.7 nm, however, the position of the (111) peak, at 39.1° 2θ, is about 0.83° 2θ higher than that expected for bulk Au. This can be explained by the lattice contraction of ultrasmall Au nanoparticles as has been firmly established by x-ray absorbance [166]. The rest of the samples, containing high to low amounts of Pd (bottom to top in Fig. 4.3a and 3b) can all be fit with a single set of fcc (111) and (200) peaks. The samples at higher Pd:Au ratios show an upward shift in 2θ which approaches pure Au at the lowest Pd ratios. As the size of the Au-rich phase remains the same, the upward shift in 2θ with high amounts of Pd implies alloying of the two metals. The peak positions from the raw data, and peaks shifts with a correction for the lattice contraction of Au are shown in Figure 4.3c. No discernable alloying is seen at the lowest Pd ratios, while above 0.04:1 Pd:Au the corrected data agree with Vegard's law [167, 168], until the final ratio of 1:27:1, at which point the Au lattice contraction correction is not needed, possibly due to the presence of large amounts of Pd.

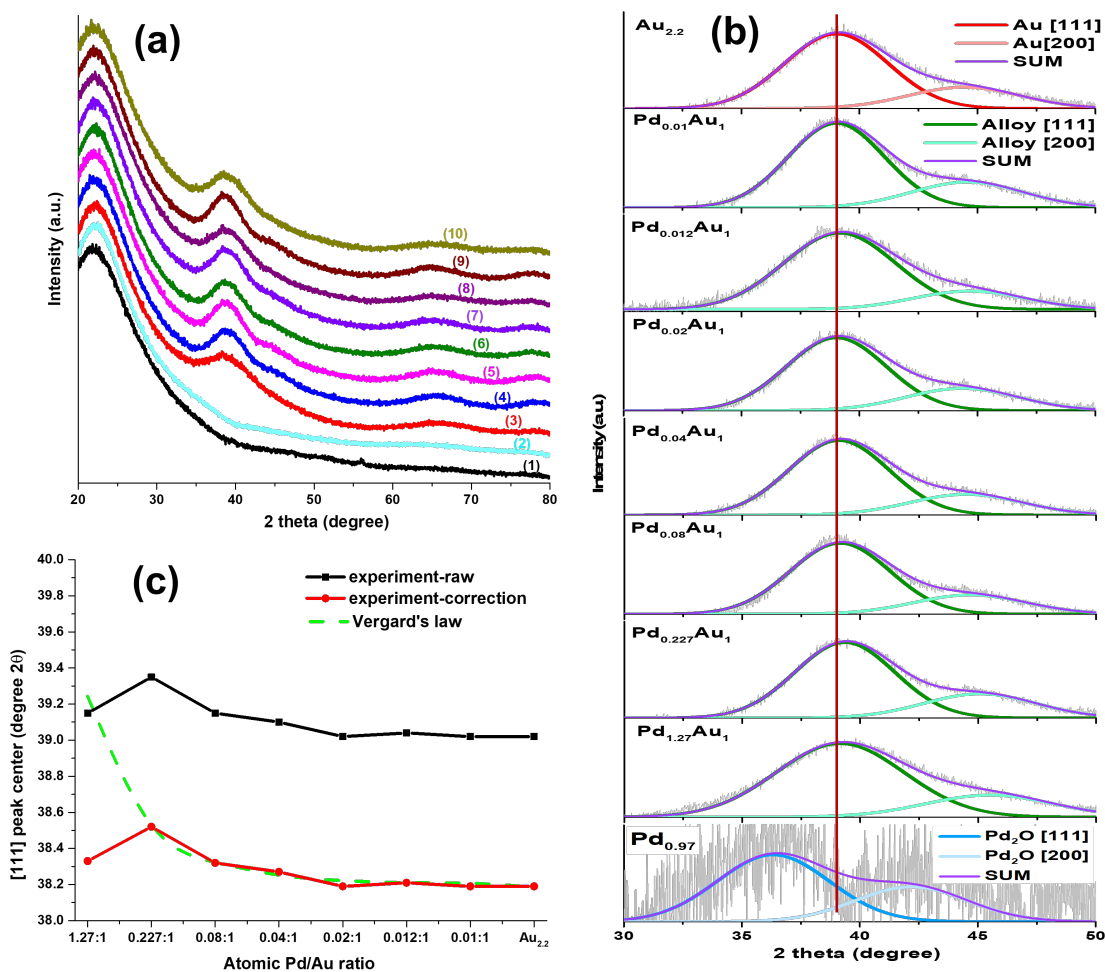


Figure 4.3 XRD analysis of the PdAu DLA series, a) Normalized XRD profiles for (1) treated SiO<sub>2</sub>, (2) Pd<sub>1.54</sub>, (3) Pd<sub>1.27</sub>Au<sub>1</sub>, (4) Pd<sub>0.227</sub>Au<sub>1</sub>, (5) Pd<sub>0.08</sub>Au<sub>1</sub>, (6) Pd<sub>0.04</sub>Au<sub>1</sub>, (7) Pd<sub>0.02</sub>Au<sub>1</sub>, (8) Pd<sub>0.012</sub>Au<sub>1</sub>, (9) Pd<sub>0.01</sub>Au<sub>1</sub>, (10) Au<sub>2.2</sub> catalysts, b) background-subtracted and fitted patterns, c) comparison of results with Vegard's law.

Particle sizes derived from the peak broadening are given in Table 4.2. All of the gold-rich catalysts have the same size (about 1.7 nm) as the pure Au sample. The highest ratio of Pd<sub>1.27</sub>Au<sub>1</sub> exhibited the smallest bimetallic particles of 1.4 nm. Pei et al [140] detected smaller bimetallic particles with even trace amounts of Pd in Au (from 4.2 nm to 2.8 nm) and concluded Pd promoted the thermal stability of Au nanoclusters which caused a stronger PdAu-silica interaction. Qian et al [169] also noticed smaller size of PdAu alloys with increased amount of Pd in fixed Au contents (from 4.0 nm to 2.3 nm) and ascribed it

to the enhancement of Au dispersion by the alloy formation. In contrast, sharp metallic [111] and [200] peaks appeared for a Pd<sub>0.12</sub>Au<sub>1</sub>\_co-DI sample (Fig. 4.4), indicative of larger alloy particles. Peaking fitting reveals two sets slightly offset FCC peaks, indicating two alloy phases with the average particle size of 11 nm.

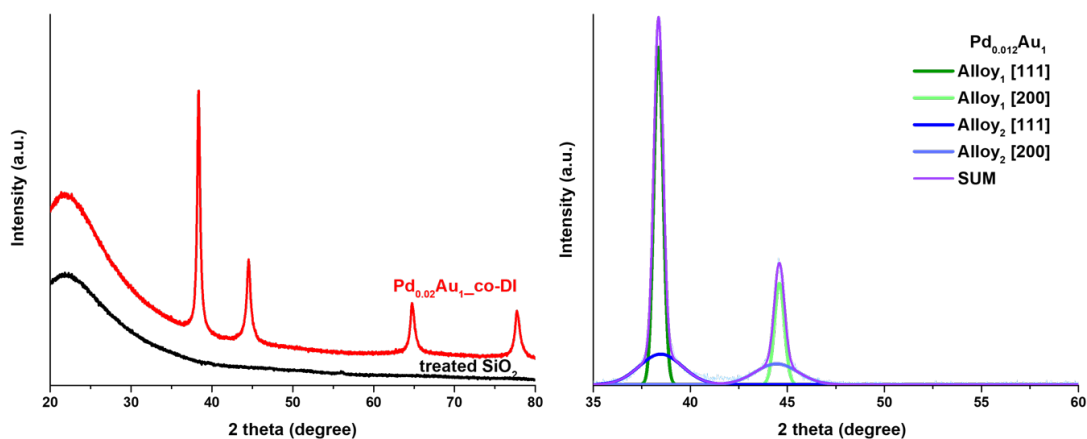


Figure 4.4 (a) Normalized XRD patterns for silica support and Pd<sub>0.02</sub>Au<sub>1</sub>\_co-DI; (b) Deconvolution of support background subtracted X-ray patterns of Pd<sub>0.02</sub>Au<sub>1</sub>\_co-DI

Table 4.2 XRD derived particle size, peak centers and Vegard's law derived peak centers.

Samples	D <sub>XRD</sub> (nm)	STEM		Bulk phase identified by XRD or STEM
		D <sub>V</sub> (nm)	D <sub>n</sub> (nm)	
Pd <sub>0.97</sub>	0.98	1.2	0.97	Pd <sub>2</sub> O
Pd <sub>1.27</sub> Au <sub>1</sub>	1.4	1.3*	1.1*	Bulk alloy, speckled
Pd <sub>0.227</sub> Au <sub>1</sub>	1.7	---	---	Bulk alloy
Pd <sub>0.08</sub> Au <sub>1</sub>	1.7	---	---	Bulk alloy
Pd <sub>0.04</sub> Au <sub>1</sub>	1.7	2.1	1.5	Bulk alloy
Pd <sub>0.02</sub> Au <sub>1</sub>	1.7	---	---	Au
Pd <sub>0.012</sub> Au <sub>1</sub>	1.7	---	---	Au
Pd <sub>0.01</sub> Au <sub>1</sub>	1.8	---	---	Au
Au <sub>1</sub>	1.7	2.0	1.3	Au

\*: SETM estimated over Pd<sub>1</sub>Au<sub>1</sub> sample

Pulse CO chemisorption was employed to address the question of how much Pd was on the surface, versus the amount in the bulk. Results are shown in Table 4.3 and are reported as uptake per gram of catalyst and per gram of Pd. If all Pd were on the surface the uptake would be 9.4 mmol/g<sub>Pd</sub>. The Pd “dispersion” which in this case is the amount of Pd on the surface versus the amount of Pd in the bulk of the alloy phase, is seen to vary from about 54 % to about 33 %. From R. V. Hardeveld and F. Hartog analysis [170] based on the XRD-determined particle size, the ratios of total metal dispersion, or the number of Au + Pd surface atoms versus total atoms is listed in the rightmost column of the table. That Pd dispersion is similar to the total metal dispersion suggests that co-SEA leads to the formation of bulk alloying with little or no surface enrichment. Surface enrichment of Pd is not expected, at least in the absence of a reactant which can pull it to the surface, as the surface free energy of Pd (2.403 J/m<sup>2</sup>) is slightly higher than that of Au (1.626 J/m<sup>2</sup>) [171]. That the majority of the Pd goes into bulk alloying is consistent with the XRD data. Below 0.04:1 Pd: Au, while chemisorption indicates the absence of Pd from the nanoparticle surfaces, the amount of the Pd is too small to produce a measurable XRD peak shift.

Table 4.3 Pulse CO chemisorption over PdAu DLA catalyts.

Samples	Q <sub>CO</sub>	Q <sub>Pd</sub>	Pd dispersion	N <sub>s</sub> /N <sub>T</sub>
	cm <sup>3</sup> /g <sub>cat.</sub>	μmol/g <sub>Pd</sub>	%	%
Pd <sub>1.27</sub> Au <sub>1</sub>	0.809	5.1	54	48
Pd <sub>0.227</sub> Au <sub>1</sub>	0.211	4.3	46	38
Pd <sub>0.08</sub> Au <sub>1</sub>	0.067	3.3	36	38
Pd <sub>0.04</sub> Au <sub>1</sub>	0.043	3.9	41	39
Pd <sub>0.02</sub> Au <sub>1</sub>	0.017	3.1	33	39

To gain further insight into the particle size and morphology, electron microscopy analysis was performed on mono/bimetallic PdAu catalysts. Representative STEM images (Fig. 4.5) revealed regular spherical particles with tight size distributions. Particle size estimates from STEM (volume averages) were largely consistent with XRD estimates as given in Table 4.2. Under the electron beam, the pure Pd oxides would be reduced, so the size reported is assumed to be reduced and not oxidized metal.

Careful inspection of high magnification images of the Pd<sub>1</sub>Au<sub>1</sub> sample (Fig. 4.5c) reveal speckled nanoparticles indicative of well-mixed alloys [172]. This effect is not seen (and is not expected to be seen) at low Pd:Au ratios. To further investigate the isolation of a minority metal, PdAu nanoparticles with inversed atomic Pd/Au ratios (1:0.04) were produced via the same synthetic procedure of co-SEA on oxidized carbon and the microscopy images are presented in Fig. 4.6. The clear occurrence of isolated, brighter Au atoms speckled throughout the dimmer Pd nanoparticles (in yellow circles) supports the hypothesis that electrostatic adsorption is an efficient methodology to attain DLAs through atomically distributing one minority element into another host metal atoms.

X-ray photoelectron spectroscopy (XPS) analysis was conducted after *in-situ* reduction to understand the electronic properties and surface composition. XPS Au4f and Pd3d, Au4d core level spectra with deconvolution by using two contributions originating from Pd<sup>0</sup> and Au<sup>0</sup> are given in Fig. 4.7. Assignments of resolved XPS spectra and the derived chemical composition was listed in Table 4.4. Au4f<sub>7/2</sub> and Au4d<sub>5/2</sub> peaks were detected on monometallic gold sample at binding energy (B.E.) of 84.3 eV and 334.7 eV, respectively, in close agreement to reported values [173]. The obtained binding energy of Pd<sup>0</sup> counterpart over Pd<sub>1</sub> was located at 335.4 eV and 340.1 eV for Pd3d<sub>5/2</sub> and Pd3d<sub>3/2</sub>,



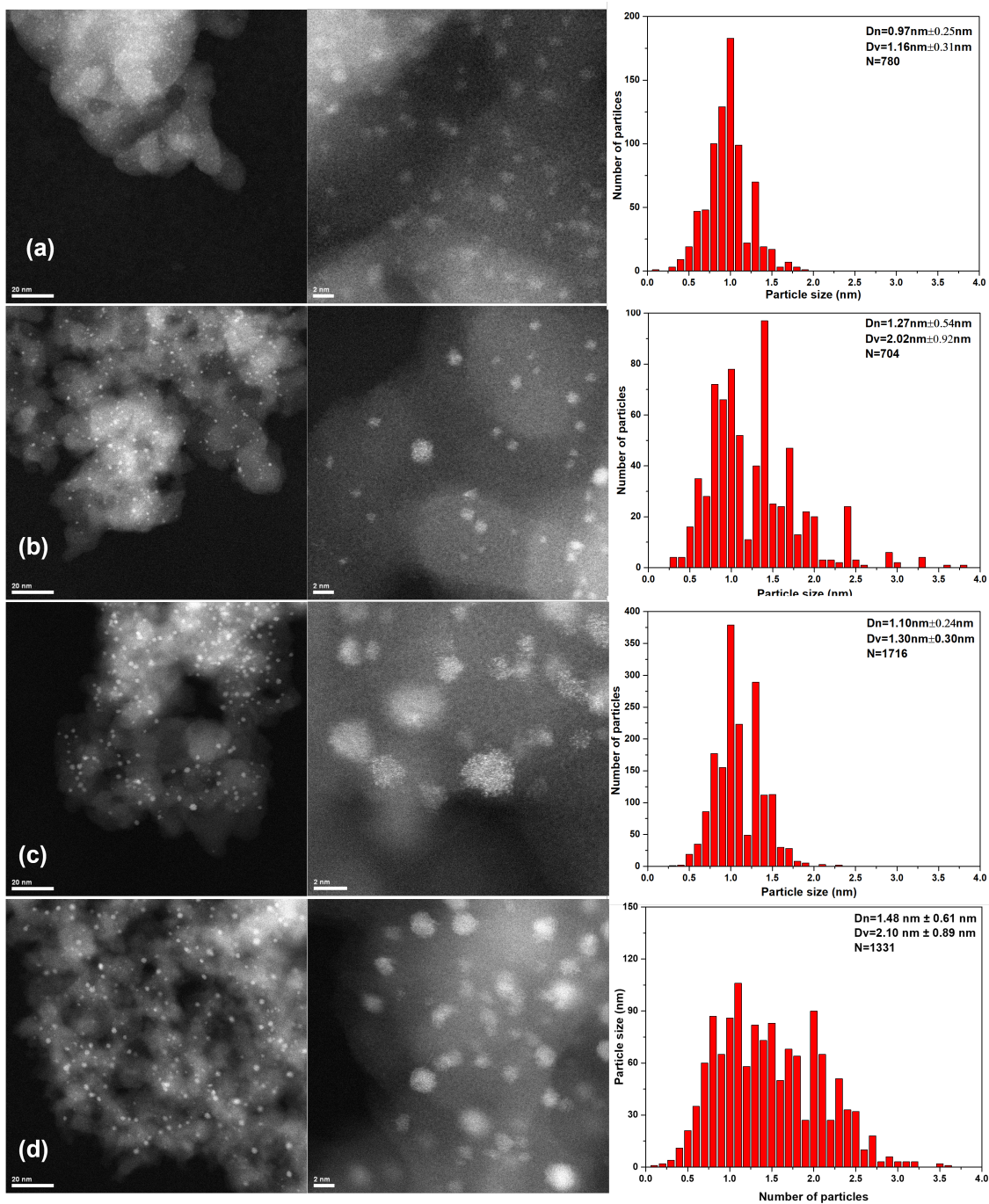


Figure 4.5 STEM images of monometallic Pd<sub>1</sub>\_SEA (A), Au<sub>1</sub>\_SEA (B), Pd<sub>1</sub>Au<sub>1</sub>\_co-SEA (C) and Pd<sub>0.04</sub>Au<sub>1</sub>\_co-SEA (D) catalyst at low and high magnification as well as the particle size distribution histograms.

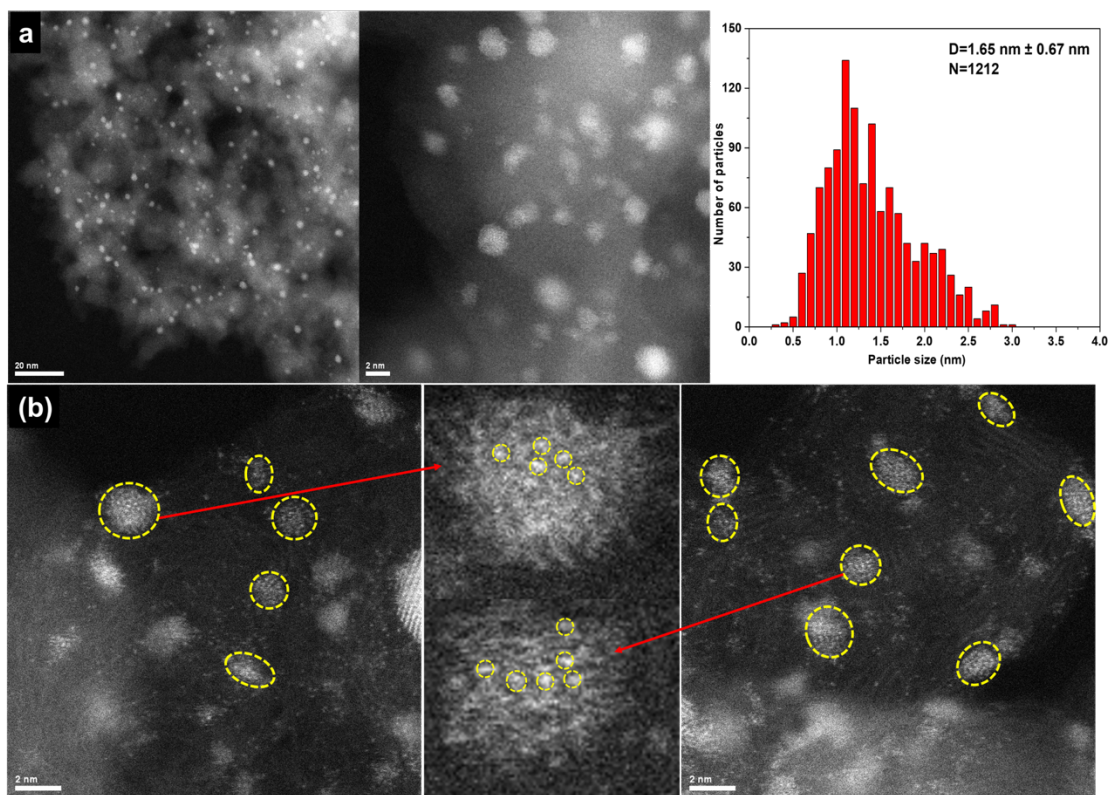


Figure 4.6 STEM images of monometallic Pd<sub>0.04</sub>Au<sub>1</sub>/A300\_co-SEA and Pd<sub>1</sub>Au<sub>0.04</sub> catalyst on carbon synthesized by co-SEA.

respectively, and the observed higher binding energy can be attributed to the small particles [174]. In PdAu DLA catalysts, with Pd dispersed in Au nanoparticles, Pd3d and Au4f binding energies moved in the opposite directions, with Au4f<sub>7/2</sub> going down from 84.3 eV for pure Au to 83.4 eV in the Pd<sub>1.27</sub>Au<sub>1</sub> alloy and Pd3d<sub>5/2</sub> going up from 335.3 eV for pure Pd to 335.6 eV as it was diluted. These shifts evidence charge transfer from Pd to Au in the alloys due to a higher electronegativity of Au. Liu and colleagues [158] also detected charge transfer between Pd and Au on their carbon-supported PdAu alloys with trace amount of Pd (0.4 at.%).

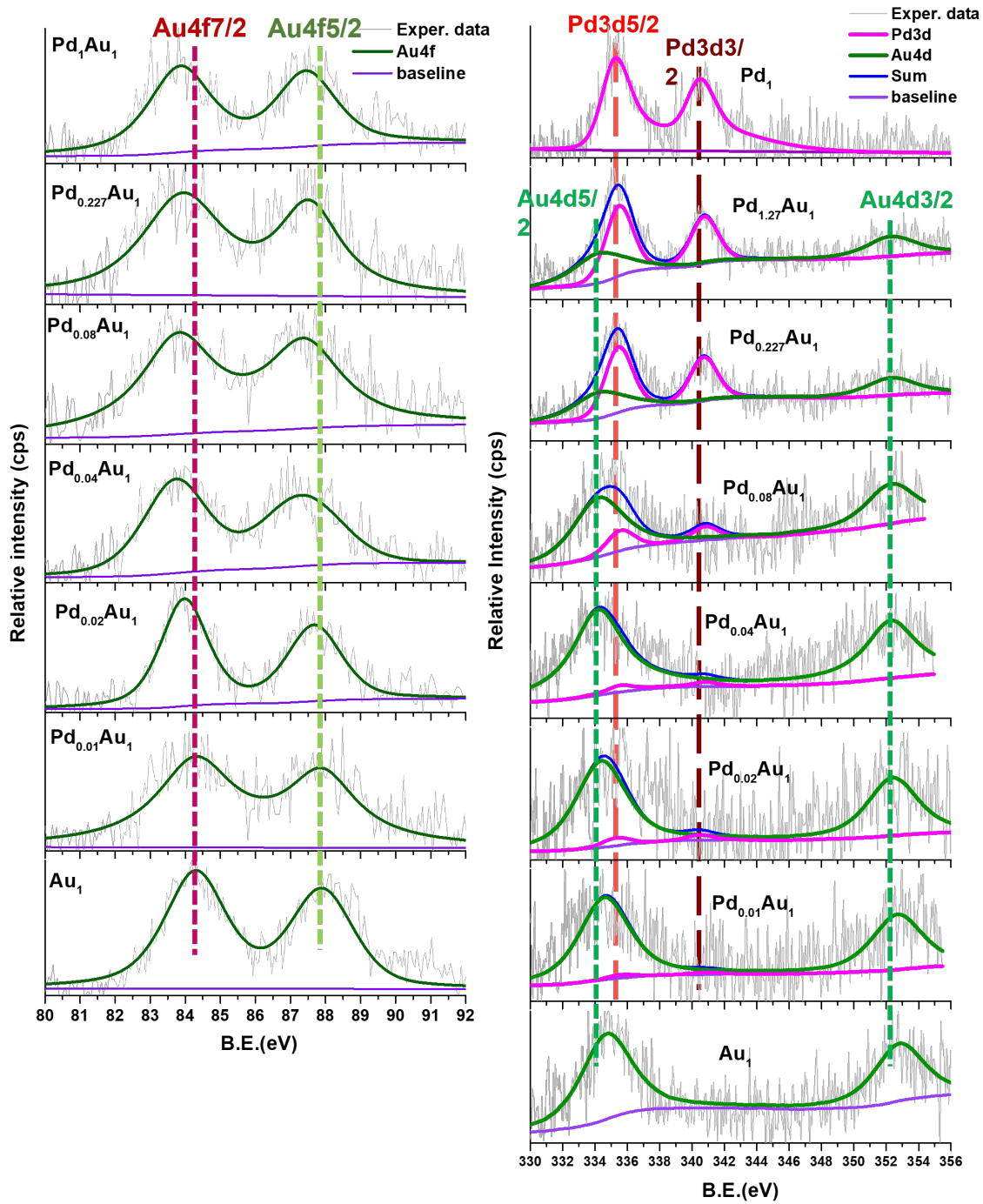


Figure 4.7 XPS spectra comparison of Au4f (a), Pd3d and Au3d (b) over PdAu DLA catalysts.

Table 4.4 Binding energy of Au4f, Pd3d, Au4d, and surface composition derived by XPS spectra.

Samples	Binding Energy (eV)		
	Au4f <sub>7/2</sub>	Pd3d <sub>5/2</sub>	Au4d <sub>5/2</sub>
<b>Pd<sub>0.98</sub></b>	---	335.3	---
<b>Pd<sub>1</sub>Au<sub>1</sub>_co-SEA</b>	83.8	335.5	334.2
<b>Pd<sub>0.227</sub>Au<sub>1</sub>_co-SEA</b>	83.8	335.6	334.2
<b>Pd<sub>0.08</sub>Au<sub>1</sub>_co-SEA</b>	83.8	335.6	334.2
<b>Pd<sub>0.04</sub>Au<sub>1</sub>_co-SEA</b>	83.8		334.2
<b>Pd<sub>0.02</sub>Au<sub>1</sub>_co-SEA</b>	84.0	weak Pd signal	334.4
<b>Pd<sub>0.01</sub>Au<sub>1</sub>_co-SEA</b>	84.3		334.6
<b>Au<sub>2.2</sub></b>	84.3	---	334.7

The characterization to this point indicates that the co-SEA yields well alloyed PdAu nanoparticles with, at the dilute limit, about thirty-five to forty percent of the Pd atoms at the surface, and also that the Pd and Au are in close enough proximity to allow electron transfer. A final characterization is the use of CO-FTIR to determine to what extent the surface Pd is isolated or exists as ensembles.

The PdAu DLA system is an ideal system to characterize Pd site isolation by CO-FTIR; the matrix of Au will not adsorb CO in appreciable amounts, and Pd in ultrasmall nanoparticles adsorb CO mostly in bridged and hollow sites [175, 176]. Thus the disappearance of bridged and hollow-adsorbed CO on Pd, which appears below 2000 cm<sup>-1</sup> [177, 178], with the persistence of linear-adsorbed CO (bands above 2000 cm<sup>-1</sup>), without any interference from CO adsorption on the second metal, is a sensitive probe of Pd site isolation [177]. The procedure for collecting spectra over an equilibrated surface is illustrated in Fig. 4.8 for the Pd<sub>1.27</sub>Au<sub>1</sub> catalyst. Flowing 1% CO in argon for 30 minutes caused a gradual increase in the adsorbed CO bands (gas phase removed for clarity in Fig.

4.8a) and afterwards, CO is removed from the gas stream and the adsorbed species re-equilibrate (Fig. 4.8b and d). After purging CO from the gas phase, the linear CO peaks decreased a bit while the bridged and hollow-bound CO peaks remained relatively constant. These spectra were acquired with an in-situ reduction of 180 °C (instead of 400 °C) which completely eliminated the uptake of CO onto Au. The final equilibrated spectrum of this and all the other samples comprise Figure 4.9.

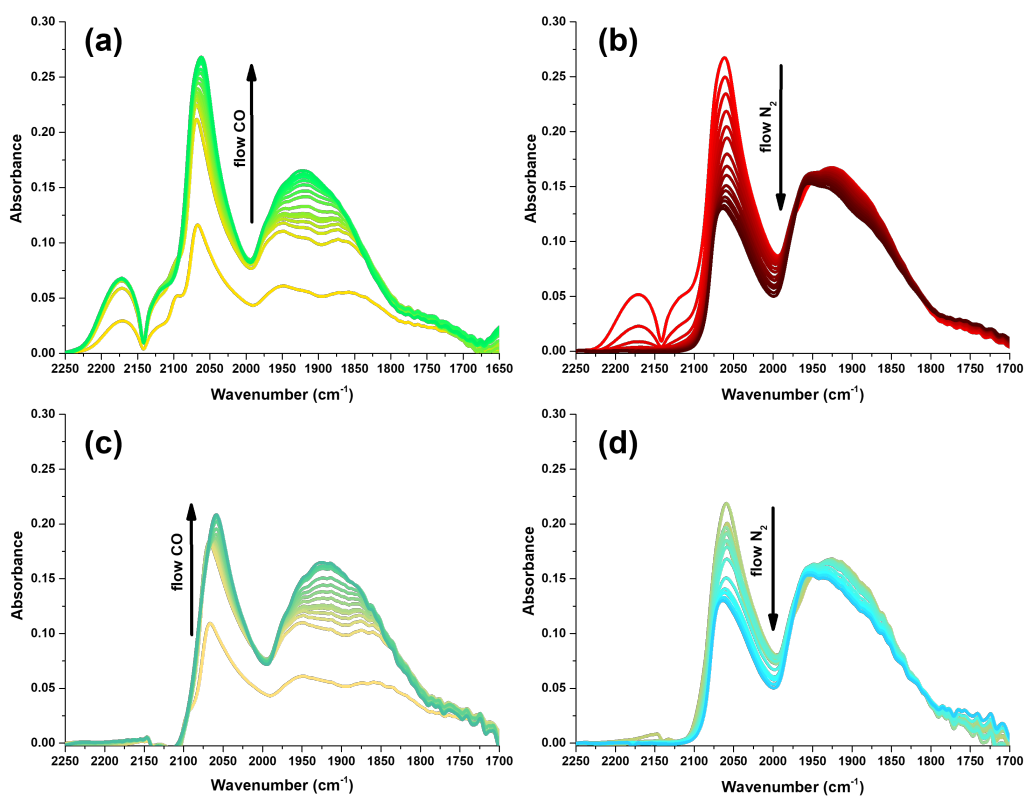


Figure 4.8 Time-dependent FTIR spectra over Pd<sub>1.27</sub>Au<sub>1</sub> (a) in 1% CO/Ar and (b) in the subsequent N<sub>2</sub> flow; (c-d) subtracted IR spectra on Au<sub>2.2</sub>.

The CO-FTIR spectra of the series of single metal and bimetallic catalysts, following the 180 °C in-situ reduction (which followed a prior 400 °C reduction and handling in air to press the IR discs) is shown in Fig. 4.9. The pure Au is shown in the

bottom spectrum, and pure Pd samples are shown in the top two spectra. No CO was observed on the monometallic Au catalyst following the lower temperature reduction. Besides the monometallic Pd<sub>0.97</sub> sample, another Pd-only sample was made, specifically for the IR study, with a lower Pd loading more representative of the Pd loadings in the DLA catalysts. The SEA-derived 0.10 wt% Pd sample corresponds to the amount of Pd present in the Pd<sub>0.08</sub>Au<sub>1</sub> sample. Both of these samples show a set of linear adsorption peaks above 2000 cm<sup>-1</sup> and a set of multiply-bonded peaks below 2000 cm<sup>-1</sup>. Gaussian fitting revealed for both samples the three characteristic linearly adsorbed CO bands (L1, L2, L3) in the regime of 2100-2000 cm<sup>-1</sup>, centering around 2088 cm<sup>-1</sup>, 2072 cm<sup>-1</sup> and 2040 cm<sup>-1</sup>, which can be ascribed to linear carbonyls on terrace, edges and kinks sites on Pd [111] and [200] facets [18, 177, 179, 180]. The bridged CO stretching region with lower frequency [181] can be curve fit with peaks at around 1965 cm<sup>-1</sup> (B1) and 1890 cm<sup>-1</sup> (B2), ascribed CO bridge-bonded to pairs of Pd atoms on [111] and [200] facets [145, 182]. In addition, another two stretching bands at 1850 cm<sup>-1</sup> (H1), and 1779 cm<sup>-1</sup>-1744 cm<sup>-1</sup> (H2), are required to finely fit the spectra due to CO bonded on three-fold hollow Pd sites on [111] and more open facets [145, 176]. The latter sites only appear on the higher loading Pd-only catalyst, perhaps from a larger particle size. Assignments of IR peaks were summarized in Table 4.5.

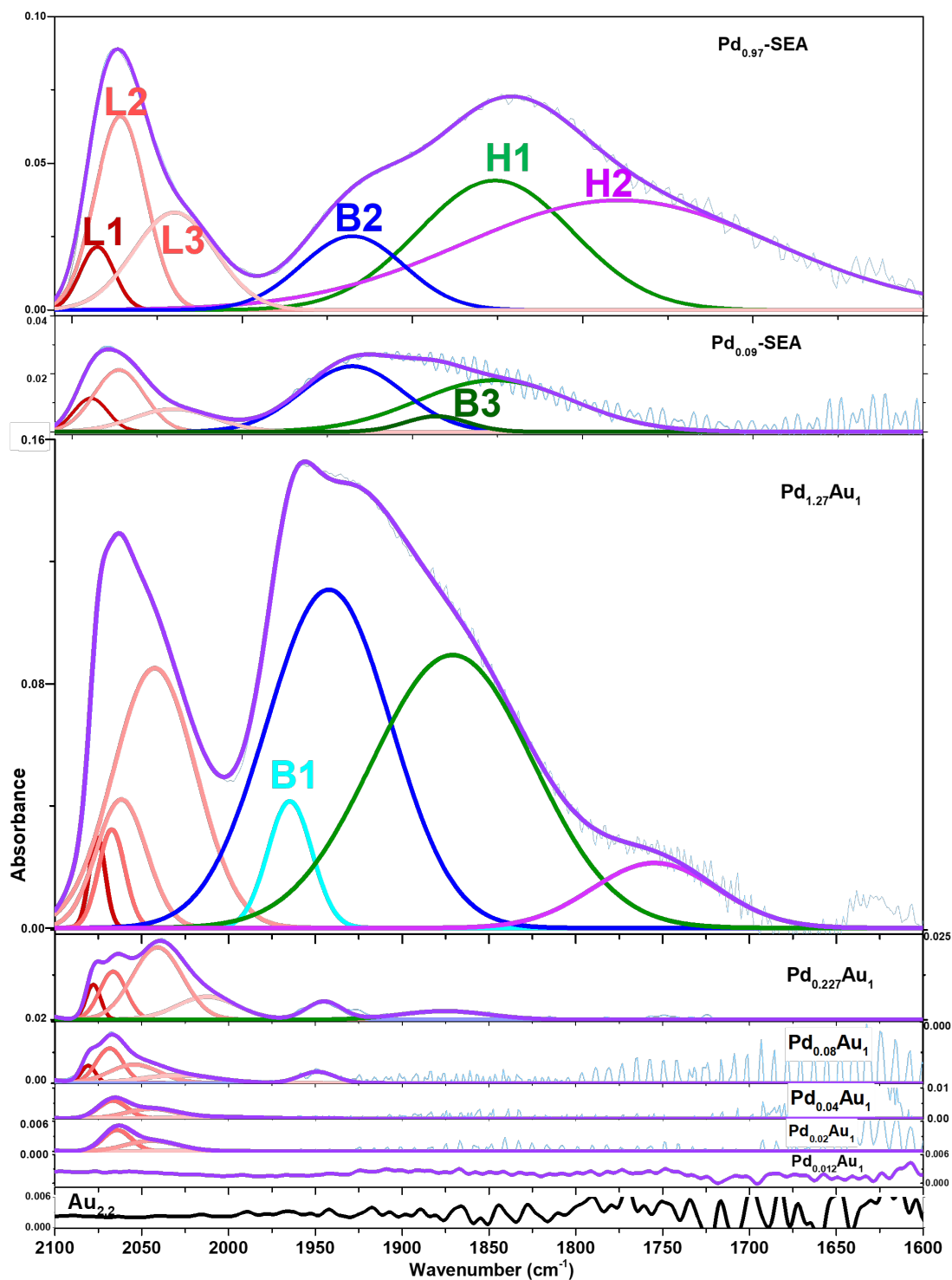


Figure 4.9 IR spectra over (a) monometallic and (b) PdAu DLA catalysts.

Table 4.5 Assignments of CO adsorption on Pd sites over monometallic and PdAu DLA catalysts.

Samples	Linear-CO on Pd (cm <sup>-1</sup> )			bridged CO on Pd (cm <sup>-1</sup> )			3-hollow CO (cm <sup>-1</sup> )		Linear CO fraction (%)
	L1, L1'	L2	L3	B1	B2	B3	H1	H2	
Pd <sub>0.97</sub> _SEA	2085	2071	2040	---	1935	---	1851	1779	24
Pd <sub>0.10</sub> _SEA	2089	2072	2040	---	1935	1886	1851	---	28
Pd <sub>1.27</sub> Au <sub>1</sub> _co-SEA	2075 2063	2047	---	1966	1936	1896	---	1744	25
Pd <sub>0.23</sub> Au <sub>1</sub> _co-SEA	2078 2063	2040	2019	1946	---	---	---	---	81
Pd <sub>0.08</sub> Au <sub>1</sub> _co-SEA	2080 2063	2040	2022	1948	---	---	---	---	88
Pd <sub>0.04</sub> Au <sub>1</sub> _co-SEA	2063	2045	2013	---	---	---	---	---	100
Pd <sub>0.02</sub> Au <sub>1</sub> _co-SEA	2063	2042	2017	---	---	---	---	---	100
reference	2069 [140] 2065 [177, 183]	2078 [145]		1950 [140, 177, 183]	1940 [180]	1900 [180]	1859 [183] 1820 [183] 180 [180]	1755 [183]	

\*: CO bands in the blue rectangles correspond to the cartoon figures in the blue rectangles.

Both Pd-only catalysts show a majority of bridge or hollow-bound CO, and with about the same fraction (24 - 28 %) of linear species. Interestingly, the high Pd loading (Pd<sub>1.27</sub>Au<sub>1</sub>) sample also shows a high percentage of nonlinear sites, with an abundance of bridged sites and a decrease of hollow sites compared to the Pd-only catalysts. Curve fitting the linear carbonyl region in this spectrum gives a new CO band at 2063 cm<sup>-1</sup>, which can be ascribed to linearly bonded-CO on isolated Pd sites associated with Au [140, 177, 183]. The red shift of 7 - 30 cm<sup>-1</sup> in linear carbonyl frequency might be interpreted by two factors: less competition in the anti-bonding  $\pi$ -back-donation from Au than Pd [183]; or weakened dipole-dipole coupling because of the decreased amount of CO molecules adsorbed on the diluted Pd sites [140, 183, 184]. The red shifts of the multi-adsorption IR peaks could be also explained by the effects of the alloys and/or CO coupling.



Starting with the Pd<sub>0.227</sub>Au<sub>1</sub> sample, the intensity of the bridge and hollow-bound peaks diminishes rapidly until they disappear completely at the 0.04:1 ratio. An analysis based on the area of IR-spectra resolved peaks can be used to quantify the fraction of isolated Pd on Au surface [28, 175]; a comparison of the ratios of linear peak intensity to total intensity is shown in Fig. 4.10. While the Pd-rich sample (Pd<sub>1.27</sub>Au<sub>1</sub>) shows about the same ratio of linear species as the Pd-only samples, the percentage of linear species raises rapidly in the lower loading samples and appears to be 100 % at or below 0.04:1 Pd:Au. As about 60 % of the Pd in that sample is alloyed in the bulk and not on the surface (Table 4.3), the effective surface ratio of Pd is 0.016:1, or about 1 Pd:63 Au. Per the Hartog/van Hardeveld relation [170], a 1.7 nm nanoparticle contains about 120 atoms, and at 0.04:1 Pd, Au, it would contain about 5 atoms of Pd, of which about 2 would exist at the surface. Lower Pd/Au ratios would contain correspondingly lower numbers of total and surface Pd per nanoparticle.

The density of isolated surface sites of Pd in the gold matrix, obtained by this simple synthesis, is reasonably high. Filie and the co-workers [185] used a colloidal preparation of bimetallic nanoparticles and noted a dual-site mechanism over their dilute Pd-in-Au alloys on SiO<sub>2</sub> at 1:50 Pd:Au due to the presence of both clustered and isolated Pd sites, suggesting partial isolation of surface Pd atoms. Ricciardulli et al. [186] synthesized catalysts with a sequence of SEA of Au ethylenediamine followed by electroless deposition of Pd, and reported the initial isolation of Pd at a Au/Pd ratio 37, although bridged CO did appear in this and a 50:1 sample after prolonged annealing in CO at 100 °C. Both of these works employed nanoparticles of larger size, about 6 and 7 nm, respectively, than the 1.7 nm particles produced here via co-SEA.

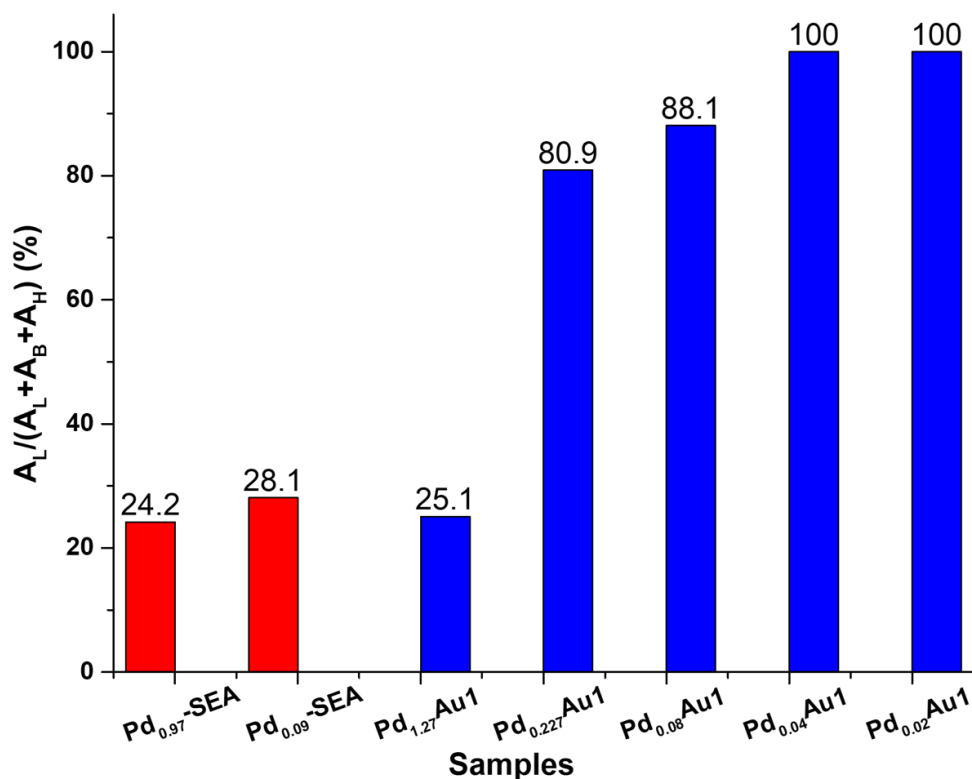


Figure 4.10 FTIR derived fraction of linearly adsorbed CO.

#### 4.5.2 Partial Oxidation Reaction of 1-Phenylethanol

The probe reaction chosen to test the effect of isolated Pd in a Au matrix was the partial oxidation (or dehydrogenation) of 1-phenylethanol to acetophenone. The oxidation of alcohols is an important class of catalytic processes to obtain value-added fine chemicals [187]. For this reaction the support has been shown to have a substantial effect on the reactivity, and silica has the lowest activity. Therefore, the effect of Pd isolation in Au should appear most prominently over this support. As high temperatures can catalyze the cleavage of C-C bond in the alcohol and lead to a low selectivity to the desired aldehyde [183, 188] a low temperature at 160 °C was employed. At this temperature and with 50 psig oxygen, selectivity to acetophenone was 100%.

Figure 4.11 are plotted results from a series of catalysts for which the mass of catalyst was adjusted to give the same number of total Pd sites, 64 mmol of Pd (except for the Au-only catalyst, which contained 64 mmol of Au.) Both pure metals exhibited low activity. Placing the same amount of Pd into the Au lattice at the ratio of 0.227:1 gave a much more active catalyst and diluting the Pd even further to 0.08:1 increased the activity even more. Due to the low amounts of Pd in the remainder of the series, runs with the remaining DLA catalysts could not be conducted with a constant amount of Pd. Measured rates for those catalysts were converted to turnover frequency (based on total Pd) and plotted along with the rest of the samples in Figure 4.11b. This plot reveals a striking change in turnover frequency of four orders of magnitude as the Pd is isolated into the Au matrix, with the samples shown by IR to be totally isolated (0.04 and lower) to be the most active by 1 to 2 orders of magnitude over catalysts showing small ensembles of Pd (1:1 – 0.08:1) and these in turn are almost two orders of magnitude higher in activity than pure Pd or Au. As the Pd dispersions of the DLA catalysts are about the same (Table 4.3) and are lower than the pure Pd (1 nm particles have about 100% dispersion), an alternate calculation of turnover frequency based on surface Pd would show the same trend, or in the case of pure Pd, an even greater difference in activity.

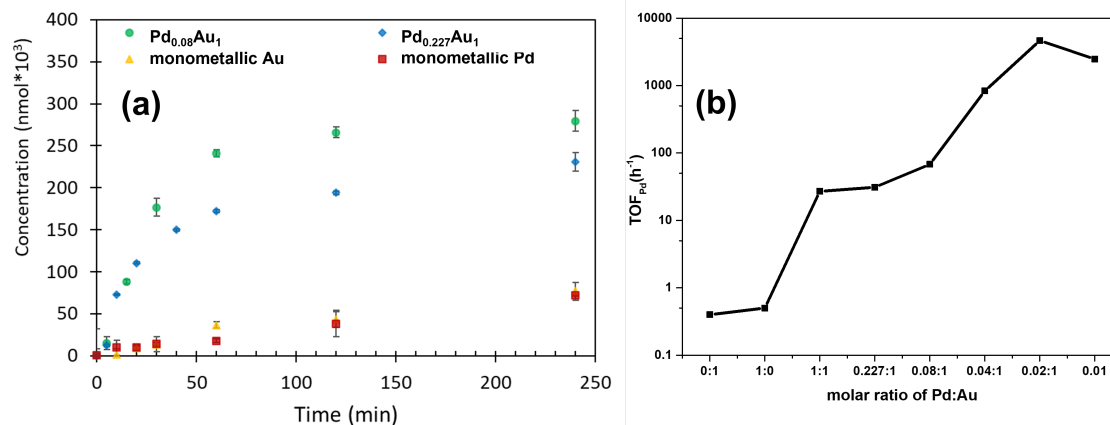


Figure 4.11 (a) Concentration of acetophenone per 0.64 mmol Pd vs reaction time; (b) turnover frequency based on Pd amount.

Li et al. [189] utilized DFT simulation and found that in the dehydrogenation of ethanol over isolated Pd atoms in a Au [111] surface, the activation barrier for  $\alpha$ -C-H cleavage is lower than O-H bond scission and the dissociated H atom migrates to the 3-fold hollow sites with one isolated Pd and two adjacent Au atomic ensemble, while  $\beta$ -C-H mainly adsorbed on Au sites with high energy barrier. That interpretation is not inconsistent with the current results. That the 0.227:1 and the 0.08:1 Pd:Au catalysts are up to two orders of magnitude less active than the lower Pd/Au ratios, even though there is relatively little multiply-bound CO (Fig. 4.9 and 4.10) in these catalysts, suggests that the main increase in activity stems from an electronic effect of isolated Pd atoms; surrounding the Pd with more Au helps. The charge transfer observed here from Pd to Au in the alloys has been shown to facilitate the generation of gold anions which can easily adsorb O<sub>2</sub> [190]. It is perhaps in the more dilute samples that this local environment is optimized.

## 4.5 Conclusion

Dilute Pd-in-Au homogenous alloys with ultra-small nanoparticles can be readily synthesized via simultaneous electrostatic adsorption. The ratio of metals is easily controlled using the concentration of the metal precursors in the impregnating solution. The nanoparticles generated from this synthesis appear to be largely alloyed, with the fraction of Pd on the surface about equal to the total metal dispersion. Pd atoms appear to become completely isolated at or below a Pd:Au ratio of 0.04:1 or 1:25, with 35 to 40% of these being present at the surface and available for reaction. The turnover frequencies for 1-phenyl ethanol dehydrogenation to acetophenone of the DLA series varied over four orders of magnitude as the Pd atoms were successively diluted in a Au matrix.

## REFERENCES

1. Poovan, F., et al., *Synergy between homogeneous and heterogeneous catalysis*. Catalysis Science & Technology, 2022.
2. Fechete, I., Y. Wang, and J.C. Védrine, *The past, present and future of heterogeneous catalysis*. Catalysis Today, 2012. **189**(1): p. 2-27.
3. Schlogl, R., *Heterogeneous catalysis*. Angew Chem Int Ed Engl, 2015. **54**(11): p. 3465-520.
4. Daniel, R.M. and M.J. Danson, *A new understanding of how temperature affects the catalytic activity of enzymes*. Trends Biochem Sci, 2010. **35**(10): p. 584-91.
5. Zaera, F., *Designing Sites in Heterogeneous Catalysis: Are We Reaching Selectivities Competitive With Those of Homogeneous Catalysts?* Chem Rev, 2022. **122**(9): p. 8594-8757.
6. Sapi, A., et al., *Metallic Nanoparticles in Heterogeneous Catalysis*. Catalysis Letters, 2021. **151**(8): p. 2153-2175.
7. Liu, L. and A. Corma, *Metal Catalysts for Heterogeneous Catalysis: From Single Atoms to Nanoclusters and Nanoparticles*. Chem Rev, 2018. **118**(10): p. 4981-5079.
8. Singh, A.K. and Q. Xu, *Synergistic Catalysis over Bimetallic Alloy Nanoparticles*. ChemCatChem, 2013. **5**(3): p. 652-676.
9. Yan, Y., et al., *Intermetallic Nanocrystals: Syntheses and Catalytic Applications*. Adv Mater, 2017. **29**(14).
10. Liu, X.Y., et al., *Catalysis by gold: New insights into the support effect*. Nano Today, 2013. **8**(4): p. 403-416.
11. Tom W. van Deelen, C.H.M., and Krijn P. de Jong, *Control of metal-support interactions in heterogeneous catalysts to enhance activity and selectivity*. Nature Catalysis, 2019. **2**(11): p. 955-970.
12. Shahinuzzaman, M., Z. Yaakob, and Y. Ahmed, *Non-sulphide zeolite catalyst for bio-jet-fuel conversion*. Renewable and Sustainable Energy Reviews, 2017. **77**: p. 1375-1384.

13. Bokov, D., et al., *Nanomaterial by Sol-Gel Method: Synthesis and Application*. Advances in Materials Science and Engineering, 2021. **2021**: p. 1-21.
14. Esposito, S., *"Traditional" Sol-Gel Chemistry as a Powerful Tool for the Preparation of Supported Metal and Metal Oxide Catalysts*. Materials (Basel), 2019. **12**(4).
15. Li, Y., et al., *Porous materials confining noble metals for the catalytic reduction of nitroaromatics: controllable synthesis and enhanced mechanism*. Environmental Science: Nano, 2021. **8**(11): p. 3067-3097.
16. Kesavan, G., et al., *Hydrothermal synthesis of NiFe<sub>2</sub>O<sub>4</sub> nanoparticles as an efficient electrocatalyst for the electrochemical detection of bisphenol A*. New Journal of Chemistry, 2020. **44**(19): p. 7698-7707.
17. Lahiri, A., G. Pulletikurthi, and F. Endres, *A Review on the Electroless Deposition of Functional Materials in Ionic Liquids for Batteries and Catalysis*. Front Chem, 2019. **7**: p. 85.
18. Rebelli, J., et al., *Synthesis and characterization of Au–Pd/SiO<sub>2</sub> bimetallic catalysts prepared by electroless deposition*. Journal of Catalysis, 2010. **270**(2): p. 224-233.
19. Hadjiivanov, K., *Identification and Characterization of Surface Hydroxyl Groups by Infrared Spectroscopy*, in *IR Identification and Characterization of Surface Hydroxyl Groups*. 2014. p. 99-318.
20. Regalbuto, J.P.a.J.R., *A simple accurate determination of oxide PZC and the strong buffering effect of oxide surface at incipient wetness*. Journal of Colloid and Interface Science, 1995. **175**: p. 239-252.
21. N. Santhanam, T.A.C., W. Spieker, J.R. Regalbuto\*, *Nature of metal catalyst precursors adsorbed onto oxide supports*. Catalysis Today 1994. **21**: p. 141-156.
22. Hao, X., W.A. Spieker, and J.R. Regalbuto, *A further simplification of the revised physical adsorption (RPA) model*. Journal of Colloid and Interface Science, 2003. **267**(2): p. 259-264.
23. Hao, X., S. Barnes, and J.R. Regalbuto, *A fundamental study of Pt impregnation of carbon: Adsorption equilibrium and particle synthesis*. Journal of Catalysis, 2011. **279**(1): p. 48-65.
24. Regalbuto\*, A.M.S.a.J.R., *Retardation of Pt Adsorption over Oxide Supports at pH Extremes: Oxide Dissolution or High Ionic Strength?* Langmuir 1994,10, 500-504, 1994.
25. Samad, J.E., et al., *The controlled synthesis of metal-acid bifunctional catalysts: The effect of metal:acid ratio and metal-acid proximity in Pt silica-alumina catalysts for n-heptane isomerization*. Journal of Catalysis, 2016. **342**: p. 203-212.

26. A. Wong, Q.L.,<sup>1</sup> S. Griffin,<sup>1</sup> A. Nicholls,<sup>2</sup> J. R. Regalbuto<sup>1</sup>, *Synthesis of ultrasmall, homogeneously alloyed, bimetallic nanoparticles on silica supports*. Science 2017. **358**, 1427–1430 (2017).
27. Wong, A.P., et al., *The catalytic behavior of precisely synthesized Pt–Pd bimetallic catalysts for use as diesel oxidation catalysts*. Catalysis Today, 2016. **267**: p. 145-156.
28. De Castro, L., et al., *Dilute Limit Alloy Pd–Cu Bimetallic Catalysts Prepared by Simultaneous Strong Electrostatic Adsorption: A Combined Infrared Spectroscopic and Density Functional Theory Investigation*. The Journal of Physical Chemistry C, 2022.
29. Ennaert, T., et al., *Potential and challenges of zeolite chemistry in the catalytic conversion of biomass*. Chem Soc Rev, 2016. **45**(3): p. 584-611.
30. Tan, Y., et al., *Species and impacts of metal sites over bifunctional catalyst on long chain n-alkane hydroisomerization: A review*. Applied Catalysis A: General, 2021. **611**.
31. Alonso, D.M., J.Q. Bond, and J.A. Dumesic, *Catalytic conversion of biomass to biofuels*. Green Chemistry, 2010. **12**(9).
32. Shen, Q., et al., *Breaking the activity limitation of iridium single-atom catalyst in hydrogenation of quinoline with synergistic nanoparticles catalysis*. Nano Research, 2022. **15**(6): p. 5024-5031.
33. Mao, J., et al., *Single atom alloy: An emerging atomic site material for catalytic applications*. Nano Today, 2020. **34**.
34. Demirbas, A., A. Bafail, and A.-S. Nizami, *Heavy oil upgrading: Unlocking the future fuel supply*. Petroleum Science and Technology, 2016. **34**(4): p. 303-308.
35. Baba, Y.D., et al., *Study of high viscous multiphase phase flow in a horizontal pipe*. Heat and Mass Transfer, 2017. **54**(3): p. 651-669.
36. Lian, X., et al., *Progress on upgrading methods of bio-oil: A review*. International Journal of Energy Research, 2017. **41**(13): p. 1798-1816.
37. Zhao, F., et al., *A review on upgrading and viscosity reduction of heavy oil and bitumen by underground catalytic cracking*. Energy Reports, 2021. **7**: p. 4249-4272.
38. Zhang, M., et al., *A review of bio-oil upgrading by catalytic hydrotreatment: Advances, challenges, and prospects*. Molecular Catalysis, 2021. **504**.
39. Xuening Li<sup>1</sup>, F.Z.a.G.L., *Review on new heavy oil viscosity reduction technologies*. Earth and Environmental Science. **983** (2022) **012059**.



40. Baloch, H.A., et al., *Recent advances in production and upgrading of bio-oil from biomass: A critical overview*. Journal of Environmental Chemical Engineering, 2018. **6**(4): p. 5101-5118.
41. Park, Y.-K., et al., *Bio-oil upgrading through hydrogen transfer reactions in supercritical solvents*. Chemical Engineering Journal, 2021. **404**.
42. Wang, X., et al., *Hydrodeoxygenation of lignin-derived phenolics – a review on the active sites of supported metal catalysts*. Green Chemistry, 2020. **22**(23): p. 8140-8168.
43. Si, Z., et al., *An Overview on Catalytic Hydrodeoxygenation of Pyrolysis Oil and Its Model Compounds*. Catalysts, 2017. **7**(6).
44. Qu, L., et al., *A review of hydrodeoxygenation of bio-oil: model compounds, catalysts, and equipment*. Green Chemistry, 2021. **23**(23): p. 9348-9376.
45. Patel, M. and A. Kumar, *Production of renewable diesel through the hydroprocessing of lignocellulosic biomass-derived bio-oil: A review*. Renewable and Sustainable Energy Reviews, 2016. **58**: p. 1293-1307.
46. Xiao, Y., et al., *Guaiacol Hydrodeoxygenation and Hydrogenation over Bimetallic Pt-M (Nb, W, Zr)/KIT-6 Catalysts with Tunable Acidity*. ACS Sustainable Chemistry & Engineering, 2022. **10**(15): p. 4831-4838.
47. Kim, S., et al., *Recent advances in hydrodeoxygenation of biomass-derived oxygenates over heterogeneous catalysts*. Green Chemistry, 2019. **21**(14): p. 3715-3743.
48. Luo, B., et al., *Boric Acid as a Novel Homogeneous Catalyst Coupled with Ru/C for Hydrodeoxygenation of Phenolic Compounds and Raw Lignin Oil*. Industrial & Engineering Chemistry Research, 2020. **59**(39): p. 17192-17199.
49. R. Gallo, J.M. and M. A. Trapp, *The Chemical Conversion of Biomass-Derived Saccharides: an Overview*. Journal of the Brazilian Chemical Society, 2017.
50. Robinson, A.M., J.E. Hensley, and J.W. Medlin, *Bifunctional Catalysts for Upgrading of Biomass-Derived Oxygenates: A Review*. ACS Catalysis, 2016. **6**(8): p. 5026-5043.
51. Zhang, H., et al., *Advances in production of bio-based ester fuels with heterogeneous bifunctional catalysts*. Renewable and Sustainable Energy Reviews, 2019. **114**.
52. Yan, P., et al., *The role of acid and metal sites in hydrodeoxygenation of guaiacol over Ni/Beta catalysts*. Catalysis Science & Technology, 2020. **10**(3): p. 810-825.

53. Lee, C.R., et al., *Catalytic roles of metals and supports on hydrodeoxygenation of lignin monomer guaiacol*. *Catalysis Communications*, 2012. **17**: p. 54-58.
54. Lee, H., et al., *Catalytic Hydrodeoxygenation of Bio-oil Model Compounds over Pt/HY Catalyst*. *Sci Rep*, 2016. **6**: p. 28765.
55. Martínez Figueredo, K.G., et al., *Production of pentyl valerate from  $\gamma$ -valerolactone, pentanol and H<sub>2</sub> using Pd and Rh-based bifunctional catalysts*. *Reaction Chemistry & Engineering*, 2022.
56. Kim, H., et al., *Upgrading bio-oil model compound over bifunctional Ru/HZSM-5 catalysts in biphasic system: Complete hydrodeoxygenation of vanillin*. *J Hazard Mater*, 2022. **423**(Pt A): p. 126525.
57. Wang, Y., et al., *Guaiacol hydrodeoxygenation over Pd catalyst with mesoporous ZSM-5 support synthesized by solid-state crystallization*. *Catalysis Today*, 2020. **358**: p. 60-67.
58. Ramanathan, A., et al., *Direct incorporation of tungsten into ultra-large-pore three-dimensional mesoporous silicate framework: W-KIT-6*. *Journal of Porous Materials*, 2012. **19**(6): p. 961-968.
59. Ramanathan, A., et al., *Novel zirconium containing cage type silicate (Zr-KIT-5): An efficient Friedel–Crafts alkylation catalyst*. *Chemical Engineering Journal*, 2015. **278**: p. 113-121.
60. Wang, X., et al., *Low temperature hydrodeoxygenation of guaiacol into cyclohexane over Ni/SiO<sub>2</sub> catalyst combined with Hbeta zeolite*. *RSC Adv*, 2019. **9**(7): p. 3868-3876.
61. Ramanathan, A., et al., *Niobium incorporated mesoporous silicate, Nb-KIT-6: Synthesis and characterization*. *Microporous and Mesoporous Materials*, 2014. **190**: p. 240-247.
62. Karanwal, N., et al., *One-pot direct conversion of levulinic acid into high-yield valeric acid over a highly stable bimetallic Nb-Cu/Zr-doped porous silica catalyst*. *Green Chemistry*, 2020. **22**(3): p. 766-787.
63. Jystad, A.M., A. Biancardi, and M. Caricato, *Simulations of Ammonia Adsorption for the Characterization of Acid Sites in Metal-Doped Amorphous Silicates*. *The Journal of Physical Chemistry C*, 2017. **121**(40): p. 22258-22267.
64. Ramanathan, A., et al., *Tungsten-incorporated cage-type mesoporous silicate: W-KIT-5*. *Microporous and Mesoporous Materials*, 2013. **175**: p. 43-49.
65. Ramanathan, A., et al., *Synthesis and characterization of Zirconium incorporated ultra large pore mesoporous silicate, Zr-KIT-6*. *Microporous and Mesoporous Materials*, 2013. **167**: p. 207-212.

66. Biffis, A., et al., *Pd Metal Catalysts for Cross-Couplings and Related Reactions in the 21st Century: A Critical Review*. Chem Rev, 2018. **118**(4): p. 2249-2295.
67. Bahmanpour, A.M., M. Signorile, and O. Kröcher, *Recent progress in syngas production via catalytic CO<sub>2</sub> hydrogenation reaction*. Applied Catalysis B: Environmental, 2021. **295**.
68. Monai, M., et al., *Catalytic Oxidation of Methane: Pd and Beyond*. European Journal of Inorganic Chemistry, 2018. **2018**(25): p. 2884-2893.
69. HUI ZHANG, M.J., ‡ YUJIE XIONG, ^ BYUNGKWON LIM, # AND YOUNAN XIA, *Shape-Controlled Synthesis of Pd Nanocrystals and Their Catalytic Applications*. ACCOUNTS OF CHEMICAL RESEARCH 2013. Vol. **46**, No. **8** (2013) **1783–1794**
70. Jiao, L. and J.R. Regalbuto, *The synthesis of highly dispersed noble and base metals on silica via strong electrostatic adsorption: I. Amorphous silica*. Journal of Catalysis, 2008. **260**(2): p. 329-341.
71. Mehrabadi, B.A.T., et al., *A Review of Preparation Methods for Supported Metal Catalysts*. 2017. p. 1-35.
72. Tae-Wan Kim, F.K., ‡ Blain Paul, and Ryong Ryoo\*, *MCM-48-like Large Mesoporous Silicas with Tailored Pore Structure: Facile Synthesis Domain in a Ternary Triblock Copolymer-Butanol-Water System*. J. AM. CHEM. SOC., 2005. **127**, **7601-7610**.
73. O'Connell, K. and J.R. Regalbuto, *High Sensitivity Silicon Slit Detectors for 1 nm Powder XRD Size Detection Limit*. Catalysis Letters, 2015. **145**(3): p. 777-783.
74. Riyapan, S., et al., *Preparation of improved Ag–Pd/TiO<sub>2</sub> catalysts using the combined strong electrostatic adsorption and electroless deposition methods for the selective hydrogenation of acetylene*. Catalysis Science & Technology, 2016. **6**(14): p. 5608-5617.
75. Thommes, M., et al., *Physisorption of gases, with special reference to the evaluation of surface area and pore size distribution (IUPAC Technical Report)*. Pure and Applied Chemistry, 2015. **87**(9-10): p. 1051-1069.
76. Mérida-Morales, S., et al., *Influence of morphology of zirconium-doped mesoporous silicas on 5-hydroxymethylfurfural production from mono-, di- and polysaccharides*. Catalysis Today, 2021. **367**: p. 297-309.
77. Liang, J., et al., *Heterogeneous Catalysis in Zeolites, Mesoporous Silica, and Metal-Organic Frameworks*. Adv Mater, 2017. **29**(30).

78. Jongerius, A.L., et al., *Stability of Pt/ $\gamma$ -Al<sub>2</sub>O<sub>3</sub> Catalysts in Lignin and Lignin Model Compound Solutions under Liquid Phase Reforming Reaction Conditions*. ACS Catalysis, 2013. **3**(3): p. 464-473.
79. Ryan M. Ravenelle, F.S.I., ‡ Andrew D'Amico, † Nadiya Danilina, § Jeroen A. van Bokhoven, §, | Johannes A. Lercher, ‡ Christopher W. Jones, † and Carsten Sievers\*, †, *Stability of Zeolites in Hot Liquid Water*. J. Phys. Chem. C, 2010. **114**, **19582–19595**.
80. Bakare, I.A., et al., *Hydrothermal stability of MTT zeolite in hot water: The role of La and Ce*. Microporous and Mesoporous Materials, 2016. **233**: p. 93-101.
81. Kyriakidou, E.A., et al., *Synthesis of Ag nanoparticles on oxide and carbon supports from Ag diammine precursor*. Journal of Catalysis, 2016. **344**: p. 749-756.
82. J. Korah, W.A.S., and J.R. Regalbuto, *Effect of impurities on the pzc of silica or alumina*. Catalysis Letters, 2003. **Vol. 85, Nos. 1–2, January 2003**.
83. Hao, X., et al., *The control of platinum impregnation by PZC alteration of oxides and carbon*. Journal of Molecular Catalysis A: Chemical, 2004. **219**(1): p. 97-107.
84. Banerjee, R., et al., *Detection of Ambient Oxidation of Ultrasmall Supported Platinum Nanoparticles with Benchtop Powder X-Ray Diffraction*. Catalysis Letters, 2017. **147**(7): p. 1754-1764.
85. Banerjee, R. and J.R. Regalbuto, *Rectifying the chemisorption – XRD discrepancy of carbon supported Pd: Residual chloride and/or carbon decoration*. Applied Catalysis A: General, 2020. **595**.
86. Tengco, J.M.M., et al., *Chemisorption–XRD particle size discrepancy of carbon supported palladium: Carbon decoration of Pd?* Catalysis Today, 2015. **246**: p. 9-14.
87. Gavrilov, A.N., et al., *On the influence of the metal loading on the structure of carbon-supported PtRu catalysts and their electrocatalytic activities in CO and methanol electrooxidation*. Phys Chem Chem Phys, 2007. **9**(40): p. 5476-89.
88. Hosseiniamoli, H., et al., *Understanding Structure–Function Relationships in Zeolite-Supported Pd Catalysts for Oxidation of Ventilation Air Methane*. ACS Catalysis, 2018. **8**(7): p. 5852-5863.
89. Deutsch, K.L. and B.H. Shanks, *Hydrodeoxygenation of lignin model compounds over a copper chromite catalyst*. Applied Catalysis A: General, 2012. **447-448**: p. 144-150.
90. Hong, Y.-K., et al., *The catalytic activity of Pd/WO<sub>x</sub>/Al<sub>2</sub>O<sub>3</sub> for hydrodeoxygenation of guaiacol*. Applied Catalysis B: Environmental, 2014. **150-151**: p. 438-445.

91. RajamanickamMaheswari, J.M.M.T., 2 AnandRamanathan,1 JohnRegalbuto\*,2 andBala Subramaniam\*,1, *Effects of Pd Nanoparticle Loading and Support Acidity on Liquid Phase Hydrodeoxygenation of Oxygenated Aromatics*. ACS Symposium Series book: Advanced Heterogeneous Catalysts Volume 1: Applications at the Nano-Scale, 2020. **Chapter 7pp 213-238**.
92. Jin, W., et al., *Noble Metal Supported on Activated Carbon for “Hydrogen Free” HDO Reactions: Exploring Economically Advantageous Routes for Biomass Valorisation*. ChemCatChem, 2019. **11**(17): p. 4434-4441.
93. Silva, N.K.G., et al., *Gas-phase hydrodeoxygenation (HDO) of guaiacol over Pt/Al<sub>2</sub>O<sub>3</sub> catalyst promoted by Nb<sub>2</sub>O<sub>5</sub>*. Fuel, 2021. **287**.
94. Teles, C.A., et al., *Role of the metal-support interface in the hydrodeoxygenation reaction of phenol*. Applied Catalysis B: Environmental, 2020. **277**.
95. de Souza, P.M., et al., *Hydrodeoxygenation of Phenol over Pd Catalysts. Effect of Support on Reaction Mechanism and Catalyst Deactivation*. ACS Catalysis, 2017. **7**(3): p. 2058-2073.
96. Teles, C.A., et al., *Reaction pathways for the HDO of guaiacol over supported Pd catalysts: Effect of support type in the deoxygenation of hydroxyl and methoxy groups*. Molecular Catalysis, 2021.
97. Wang, W., C.-J. Liu, and W. Wu, *Bifunctional catalysts for the hydroisomerization of n-alkanes: the effects of metal–acid balance and textural structure*. Catalysis Science & Technology, 2019. **9**(16): p. 4162-4187.
98. Wu, X., et al., *Effect of acid-metal balance of bifunctional Pt/Beta catalysts on vapor phase hydrodeoxygenation of m-cresol*. Catalysis Today, 2020. **355**: p. 43-50.
99. Hensley, A.J.R., et al., *Catalytic consequences of hydrogen addition events and solvent-adsorbate interactions during guaiacol-H<sub>2</sub> reactions at the H<sub>2</sub>O-Ru(0 0 0 1) interface*. Journal of Catalysis, 2021. **395**: p. 467-482.
100. Scoullou, E.V., et al., *Guaiacol Adsorption and Decomposition on Platinum*. The Journal of Physical Chemistry C, 2018. **122**(51): p. 29180-29189.
101. Wang, A., et al., *Selective Production of  $\gamma$ -Valerolactone and Valeric Acid in One-Pot Bifunctional Metal Catalysts*. ChemistrySelect, 2018. **3**(4): p. 1097-1101.
102. Sharma, A.K., P. Mehara, and P. Das, *Recent Advances in Supported Bimetallic Pd–Au Catalysts: Development and Applications in Organic Synthesis with Focused Catalytic Action Study*. ACS Catalysis, 2022. **12**(11): p. 6672-6701.
103. Sankar, M., et al., *Designing bimetallic catalysts for a green and sustainable future*. Chem Soc Rev, 2012. **41**(24): p. 8099-139.

104. Tao, F.F., *Synthesis, catalysis, surface chemistry and structure of bimetallic nanocatalysts*. Chem Soc Rev, 2012. **41**(24): p. 7977-9.
105. Loza, K., M. Heggen, and M. Epple, *Synthesis, Structure, Properties, and Applications of Bimetallic Nanoparticles of Noble Metals*. Advanced Functional Materials, 2020. **30**(21).
106. Wu, J., et al., *Surface lattice-engineered bimetallic nanoparticles and their catalytic properties*. Chem Soc Rev, 2012. **41**(24): p. 8066-74.
107. Zhang, T., et al., *Single-atom alloy catalysts: structural analysis, electronic properties and catalytic activities*. Chem Soc Rev, 2021. **50**(1): p. 569-588.
108. Villa, A., et al., *New challenges in gold catalysis: bimetallic systems*. Catalysis Science & Technology, 2015. **5**(1): p. 55-68.
109. Zhang, L., Z. Xie, and J. Gong, *Shape-controlled synthesis of Au-Pd bimetallic nanocrystals for catalytic applications*. Chem Soc Rev, 2016. **45**(14): p. 3916-34.
110. Lee, J.-S.M., et al., *Homogenized Bimetallic Catalysts from Metal–Organic Framework Alloys*. Chemistry of Materials, 2019. **31**(11): p. 4205-4212.
111. van der Hoeven, J.E.S., et al., *Unlocking synergy in bimetallic catalysts by core-shell design*. Nat Mater, 2021. **20**(9): p. 1216-1220.
112. Marcinkowski, M.D., et al., *Pt/Cu single-atom alloys as coke-resistant catalysts for efficient C-H activation*. Nat Chem, 2018. **10**(3): p. 325-332.
113. Zhao, X., et al., *Recent Progress in Pd-Based Nanocatalysts for Selective Hydrogenation*. ACS Omega, 2022. **7**(1): p. 17-31.
114. Navlani-García, M., et al., *New Approaches Toward the Hydrogen Production From Formic Acid Dehydrogenation Over Pd-Based Heterogeneous Catalysts*. Frontiers in Materials, 2019. **6**.
115. Nasrollahzadeh, M., et al., *Recent developments in palladium (nano)catalysts supported on polymers for selective and sustainable oxidation processes*. Coordination Chemistry Reviews, 2019. **397**: p. 54-75.
116. Xiao, W., et al., *Optimizing the ORR activity of Pd based nanocatalysts by tuning their strain and particle size*. Journal of Materials Chemistry A, 2017. **5**(20): p. 9867-9872.
117. Ishida, T., et al., *Importance of Size and Contact Structure of Gold Nanoparticles for the Genesis of Unique Catalytic Processes*. Chem Rev, 2020. **120**(2): p. 464-525.

118. Hartadi, Y., D. Widmann, and R.J. Behm, *CO<sub>2</sub> hydrogenation to methanol on supported Au catalysts under moderate reaction conditions: support and particle size effects*. ChemSusChem, 2015. **8**(3): p. 456-65.
119. Sankar, M., et al., *Role of the Support in Gold-Containing Nanoparticles as Heterogeneous Catalysts*. Chem Rev, 2020. **120**(8): p. 3890-3938.
120. Gao, F. and D.W. Goodman, *Pd-Au bimetallic catalysts: understanding alloy effects from planar models and (supported) nanoparticles*. Chem Soc Rev, 2012. **41**(24): p. 8009-20.
121. Miura, H. and T. Shishido, *Concerted Catalysis of Pd and Au on Alloy Nanoparticles for Efficient Heterogeneous Molecular Transformations*. Chemistry Letters, 2021. **50**(2): p. 346-352.
122. Jiang, Z., S. Guo, and T. Fang, *Enhancing the Catalytic Activity and Selectivity of PdAu/SiO<sub>2</sub> Bimetallic Catalysts for Dodecahydro-N-ethylcarbazole Dehydrogenation by Controlling the Particle Size and Dispersion*. ACS Applied Energy Materials, 2019. **2**(10): p. 7233-7243.
123. Han, S. and C.B. Mullins, *Catalytic Reactions on Pd-Au Bimetallic Model Catalysts*. Acc Chem Res, 2021. **54**(2): p. 379-387.
124. Dimitratos, N., et al., *Pd and Pt catalysts modified by alloying with Au in the selective oxidation of alcohols*. Journal of Catalysis, 2006. **244**(1): p. 113-121.
125. Chakarova, K., et al., *Well-Defined Negatively Charged Gold Carbonyls on Au/SiO<sub>2</sub>*. The Journal of Physical Chemistry C, 2011. **115**(43): p. 21273-21282.
126. Rojas, H., et al., *Hydrogenation of  $\alpha,\beta$ -unsaturated carbonyl compounds over Au and Ir supported on SiO<sub>2</sub>*. Journal of Molecular Catalysis A: Chemical, 2012. **363-364**: p. 122-128.
127. Sean R. Noble, S.E.B., Ritubarna Banerjee a, Jeff Miller, John R. Regalbuto *Supported nanoparticle synthesis with Au bis-Ethylenediamine: The mechanism of adsorption onto oxides and carbons*. Journal of Catalysis. **393** (2021) **344–356**.
128. Eskandari, S., et al., *Pushing the limits of electrostatic adsorption: charge enhanced dry impregnation of SBA-15*. Catalysis Today, 2019. **338**: p. 60-71.
129. A. Wong, Q.L., 1 S. Griffin,1 A. Nicholls,2 J. R. Regalbuto1\*, *Synthesis of ultrasmall, homogeneously alloyed, bimetallic nanoparticles on silica supports*. Science, 2017. **358**, **1427–1430** (2017).
130. Shourong Zhu, W.G., Douglas R. Powell, and Judith A. Walmsley, *Synthesis, Structures, and Electrochemistry of Gold(III) Ethylenediamine Complexes and Interactions with Guanosine 5'-Monophosphate*. Inorganic Chemistry. **Vol. 45, No. 6, 2006**.

131. Rakočević, L., et al., *Hydrogen Evolution on Reduced Graphene Oxide-Supported PdAu Nanoparticles*. *Catalysts*, 2021. **11**(4).
132. N. Santhanam, T.A.C., W. Spieker, J.R. Regalbuto, *Nature of metal catalyst precursors adsorbed onto oxide supports*. *Catalysis Today* 21 (1994) 141-156.
133. REGALBUTO, K.B.A.A.J.R., *A Revised Physical Theory for Adsorption of Metal Complexes at Oxide Surfaces*. *JOURNAL OF COLLOID AND INTERFACE SCIENCE* 1997. **185**, 174–189 (1997).
134. Samad, J.E., et al., *The controlled synthesis of metal-acid bifunctional catalysts: Selective Pt deposition and nanoparticle synthesis on amorphous aluminosilicates*. *Journal of Catalysis*, 2016. **342**: p. 213-225.
135. Banerjee, R., et al., *Ambient Oxidation of Ultrasmall Platinum Nanoparticles on Microporous Carbon Catalyst Supports*. *ACS Applied Nano Materials*, 2018. **1**(10): p. 5876-5884.
136. Alcantara Ortigoza, M. and S. Stolbov, *The perturbation energy: A missing key to understand the "nobleness" of bulk gold*. *J Chem Phys*, 2015. **142**(19): p. 194705.
137. Wu, P., et al., *Formation of PdO on Au–Pd bimetallic catalysts and the effect on benzyl alcohol oxidation*. *Journal of Catalysis*, 2019. **375**: p. 32-43.
138. GRAHAM J. HUTCHINGS\*, A.C.J.K., *Strategies for the Synthesis of Supported Gold Palladium Nanoparticles with Controlled Morphology and Composition*. *ACCOUNTS OF CHEMICAL RESEARCH*
139. Suo, Y. and I.M. Hsing, *Synthesis of bimetallic PdAu nanoparticles for formic acid oxidation*. *Electrochimica Acta*, 2011. **56**(5): p. 2174-2183.
140. Pei, G.X., et al., *Promotional effect of Pd single atoms on Au nanoparticles supported on silica for the selective hydrogenation of acetylene in excess ethylene*. *New Journal of Chemistry*, 2014. **38**(5).
141. *A simple accurate determination of oxide PZC and the strong buffering effect of oxide surface at incipient wetness*.
142. Bukhtiyarov, A.V., et al., *In situ formation of the active sites in Pd-Au bimetallic nanocatalysts for CO oxidation: NAP (near ambient pressure) XPS and MS study*. *Faraday Discuss*, 2018. **208**(0): p. 255-268.
143. Verma, P., et al., *Bimetallic PdAu Catalysts within Hierarchically Porous Architectures for Aerobic Oxidation of Benzyl Alcohol*. *Nanomaterials (Basel)*, 2021. **11**(2).



144. Bachiller-Baeza, B., et al., *Pd–Au bimetallic catalysts supported on ZnO for selective 1,3-butadiene hydrogenation*. *Catalysis Science & Technology*, 2020. **10**(8): p. 2503-2512.
145. Giorgi, J.B., *FTIR-Study of CO adsorption on crystalline-silica-supported palladium particles.pdf*. 2002.
146. Gates, B.C., et al., *Atomically dispersed supported metal catalysts: perspectives and suggestions for future research*. *Catalysis Science & Technology*, 2017. **7**(19): p. 4259-4275.
147. Kim, D., et al., *Synergistic geometric and electronic effects for electrochemical reduction of carbon dioxide using gold-copper bimetallic nanoparticles*. *Nat Commun*, 2014. **5**: p. 4948.
148. Kuo, C.-T., et al., *Structure Sensitivity of Acetylene Semi-Hydrogenation on Pt Single Atoms and Subnanometer Clusters*. *ACS Catalysis*, 2019. **9**(12): p. 11030-11041.
149. Liu, J., et al., *Tackling CO Poisoning with Single-Atom Alloy Catalysts*. *J Am Chem Soc*, 2016. **138**(20): p. 6396-9.
150. Simonovis, J.P., et al., *Enhanced Stability of Pt-Cu Single-Atom Alloy Catalysts: In Situ Characterization of the Pt/Cu(111) Surface in an Ambient Pressure of CO*. *The Journal of Physical Chemistry C*, 2018. **122**(8): p. 4488-4495.
151. Zhang, X., et al., *Platinum-copper single atom alloy catalysts with high performance towards glycerol hydrogenolysis*. *Nat Commun*, 2019. **10**(1): p. 5812.
152. Chen, Z. and P. Zhang, *Electronic Structure of Single-Atom Alloys and Its Impact on The Catalytic Activities*. *ACS Omega*, 2022. **7**(2): p. 1585-1594.
153. Pei, G.X., et al., *Ag Alloyed Pd Single-Atom Catalysts for Efficient Selective Hydrogenation of Acetylene to Ethylene in Excess Ethylene*. *ACS Catalysis*, 2015. **5**(6): p. 3717-3725.
154. Mamatkulov, M., et al., *Pd Single-Atom Sites on the Surface of PdAu Nanoparticles: A DFT-Based Topological Search for Suitable Compositions*. *Nanomaterials (Basel)*, 2021. **11**(1).
155. Hannagan, R.T., et al., *Single-Atom Alloy Catalysis*. *Chem Rev*, 2020. **120**(21): p. 12044-12088.
156. Liu, J., et al., *Integrated Catalysis-Surface Science-Theory Approach to Understand Selectivity in the Hydrogenation of 1-Hexyne to 1-Hexene on PdAu Single-Atom Alloy Catalysts*. *ACS Catalysis*, 2019. **9**(9): p. 8757-8765.

157. Reocreux, R., et al., *Efficient and selective carbon-carbon coupling on coke-resistant PdAu single-atom alloys*. Chem Commun (Camb), 2019. **55**(100): p. 15085-15088.
158. Liu, J., et al., *Palladium-gold single atom alloy catalysts for liquid phase selective hydrogenation of 1-hexyne*. Catalysis Science & Technology, 2017. **7**(19): p. 4276-4284.
159. Lee, J.D., et al., *Dilute Alloys Based on Au, Ag, or Cu for Efficient Catalysis: From Synthesis to Active Sites*. Chem Rev, 2022. **122**(9): p. 8758-8808.
160. Wrasman, C.J., et al., *Dilute Pd/Au Alloys Replace Au/TiO<sub>2</sub> Interface for Selective Oxidation Reactions*. ACS Catalysis, 2020. **10**(3): p. 1716-1720.
161. A. Wong, Q.L., 1 S. Griffin, 1 A. Nicholls, 2 J. R. Regalbuto 1\*, *Synthesis of ultrasmall, homogeneously alloyed, bimetallic nanoparticles on silica supports*. Science **358**, **1427–1430** (2017).
162. Regalbuto, J.R., *Catalyst Preparation: Science and Engineering. Chapter 13 Strong Electrostatic Adsorption of Metals onto Catalyst Supports*. CRC Press, 2006.
163. R. P. BLOCK\* AND JOHN C. HAILAR, J., *The Reaction of Gold(III) with Some Bidentate Coordinating Groups*. GoLD(III) WITH SOME BIDENTATE COORDINATING GROUP, 1951.
164. *Preparation, characterization and catalytic activity of gold-based nanoparticles on HY zeolites*. Catalysis Today **72** (2002) **115–121**.
165. Lipp, J.W., *FINE POINTS FOR BROAD BUMPS: THE EXTENSION OF RIETVELD REFINEMENT FOR BENCHTOP POWDER XRD ANALYSIS OF ULTRASMALL SUPPORTED NANOPARTICLES*. Dissertation of University of South Carolina, 2022.
166. Miller, J.T., et al., *The effect of gold particle size on AuAu bond length and reactivity toward oxygen in supported catalysts*. Journal of Catalysis, 2006. **240**(2): p. 222-234.
167. Denton, A.R. and N.W. Ashcroft, *Vegard's law*. Phys Rev A, 1991. **43**(6): p. 3161-3164.
168. Leppert, L., R.Q. Albuquerque, and S. Kümmel, *Gold-platinum alloys and Vegard's law on the nanoscale*. Physical Review B, 2012. **86**(24).
169. Qian, K., et al., *Alloying Au surface with Pd reduces the intrinsic activity in catalyzing CO oxidation*. Catalysis Today, 2017. **280**: p. 253-258.
170. HARTOG, R.V.H.a.F., *THE STATISTICS OF SURFACE qTOMS AND SURFACE SITES ON METAL CRYSTALS*. surface science, 1969. **15**: p. 189-230.

171. C.-W. Yi, K.L., T. Wei, and D. W. Goodman, *The Composition and Structure of Pd-Au Surfaces*. J. Phys. Chem. B 2005. **2005**, **109**, **18535-18540**.
172. Tiruvalam, R.C., et al., *Aberration corrected analytical electron microscopy studies of sol-immobilized Au + Pd, Au{Pd} and Pd{Au} catalysts used for benzyl alcohol oxidation and hydrogen peroxide production*. Faraday Discuss, 2011. **152**: p. 63-86; discussion 99-120.
173. Gallo, I.B.C., E.A. Carbonio, and H.M. Villullas, *What Determines Electrochemical Surface Processes on Carbon-Supported PdAu Nanoparticles?* ACS Catalysis, 2018. **8**(3): p. 1818-1827.
174. Kaden, W.E., *Electronic structure controls reactivity of size-selected Pd clusters adsorbed on TiO<sub>2</sub> surfaces*. 2009.
175. Griselda C. Cabilla, A.a.L.B.a.M.A.B.a., *Characterization by CO/FTIR spectroscopy of Pd/silica catalysts and its correlation with syn-gas conversion*. Catalysis Letters **55 (1998) 147-156**.
176. Tereshchenko, A., et al., *Pd nanoparticle growth monitored by DRIFT spectroscopy of adsorbed CO*. Analyst, 2020. **145**(23): p. 7534-7540.
177. Luneau, M., et al., *Dilute Pd/Au Alloy Nanoparticles Embedded in Colloid-Templated Porous SiO<sub>2</sub>: Stable Au-Based Oxidation Catalysts*. Chemistry of Materials, 2019. **31**(15): p. 5759-5768.
178. Shan, J., et al., *PdCu Single Atom Alloys for the Selective Oxidation of Methanol to Methyl Formate at Low Temperatures*. Topics in Catalysis, 2020. **63**(7-8): p. 618-627.
179. *Infrared determination of the accessible metallic surface of supported palladium containing ceria*. Applied Catalysis A: General. **67 (1991) 325-335**.
180. *ESTIMATION OF THE NUMBER OF CO MOLECULES ADSORBED IN VARIOUS MODES ON DIFFERENT CRYSTAL PLANES OF ALUMINA SUPPORTED POLYCRYSTALLINE PALLADIUM*. Surface Science 1987. **188 (1987) 505-518**.
181. *Molecular Orbital View of Chemisorbed Carbon Monoxide*. The Journal of Physical Chemistry C, 1964.
182. Junling Lu, B.F., 2, *Coking- and Sintering-Resistant Palladium Catalysts Achieved Through Atomic Layer Deposition*. 2012.
183. Ouyang, M., et al., *Directing reaction pathways via in situ control of active site geometries in PdAu single-atom alloy catalysts*. Nat Commun, 2021. **12**(1): p. 1549.

184. *THE CHEMISORPTION OF CARBON MONOXIDE ON PALLADIUM SINGLE CRYSTAL SURFACES: IR SPECTROSCOPIC EVIDENCE FOR LOCALISED SITE ADSORPTION*. Surface Science **72 (1978) 513-535**.
185. Filie, A., et al., *The dynamic behavior of dilute metallic alloy Pd<sub>x</sub>Au<sub>1-x</sub>/SiO<sub>2</sub> raspberry colloid templated catalysts under CO oxidation*. Catalysis Science & Technology, 2021. **11(12)**: p. 4072-4082.
186. Ricciardulli, T., et al., *Effect of Pd Coordination and Isolation on the Catalytic Reduction of O<sub>2</sub> to H<sub>2</sub>O<sub>2</sub> over PdAu Bimetallic Nanoparticles*. J Am Chem Soc, 2021. **143(14)**: p. 5445-5464.
187. Davis, S.E., M.S. Ide, and R.J. Davis, *Selective oxidation of alcohols and aldehydes over supported metal nanoparticles*. Green Chem., 2013. **15(1)**: p. 17-45.
188. Giannakakis, G., et al., *NiAu Single Atom Alloys for the Non-oxidative Dehydrogenation of Ethanol to Acetaldehyde and Hydrogen*. Topics in Catalysis, 2018. **61(5-6)**: p. 475-486.
189. Li, H., W. Chai, and G. Henkelman, *Selectivity for ethanol partial oxidation: the unique chemistry of single-atom alloy catalysts on Au, Ag, and Cu(111)*. Journal of Materials Chemistry A, 2019. **7(41)**: p. 23868-23877.
190. Mitsutaka Okumura, Y.K., Masatake Haruta, Kizashi Yamaguchi, *DFT studies of interaction between O<sub>2</sub> and Au clusters. The role of anionic surface Au atoms on Au clusters for catalyzed oxygenation*. Chemical Physics Letters 2001. **346 (2001) 163±168**.

## APPENDIX A

### SUPPLEMENTARY MATERIALS TO CHAPTER 2

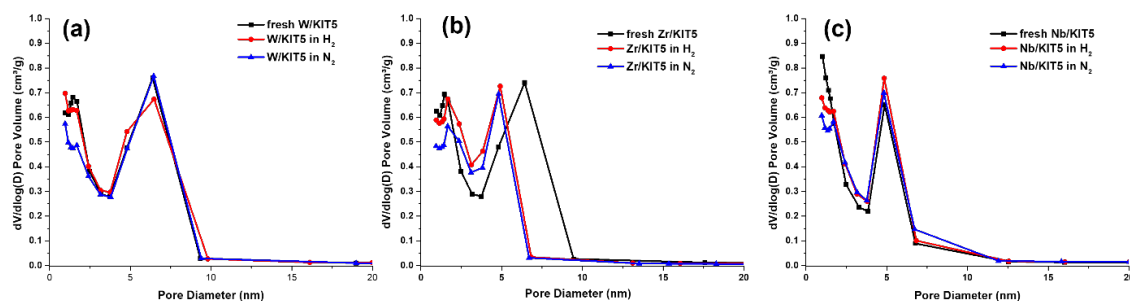


Figure A.1 Pore size distribution of metal doped KIT5 silicas before and after hydrothermal stability tests.

Table A.1 Acidity of bifunctional catalysts and supports quantified by NH<sub>3</sub>-TPD.

sample	Peak I		Peak II		Peak III		Total acidity mmol NH <sub>3</sub> /g <sub>cat.</sub>
	T (°C)	mmol NH <sub>3</sub> /g <sub>cat.</sub> (percentage %)	T (°C)	mmol NH <sub>3</sub> /g <sub>cat.</sub> (percentage %)	T (°C)	mmol NH <sub>3</sub> /g <sub>cat.</sub> (percentage %)	
Zr-KIT5	218	0.04 (6.8)	307	0.43 (67.1)	427	0.16 (26.1)	0.63
Pd/Zr-KIT5-SEA	200	0.09 (12.5)	251, 305	0.58 (76.1)	413	0.09 (4.4)	0.76
Pd/Zr-KIT5-DI	216	0.08 (12.0)	252, 312	0.60 (85.8)	412	0.03 (2.2)	0.70
Nb-KIT5	214	0.02 (9.4)	309	0.15 (61.2)	487	0.07 (29.4)	0.25
Pd/Nb-KIT5-SEA	207	0.05 (14.7)	304	0.24 (72.2)	514	0.04 (13.1)	0.33
Pd/Nb-KIT5-DI	205	0.04 (15.4)	284	0.15 (63.5)	511	0.05 (21.1)	0.24
Zr-KIT6	212	0.03 (4.6)	300	0.45 (68.2)	419	0.18 (27.2)	0.64
Pd/Zr-KIT6-SEA	209	0.08 (8.3)	257, 334	0.49 (72.5)	424	0.13 (10.0)	0.71
Pd/Zr-KIT6-DI	203	0.03 (4.6)	255,321	0.60 (84.7)	424	0.08 (10.7)	0.73
Nb-6	207	0.02 (11.0)	291	0.12 (64.5)	471	0.045 (24.5)	0.18
Pd/Nb-KIT6-SEA	218	0.04 (10.3)	314	0.23 (62.3)	495	0.10 (27.4)	0.37
Pd/Nb-KIT6-DI	205	0.02 (10.4)	289	0.13 (74.1)	485	0.03 (15.4)	0.18

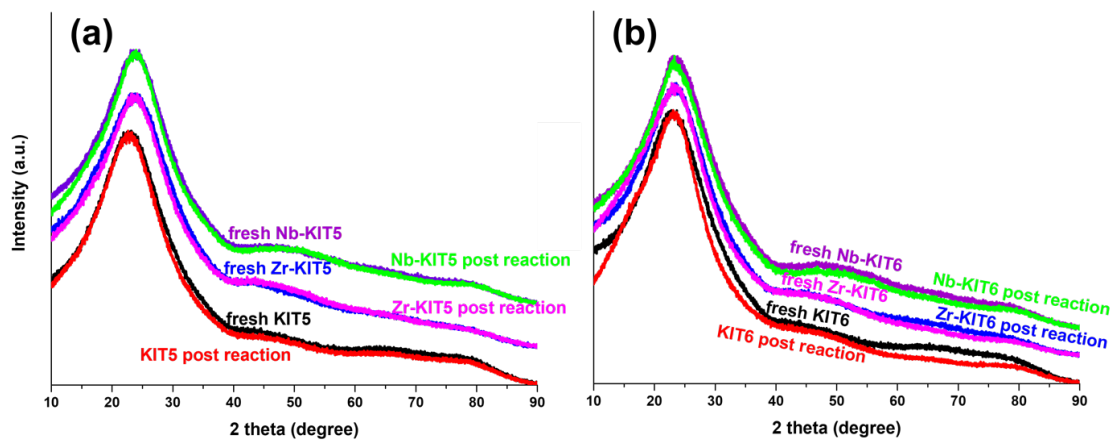


Figure A.2 XRD patterns of silica supports before and post HDO reaction for 1 hr: (a) KIT5 series silicas; (b) KIT6 series silicas.

APPENDIX B

SUPPLEMENTARY MATERIALS TO CHAPTER 3

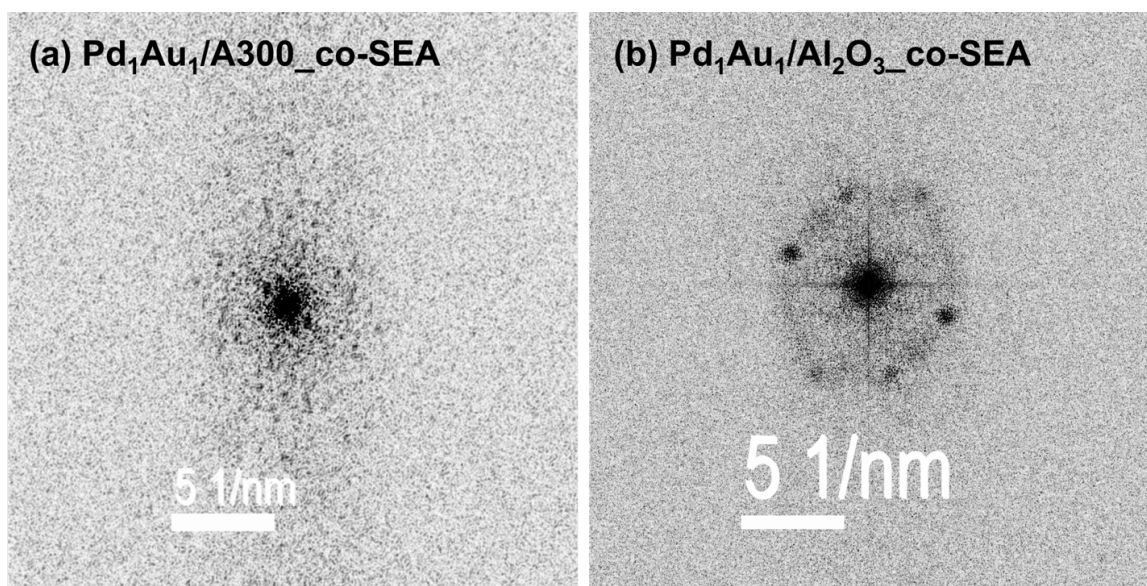


Figure B.1 FFT images for  $\text{Pd}_1\text{Au}_1/\text{A300\_co-SEA}$  (a) and  $\text{Pd}_1\text{Au}_1/\text{Al}_2\text{O}_3\_co\text{-SEA}$  (b).

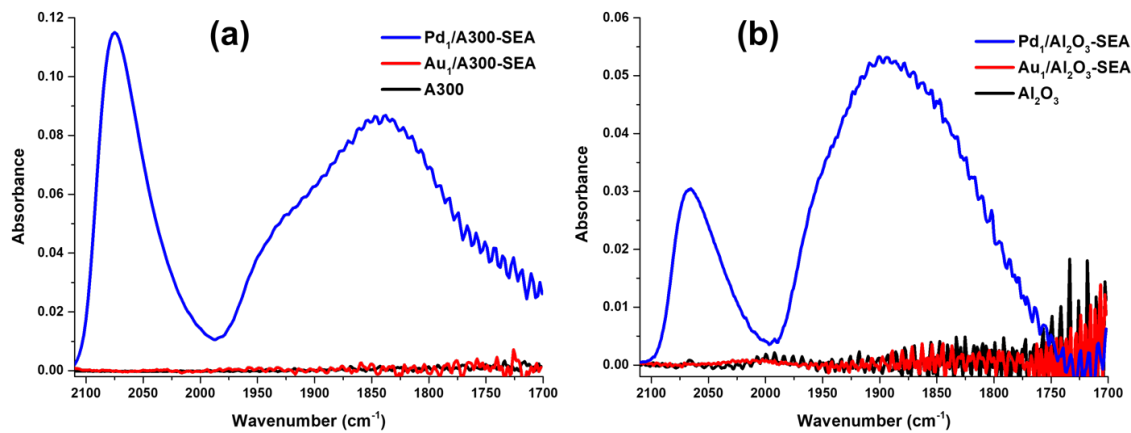


Figure B.2 FTIR spectra over pure support and single Pd, Au materials: (a) on 300; (b)  $\gamma$ -Al<sub>2</sub>O<sub>3</sub>.